Nanoengineering Heterogeneous Catalysts for the Selective Hydrogenation of Key Agrochemical and Industrial Derivatives

Scott Board

Master of Philosophy

Aston University
European Bioenergy Research Institute

June 2016

Aston University

Nanoengineering Heterogeneous Catalysts for the Selective Hydrogenation of Key Agrochemical and Industrial Derivatives

Scott Board

Master of Philosophy

2016

Selective hydrogenation through tailored catalysts for both agrochemical and commercial chemical precursors opens the potential for low energy and low waste production within both industries. For the purposes of this work, catalyst series with varying loadings of palladium nanoparticles were prepared upon both amorphous silica, and the structured mesoporous SBA-15. Full and extensive characterisations of both series were performed, and comparisons between the two made.

For work focusing on agrochemical derivatives, research was done using the simplified reference chemical crotononitrile. A wide range of systematic screenings were performed to identify the effect of a variety of variables upon the activity and selectivity of the reaction These included the effect of metal loading, catalyst mass, temperature, hydrogen pressure, and perturbation. Results indicated a poor selectivity towards nitrile hydrogenation within mild conditions, with more notable results within higher pressures.

Key findings within the crotononitrile work highlighted a retardation effect within higher pressures. Extensive work including beam-time at the Diamond Light Source synchrotron allowed for the successful identification of palladium-hydride in-situ. As a result, a positive correlation was formed between hydride formation and the retardation of the nitrile selectivity due to its effect upon the active sites of the catalyst.

For the work looking at the commercial aspect of selective hydrogenation, the conversion of cinnamaldehyde to cinnamyl alcohol was reviewed. Utilising the same catalyst series identified in previous research, a similar screening of reaction conditions and their effects upon the activity and selectivity were performed. With key comparisons to previous work within the group utilising platinum-based catalysts, it was concluded that palladium exhibited a much higher activity but at the cost of lowered selectivity towards aldehyde hydrogenation. Additionally, with previous work espousing the effect of alignment within cinnamaldehyde hydrogenation, it was noted that palladium was much less beholden to the effects of support polarity due to silanol species. Parallel work on sterically inhibiting moieties within benzaldehyde test reagents also highlighted a strong effect on catalytic activity due to poor metal-reagent surface alignment.

Key Words: Selective hydrogenation, catalysis, crotononitrile, cinnamaldehyde, XAS

Acknowledgements

To begin I wish to give my thanks to my supervisors, Professor Karen Wilson, and Professor Adam F. Lee. Thank you both for the opportunity to do this research, and also for your advice and motivation through everything. I will always value the chances you afforded me. I also give thanks to my industrial supervisors Dr Colin Brennan and Dr Martin Bowden at Syngenta, for helping fund this work and for providing critical and cheerfully encouraging feedback at many points throughout my studies.

I am very grateful to all the members of the Surface, Materials, and Catalysis Group, and to those within the European Bioenergy Research Institute. Your expertise, assistance, and most importantly friendship, are what kept me going through these past years. Thank you both to Dr Christopher M.A. Parlett and Dr Mark Isaacs for their constant help and comradery during my time within the group. I also give special thanks to my friend and colleague Mr James Hunns, who helped keep me sane despite the numerous bumps in the road.

Finally, I wish to say a profound thank you to all the friends and family who have helped me and supported me every step of the way. To my mother Sonia and my father Ian, thank you for helping me become the man I am today, and for your unwavering belief in me even when I did not share the sentiment. To Ben Brain, for being the best friend anyone could ask for and forever being there for me. To my sisters Zöe and Lauren, for making me smile and always showing you cared. Lastly, to my baby brothers James and Ben, to whom I dedicate this work, in the hopes that they will achieve great things and find happiness in their lives.

"If I have seen further it is by standing on the shoulders of Giants" – Isaac Newton

Declaration

I declare that the research conducted and described in this MPhil thesis was carried out between October 2012 and June 2016 and is the sole work of the author. This work has not previously been submitted in whole or part for a degree at any other time or at any other academic institution. I hereby give my consent as author for my thesis, if accepted, to be made available for photocopying and for inter-library loan, and for the title and summary to be made readily available to outside institutions.

Table of Contents

Chapter 1 – Introduction

Chapter 2 – Experimental

Chapter 4 – Selective hydrogenation of allylic aldehydes using tuneable palladium-based catalysts

Chapter 5 – Conclusions and future work

List of Figures, Tables & Equations

Chapter 1 – Introduction

Chapter 2 – Experimental

Chapter 3 – Selective hydrogenation of allylic nitriles using tuneable palladium-based catalysts

Chapter 4 – Selective hydrogenation of allylic aldehydes using tuneable palladium-based catalysts

Chapter 5 – Conclusions

Chapter 1

Introduction

1.2 Introduction

1.2.1 Green Chemistry and Heterogeneous Catalysis

With an ever-increasing awareness for the impacts we make upon the earth from industrial processes, it has become more and more important to discover greener processes for the synthesis of industrial-scale fine chemicals. The first comprehensive set of guidelines for effective economically and environmentally friendly chemical processes was originally proposed by Dr Paul Anastas, and have become known as the '12 Principles of Green Chemistry'.[1] These principles, which are outlined within **Figure 1.1** and detailed in **Table 1.1**, lay a framework for modern chemists and detail the conditions a reaction should fulfil in order to be designated as environmentally friendly or, colloquially, 'green'. In an effort to achieve the goal of environmentally benign and economically fortuitous processes, the use of heterogeneous catalysis has been incorporated to fulfil many of these principles.

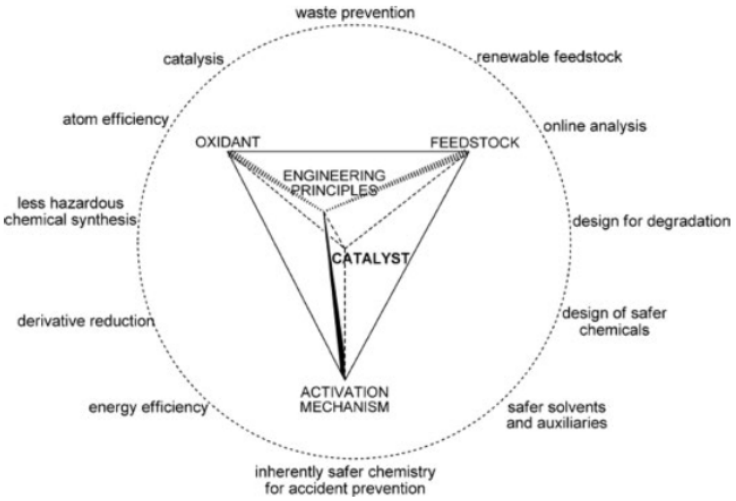

Figure 1.1 – Visualisation of the 12 principles of green chemistry and how they apply to modern catalyst synthesis (Modified source material).[2]

The word 'Catalysis', derived from the Greek for "dissolution" or "breaking down", was first utilised by the Swedish chemist Jöns Jacob Berzelius in a report written in 1835.[3] Within, he describes substances which increase the rate of a reaction whilst remaining unaltered by the process. The official definition of a catalyst, as noted by the Oxford English Dictionary is as follows. "A substance which when present in small amounts increases the rate of a chemical reaction or process but which is chemically unchanged by the reaction; a catalytic agent.".[4]

1	**Prevention** – It is better to prevent waste than to treat or clean it up upon creation.
2	**Atom Economy** – Methods should be designed to maximise the incorporation of all materials used in the process into the final product
3	**Less Hazardous** – Where practical, design methods to use and generate substances with little or no toxicity to human health and the environment
4	**Safer Chemicals** – Chemical products should be designed to affect their desired function whilst minimising their toxicity
5	**Safer Solvents/Auxiliaries** – Auxiliary substances should be made unnecessary wherever possible and innocuous when used
6	**Energy Efficiency** – Energy requirements of processes should be minimised, and if possible methods should be conducted at ambient temperature & pressure
7	**Renewable Feedstock** – A raw material should be renewable wherever technically and economically practical
8	**Derivatives** – Protective steps (protecting/blocking groups, *etc.*) should be minimised or avoided if possible as such steps require additional reagents
9	**Catalysis** – Catalytic reagents are superior to stoichiometric reagents
10	**Degradation** – Chemical products should be designed to break down into innocuous products at the end of their function
11	**Real-time Analysis** – Reactions should be engineered to allow for real-time monitoring and control prior to the formation of hazardous substances
12	**Accident Prevention** – Substances used should be chosen to minimise the potential for chemical accidents such as releases, explosions and fires

Table 1.1 – A modified outline of the '12 principles' of green chemistry.[1]

To elucidate, at the core of any reaction its rate is determined by the activation energy (the energy required for the reaction to occur) of the slowest stage, the 'rate determining step'. A catalyst is a material which, upon addition into a reaction, provides an 'alternate pathway' for the reaction, in which the overall activation energy is lower and thus more energetically favourable. As such, an increased number of molecules can achieve the required energy level, which will subsequently increase the reaction rate of the process in question. Importantly, the substance used to achieve this must end the reaction in the same state as it began to be considered a catalyst.

Catalysts can also help increase the selectivity of a reaction, by providing the energetic equivalent of a path of least resistance towards a specific product. This concept is illustrated in **Figure 1.2**.[5]

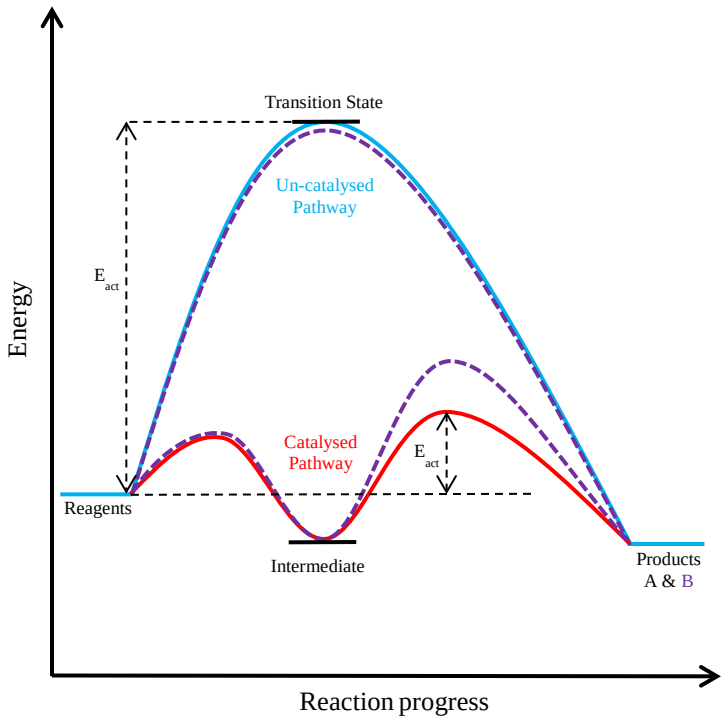

Figure 1.2 – Illustration of the effect a catalyst has upon both reaction rate and selectivity. (Bold lines for product A, dotted for B). The lowered activation energy of 'A' in the catalysed pathway compared to that of 'B' increases the products selectivity.[5]

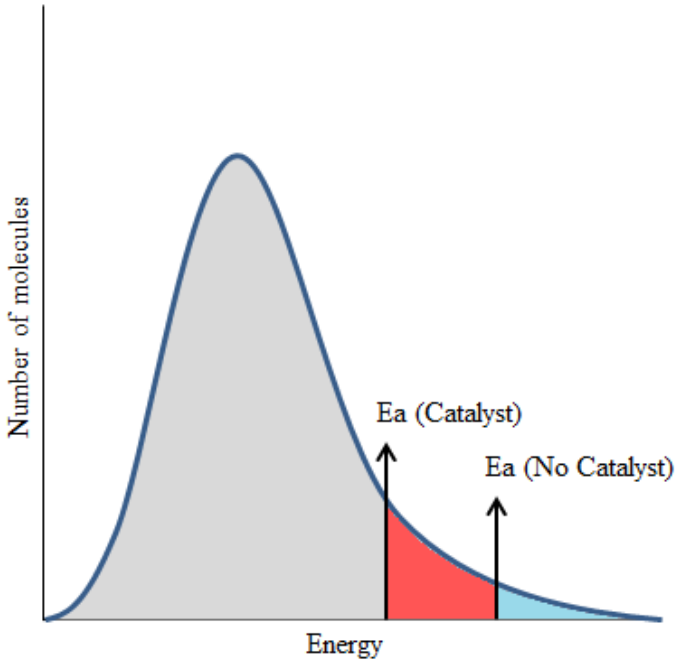

Figure 1.3 –Maxwell- Boltzmann Distribution, indicating the effect of a catalyst

The diagram shown above (**Figure 1.3**) is known as a Maxwell-Boltzmann Distribution, and is used in this instance to describe the interaction of a catalyst within a reaction.[6,7] The figure displays the 'area' of particles with the sufficient activation energy. By adding a catalyst and reducing this value, more molecules achieve or exceed this value and thus the reaction rate increases.

1.1.2 Catalyst design and supports

The field of catalysis can be categorised into two fields, homogeneous and heterogeneous catalysis. Homogenous catalysts reside in the same phase as the mixture it is reacting with, predominantly the liquid phase. Enzymes, or biocatalysts, fall into this group but are sometimes considered a separate class. The advantages and disadvantages of heterogeneous or homogeneous catalysts has been a source of debate for as long as the techniques have been available. The key factor in most cases is that whilst homogeneous catalysts display far greater activity and tunability for certain reactions, their very nature causes catalyst recovery to become incredibly difficult. This, in turn, means that in many cases fresh catalysts must be produced for each reaction batch, significantly hindering commercial viability as well as causing environmental concerns.[8]

Heterogeneous catalysts react with mixtures in another phase to their own. Because of this, there is ease in separation from the reaction mixture *via* various forms of filtering. Their main drawback, however, is that their active sites are less well understood, with a large number of variable factors which can easily alter the efficiency of the catalyst if allowed to change. Heterogeneous catalysts also suffer from the effects of poisoning or inhibiting substances (irreversible and reversible, respectively). Catalyst poisoning can be a major issue for industrial scale processes, and is one of the issues that will be addressed later in this work

For heterogeneous catalysts the ability to support the catalytic active sites, in this case metal nanoparticles, provides a distinct advantage over its homogeneous counterparts, as the support can be filtered and removed from each experiment or batch, allowing for a much more economically and ecologically viable option. In addition, the use of heterogeneous catalysts means that specific active sites such as metal oxides can be generated within the reaction (*in-situ*) allowing for much greater control.

Typically, the more common catalytic supports are based either on their inert nature, or in their ability to supplement or assist the actions of the catalytic sites.[9] Carbonaceous materials, such as pure activated carbon or the more advanced forms of carbon nanotubes and carbon fibre are commonly utilised in modern catalysts.[10] This is often due to their high porosity and surface area, and the ease at which the surface properties can be altered by processes such as doping.[11]

The most commonly utilised supports for heterogeneous catalysts are those that fall under the category of metal oxides. With high chemical and thermal stability, coupled with significantly high surface areas, these are ideal for a wide variety of different catalysts and processes. Many of them can be further modified or functionalised to provide more attractive surfaces for metal nanoparticles, to assist in the chemical process, or even function as catalysts themselves. The most common metal oxides employed as supports are titania, ceria, alumina and most relevant for this thesis, silica.[12,13] For the efforts of this project, silica was chosen as a basic support for the catalysts due to its ability to be easily manipulated and impregnated with metal nanoparticles along with its inert nature, and also for its abundance and low cost.

In addition, polymers and biopolymers have been cited as having significant advantages for supporting metal nanoparticles due to their stable nature and ready availability. These include more recent advancements for polymers such as polyorganophosphazenes (POP) and fibres.[14] With a strong push towards even more 'green' processes, the use of biopolymers has recently become a topic of interest, with some work on creating mesoporous starch polymer already underway.[15]

In an effort to further increase the capabilities of catalytic supports, effort has been taken to investigate the effects of material manipulation and the modification of surface area and porosity for the purposes of increased metal dispersion and thus activity.[16,17,18,19] Within the realm of porosity there are three major categories, divided in respect to the size of the generated pores diameter. The largest is macroporosity (> 50 nm) followed by mesoporosity (2-50 nm) and finally microporosity (< 2 nm). Microporosity poses an issue as although it increases surface area the pores are typically too small for any substrate diffusion. Conversely, macropores sheer size will reduce overall surface area.[20]

In essence, we are left with mesoporosity as the ideal, with pore diameters in a range that allows for the vast majority of substrates to diffuse through without hindrance, whilst also significantly increasing the surface area of the support. It is noted however that

very recent work on the combination of both mesoporosity and macroporosity, in what is being referred to as hierarchical pore network, can yield extremely interesting results.[21 22]

Initial work on structured porous silica was performed and patented as far back as 1964 by Degussa.[23] However, it would be several more decades before interest in this process was taken, and acknowledged as a potentially ground-breaking process.[24] With the principles laid out in this work, in 1998 Zhao et al., produced a material which is now referred to as Santa Barbara Type 15 (SBA-15). SBA-15 is a highly structured mesoporous silica designed to maximise silica surface area with well-ordered and highly structured '2D' mesopores channels of a range of 4-30 nm.[25] As shown in **Figure 1.4**, Pluronic P-123 is a triblock polymer with two hydrophilic 'heads' on either end of a hydrophobic body. Based upon more recent work within this field using x-ray scattering, we know that upon addition to water in large quantities they will form self-assembled micelle 'coins' due to its thermodynamic stability.[26] These micelles coins will then align together into flexible rods to increase their stability, which are coated and subsequently strengthened by the addition of silica from the TEOS onto their surface. These straightened rods inevitably crash out of solution, and as they settle will orient themselves into hexagonal configurations. Upon extraction, the solid is calcined, thereby burning out the micelle template within each hexagonally aligned tube, resulting in a well-defined porous structure (More detail in **Chapter 2**). This process is now widely used and modified.[26,27,28]

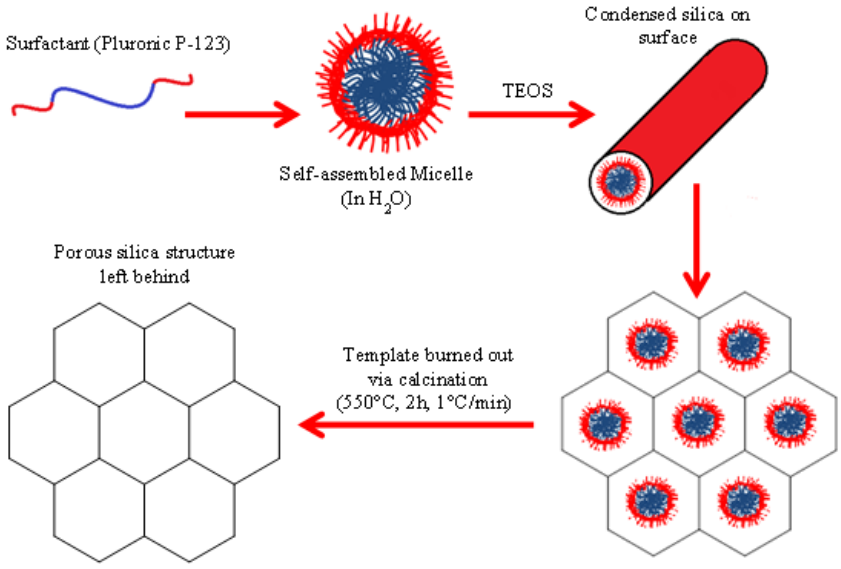

Figure 1.4 – Illustration highlighting process of formation for SBA-15 mesoporous silica

One of the most attractive properties of mesoporous silica, and SBA-15 in particular, is the ability to tailor the synthesis process in such a way as to modify the porosity characteristics of the resultant product.[29,30] Specifically, by altering the

temperature at varying stages of the synthesis, you can easily affect the morphology. For instance, as you move from 35-100 °C you see an increase in pore diameter and a decrease in wall thickness.[31]

The main drawback of SBA-15 is that, compared to generic amorphous silica, the formation of the support is time consuming with multiple steps. Namely, the aging of the support takes over 24 hours, and calcination to remove the micelle from the new structure must be done slowly so as to avoid localised overheating, causing damage to the structure.[32] Other processes such as solvent or supercritical fluid extraction have been looked into, but often encounter issues with full removal.[33,34] The length of this process can be detrimental on an industrial scale, but may prove to be a negligible issue when compared to the increased yield generated from using such a tailored support.

In regards to the differences between standard amorphous silica and mesoporous SBA-15, a potentially key difference can be found. In regards to the surface of these supports, we must consider the presence of silanol groups. These are a moiety designated as Si-O-H, and are present in varying amounts upon silica surfaces. The key factor is that these groups, present as isolated, geminal, and vicinal, are quite polar, and thus induce hydrophilicity upon the catalyst. It is known that SBA-15 contains far greater amounts of these silanol groups, and it has been reported that the repulsive nature of these can have a profound effect upon the alignment of reagents upon the metallic active site.[35,36 ,37] As a result, this factor must be something that is investigated, specifically in the case of aldehyde hydrogenations.

1.1.3 Selective Hydrogenations

In reference to the 12 principles as highlighted earlier, modern industrial processes are attempting to move away from traditional means of hydrogenation. Namely, these involve the use of strong reducing agents such as formic acid (HCOOH),[38] hydrazine (H_2NNH_2),[39] lithium aluminium hydride ($LiAlH_4$),[40] and sodium borohydride ($NaBH_4$).[41] Whilst these agents are excellent donators of hydrogen, there are several key drawbacks. Firstly, these compounds must be used in often stoichiometric amounts in order to effectively hydrogenate the target reagent, which is in itself a costly issue. To compound this, the agents used are typically highly toxic and therefore pose a great risk to the user and the environment, with issues arising for disposal. Finally, these compounds are often enantioselective for these processes, and therefore selective tuning of a reaction can prove difficult or outright impossible whilst using reducing agents.

In order to mitigate or outright eliminate these issues, the use of gaseous hydrogen (H_2) has been proposed as an effective source of hydrogen atoms for these reactions. When utilising catalysts, specific metallic nanoparticles can be used to dissociate hydrogen across the surface to react with the chosen compounds. Hydrogen gas is typically produced through the process of steam reforming, by which steam (water vapour) and methane react to form carbon monoxide and hydrogen gas.[42] Typically this process is performed using natural gas.[43] A more renewable source of hydrogen can come from production using biomass.[44,45] Finally, other more environmentally friendly sources of hydrogen, such as water-splitting through solar energy, are currently being investigated for optimisation.[46]

1.1.3.1 Nitrile hydrogenations

With an exponentially rising population, with a net gain of roughly 600 million people between 2003 and 2011, there is a growing concern for the production of food to cope with the increasing demand. It has been suggested by The World Bank that by 2030, the worldwide production of cereal will have to increase by approximately 50 % to meet the growing demand.[47] Primary amines (compounds containing an NH_2 moiety) are notably used as intermediates for the synthesis of a wide variety of fine chemicals used in the agrochemical industry.[48] Therefore, a way of producing these cheaply, cleanly, and from renewable resources, could help with the production and protection of crops to meet the increasing demand.

Traditionally, the synthesis of primary amines involved the use of stoichiometric, toxic chemicals, through a multitude of steps and intermediates.[49,50] This is a highly unfavourable process, resulting in a large amount of by-products. E-factor is the amount of waste formed per kg of product, and is often used to give a broad overlook of the selectivity of a process, and to denote how ‘green’ it is. Typical bulk chemical processes have an E-factor in the region of 1-5, with some (like the petrochemical industry) having processes in the region of 0.1. Typical pharmaceutical/fine reactions such as the synthesis of primary amines can have an E-factor anywhere from 5-100, due to increased complexity (**Table 1.2***).*[51] Therefore, it is clear from both a green and economic standpoint that better processes for the synthesis of amines must be found.

Industry Sector	Product Tonnage	E-factor (kg waste/kg product)
Bulk Chemicals	10^4-10^6	<1-5
Fine Chemicals	10^2-10^4	5-50
Pharmaceuticals	10-10^3	25-100

Table 1.2 – Comparison of the E-factor from various industries.[51]

Modern processes utilise catalysts in varying ways in an attempt to make the process cleaner and more efficient. However, a large number of currently employed catalytic processes require unfavourable reaction conditions, coupled with a low level of selectivity for the desired product. Promising steps have been made in attempts to create a single step "one-pot" reaction for industrial application, including work by Yinyan Huang and colleagues.[52] By using a heterogeneous catalyst and the process of hydrogenation, they were able to demonstrate a much more simplistic reaction. With a temperature of 110 °C, and a pressure of 24 bars, it is a significant advancement on historically stoichiometric conditions, and highlights that the process can be made much more efficient.

Hydrogenation, a reaction first made commercially viable by Paul Sabatier, is a process by which molecular hydrogen chemically reacts with another chemical. Typically, and for the purposes of this study, this involves the use of a catalyst, with the alternative requiring a highly pressurised and/or heated system. Hydrogenation is predominantly used in the reduction/saturation of double and triple bonds in organic chemicals.

In the modern industrial age, the process of hydrogenation is widely used in the fine chemicals industry, as well as in pharmaceuticals for a number of processes.[53,54,55,56,57] For the purposes of this work, particular interest has been paid towards what is known as 'Selective hydrogenation'.[58] As the name suggests, it is a process by which only specific unsaturated bonds are hydrogenated in a reaction, whilst leaving others free of alteration.

This is important in industry as it allows for the formation of much more complex molecules without the need for strenuous reaction conditions or wasteful protective groups. There are a number of reported methods for isolating specific bonds in a compound for hydrogenation, including various steric and electronic effects. Catalysts can achieve this in a number of ways. By 'forcing' molecules into specific configurations due to the nature of their active sites, you can essentially keep particular bonds out of reach of the active site.

Similarly, certain elements will have a higher propensity towards adsorbing or bonding depending on their electronic configurations.

In the work to follow in subsequent chapters, insight into the selective hydrogenation of nitrile-species has been conducted. Specifically, research has been carried out on the hydrogenation of benzyl cyanide into 2-phenylethylamine (PEA) with the use of supported palladium catalysts. The aim of this research is to garner a better understanding of the active site and reaction conditions, to facilitate the design of a more efficient and green catalyst for the process of amine formation. To begin, a simpler nitrile-species known as crotononitrile was studied, in the hopes of discovering the conditions required to yield the most industrially desirable and ecologically friendly results. The proposed mechanism for this is shown in **Figure 1.5**. [59 60 61 62] The following work outlines the literature behind the process of nitrile hydrogenation, and the findings of research into this field.

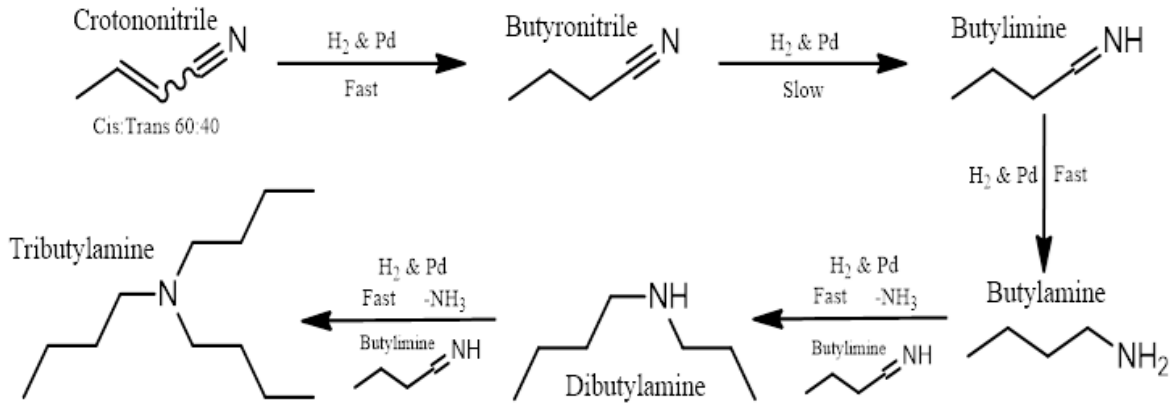

Figure 1.5 – Proposed mechanism for the conversion of crotononitrile into butylamine, and the potential formation of by-products (secondary/tertiary amine formation, butane & ammonia) [Modified from literature].[62]

One of the drawbacks of nitrile hydrogenation is the propensity towards catalytic deactivation by the formation of unwanted by-products with a high affinity towards the active surface of the catalyst.[63] Furthermore, it is difficult to direct the reaction in such a way as to selectively produce the primary amine alone, instead producing large amounts of the secondary or tertiary forms. One recent study at Zhejiang University indicated full conversion, and selectivity in the range of 99 %. However, this was for the tertiary-amine rather than primary.[64] The propensity towards the formation of the 'trimer' rather than the

monomer presents a challenging issue that must to be addressed. In another study, from which *Scheme 1* was based, it is stated that the secondary and tertiary amines are formed from subsequent reaction of the primary amine with the imine intermediate. They note that adding acid into the reaction results in the formation of a salt with the primary amine. This prevents any further conversion, increasing the selectivity significantly.[62]

The proposed reaction mechanism for the production of the secondary and tertiary amines is shown in **Figure 1.6**. Work done in this field has suggested that the addition of large amounts of amine may inhibit the formation of the 'higher amines' due to Le Chatelier's principle.[65] [59] This principle denotes the effect of condition changes upon a chemical equilibrium. In this case the increased volume of amine, a product of this reaction, would cause the equilibrium to shift to the 'left' towards the substrate. In this manner we could arguably slow the formation of secondary/tertiary amines from the primary. However this is clearly a less than optimal solution, resulting in large amounts of waste which would not be applicable for a green industrial reaction. Ammonia addition, unless countered by altering other parameters, will also reduce the overall rate of reaction due to catalytic poisoning, as is mentioned in later segments of this work.[66]

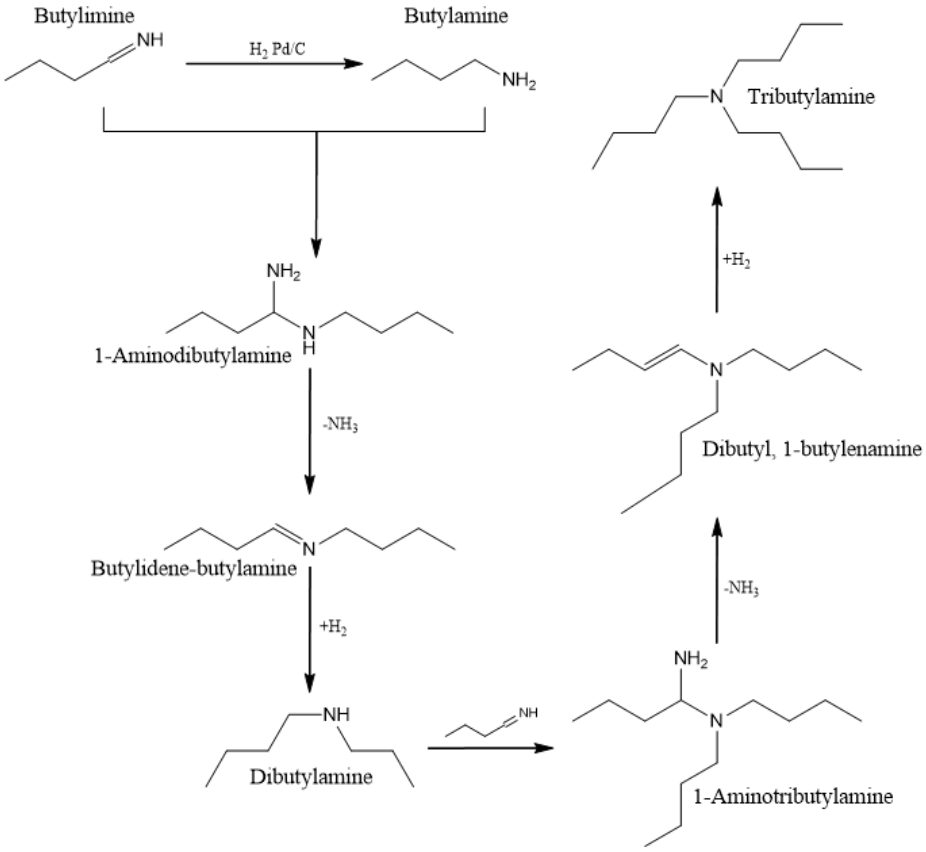

Figure 1.6 – Proposed mechanism detailing the formation of the unwanted secondary and tertiary amines and the intermediates involved in crotononitrile hydrogenation.[59]

In regards to product selectivity, interactions with unsaturated nitriles have been pursued in some papers. It was noted that in reactions containing unsaturated nitriles, the further an alkene bond was situated from the nitrile in the tested substrates, the higher the selectivity towards the unsaturated amine.[67]

As a result of this prior research, there are clear areas of research that require attention to produce the best possible catalyst for this reaction. One such step is determining the exact cause of the catalytic deactivation, and how to prevent or reverse it. Secondly, the interaction of the substrate with the catalyst in relation to selectivity of the primary amine must be reviewed, to reduce the production of the unwanted secondary and tertiary amines in a way which does not require undesirable reagents.

Following along from the research done by my predecessor, the following chapters look into the performance of a commercial palladium-carbon (Pd/C) catalyst with the reaction in question, and the work done towards finding the most suitable catalyst for the job. Particular attention was paid towards the deactivation of this, and other catalysts. As my predecessor discovered, the primary deactivation of the Pd/C catalyst is cyanide upon the surface, and so it was important to discover the mechanism of this process, and potential ways to prevent it from occurring.

Many studies focus on the hydrogenation of butyronitrile, the saturated equivalent of crotononitrile, as removal of the C=C bond prevents the hydrogen present being used up in the hydrogenation of the double bond. This allows for a better understanding of the processes at hand for the nitrile hydrogenation.

Studies performed by various research groups have yielded valuable data concerning the hydrogenation of nitriles. In line with the work for this report, Harold Greenfield shows that the use of a Pd/C catalyst yields the formation of tertiary amine.[68] This, in combination with previous findings supports the suggestion of primary amine formation, but still points to the issue of subsequent reactions to the higher amines. His findings also suggest that catalyst poisoning can be prevented if the reaction is performed in an aqueous medium, rather than an organic solvent. Further work into catalyst poisoning and prevention is covered in the ‘catalytic poisoning’ section.

When considering the hydrogenation of reagents upon a palladium catalyst, it is also important to consider what is taking place upon the active site itself, and with the metallic nanoparticles. Though there is very little literature on the subject, there is the potential for palladium, in an atmosphere of hydrogen, to form a rarely documented structure known as palladium hydride (PdH). This form is proposed to be constructed as a result of prolonged exposure to adsorbed hydrogen atoms, which subsequently insert themselves into the octahedral sites of the palladium FCC structure.[69] This has the potential to severely affect the catalyst active site, as it will invariable alter both the physical and electronic structure of the palladium.

It is reported that this action upon the palladium causes the atoms to be forced apart by a fractionally small degree. Specifically, it will cause a stretching of the inter-atomic distance by 0.1 Å, shifting it from 2.72 to 2.82 angstroms.[70] In addition, this forcible shifting of the atoms will cause a slight decrease in the excitation energy of their electrons. Specifically, it has been quoted in literature that this shift should be in the range of 6.7 eV.[71] In theory, although these changes are incredibly small, they could be detected through the use of X-ray Absorption Spectroscopy (XAS), observing the formation of this hydride phase at the atomic level.[72,73,74,75]

In comparison to work performed within the liquid phase, research has also been done into gas phase hydrogenation, yielding important and intriguing data concerning the exact processes of product formation and catalytic poisoning. Yinyan Huang and colleagues have published extensively into the field of gas-phase hydrogenation and its comparisons to liquid phase.[76] Strikingly, they suggest that the hydrogenation of the nitrile species is not due to adsorbed hydrogen gas on the catalyst, but rather from the methyl group of another nitrile compound.[77] Their work also corroborates with others that nitrogen-bonded chemicals are the intermediates in the formation of all the amine forms.

Further work into the field by the research group further suggests the process of intermolecular hydrogen transfer, by use of deuterated species. Furthermore they establish that hydrogen transfer is more readily processed by acetonitrile when combined with butyronitrile. They propose this is due to “resonance stabilization” in compounds of this kind, resulting in relatively easy C-H fission in the methyl group. Furthermore they state that this sort of process is efficient in breaking the bond between the nitrogen and the catalytic surface. However, in doing so creates a precursor to the secondary amine rather

than the primary which for the purposes of this work is not ideal.[76] The result of this work is a proposed surface mechanism for the formation of subsequent chemical species due to intermolecular hydrogen transfer as shown in ***Figure 1.7***.[61, 76]

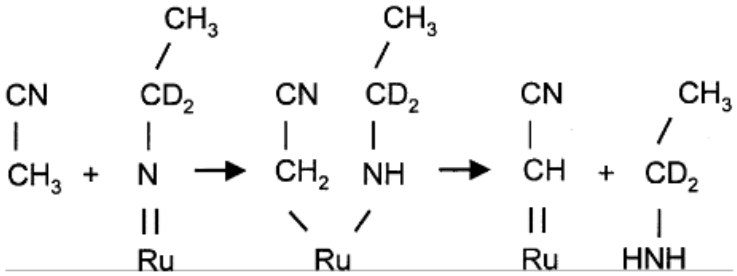

Figure 1.7 – Proposed Intermolecular Hydrogen Transfer for the formation of Amines. Use of deuterated acetonitrile allows for effective tracking of specific hydrogen transfer[76]

As previously mentioned, the production of the amine is thought to occur through the production of an imine intermediate. Due to the highly reactive nature of this compound, researchers have struggled to identify the species in the reaction. In light of this, work has been done in proposing possible alternative intermediates in the reaction. One such paper suggests that there are three possible intermediates when the starting material (in this case acetonitrile) is reacted with two hydrogen atoms; a side-long adsorption for the standard imine, *via* the carbon for a carbine, or through the nitrogen for a nitrene. Examples of these are shown in **Figure 1.8**.[78]

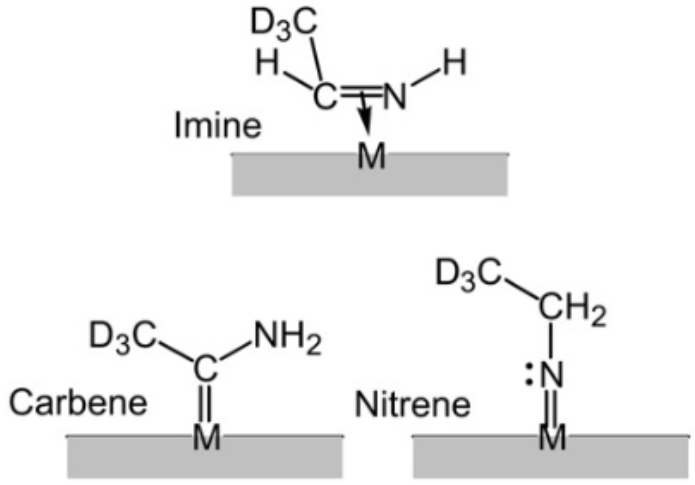

Figure 1.8 – The three potential intermediates formed following the reaction of two hydrogen atoms and the example molecule acetonitrile.[78]

In an effort to increase the conversion of nitrile species into their constituent amines, much of the work in this field is performed under increased pressure. This is done with the aim of increasing hydrogen adsorption into the liquid phase resulting in a concentration and thus higher rate of reaction. Studies observing the effect of increasing reaction pressure suggest that there is a first order relation between pressure increase and reaction rate.

Work in this field also supports the idea of a Langmuir-Hinshelwood type reaction, whereby both molecules involved in the process adsorb onto the surface and react there.[59, 79] This is opposed to the second form of surface reactions, the 'Eley-Rideal' mechanism, whereby only one molecule adsorbs, whilst the other remains in the reaction medium.

The primary aim of the work in this report is to detail the conditions and processes needed for efficient and selective hydrogenation of nitrile compounds. To begin with, the simple nitrile crotononitrile was observed, due to its relatively innocuous nature compared to other nitriles. As mentioned before, this project is partially funded by the company Syngenta. It is hoped that once crotononitrile has been deemed to be sufficiently reviewed, the chemical benzyl cyanide can then be tested under similar conditions.

The choice of chemical was due to benzyl cyanides mimicry of the relevant site that Syngenta requires to be selectively hydrogenated. In this way we can simulate the reactive site without needing to use the actual chemical precursor which will have many NDAs and IPs associated with it.

1.1.3.2 Aldehyde hydrogenations

Within the realms of hydrogenation, another key process is the selective hydrogenation of cinnamaldehyde due to its primarily abundant use in both the food and fragrance industries as an artificial additive to generate the aroma or flavour of cinnamon.[80,81,82] In addition, cinnamaldehyde and its derivatives have been investigated for their applications as antifungal agents,[83] preventing microbial spoilage,[84] and as potential repellent for insects such as mosquitoes.[85]

Previous work within literature,[86,87] and within this research group,[37,88] has focused upon the production of aldehydes such as cinnamaldehyde and its constituents *via* their respective alcohol forms through the use of selective oxidation.[89] In the reverse,

cinnamaldehyde and others can be converted to cinnamyl alcohol or their respective alcohol through the use of selective hydrogenation.

Work with platinum has shown great promise, but due to a combination of high production cost for platinum catalysts and the promisingly high activity of palladium-based catalysts, work has turned more towards this precious metal.[90] However, although palladium has a record for being a highly effective catalytic metal, it shows very little activity when exposed to α,β-unsaturated aldehydes such as cinnamaldehyde. Rather than pushing towards the C=O hydrogenation, it rather focuses on the C=C hydrogenation process and yields small to negligible amounts of cinnamyl alcohol.[91, 92] Even with homogeneous catalysts, well known for their significantly increased activity at the cost of recovery, we see very low selectivity towards this desired product, instead seeing large quantities of the other products such as phenyl propan-1-ol and phenyl propionaldehyde.[93]

In addition, computational models of an α,β-unsaturated ethylenic aldehyde upon palladium have been performed.[94] In this extensive study, it has been determined that selectivity towards the aldehyde bond is severely inhibited, with much more activity towards the standard C=C bond. It concludes that this is due to two key reasons. The first is the method of adsorption upon the surface, with chemisorption upon the di-σ_{CC} coordination, with eventual interaction of the oxygen lone pair upon the surface. For this they suggest decreasing the binding strength of the reagent via larger substituents or by using metals with larger d orbitals such as osmium or iridium. Additional suggestions included the use of lewis acid promoters to activate the carbonyl, and enriching the surface with electrons by use of titanium dioxide or graphite, to favour C=O coordination. It suggests this is predominantly an issue with platinum systems. Secondly, it advises that if the C=C bond is not solely coordinated, then both coordinate simultaneously within a quasi-planar situation. In this case C=C hydrogenation is simply preferred through kinetics alone. It suggests this is more typical for palladium systems, and is quoted as proclaiming this a difficult situation to improve and that palladium is intrinsically poor for selective hydrogenation of C=O.[94]

1.1.4 Catalyst Poisoning

When considering the ability for a catalyst to perform optimally and without any form of inhibition, there are several factors which may contribute. These factors are often

divided into several different categories.[95] Of these, there are a few key processes relevant to this work.

'Fouling' is a process of mechanical deposition upon the surface and pores, and is often contributed to carbonaceous species and referred to as coking. In this, the catalysts activity is diminished by reagent being physically unable to reach the active sites. For porous catalysts this is usually due to pore blockage. 'Thermal degradation' is the process by which the pore structure may collapse from over-heating, or the metal nanoparticles sinter. The collapsing of pore structure is an obvious aspect, cutting off access to active sites and decreasing surface area. Sintering is the process by which smaller particles of metal will shift across the surface and merge into larger clusters. When this happens, the total number of active sites decrease, as much of the metal becomes trapped within the bulk of the particles. Examples of this, performed by Gareth Parkinson et al. within Nature Materials show precisely how vulnerable catalysts are to this process, through the use of Scanning Tunnelling Microscopy (STM) (**Figure 1.9**).[96]

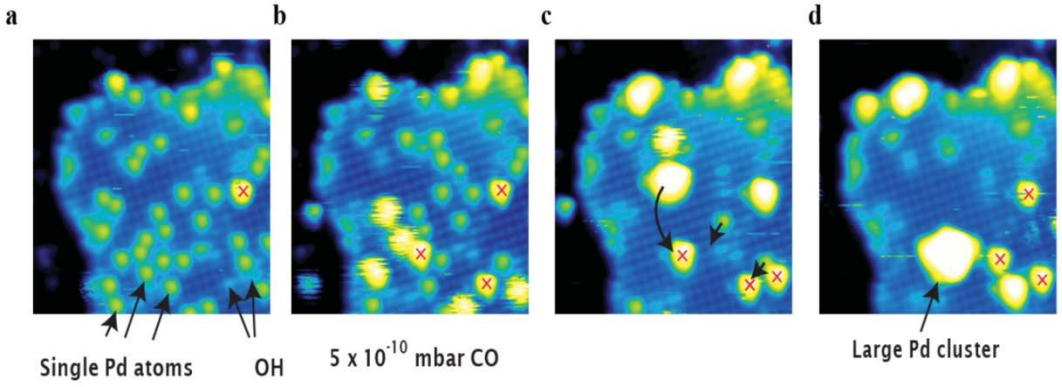

Figure 1.9 – STM images taken from a 36 frame 'movie' over the course of two hours. Frames indicate significant palladium adatom sintering over this time frame.[96]

Finally, 'Poisoning' is similar to fouling, but occurs through chemisorption upon the catalyst. By chemically binding to the active site, a poisoning agent will prevent any other interactions with the site, nullifying the catalysts capabilities (**Figure 1.10**).[97]

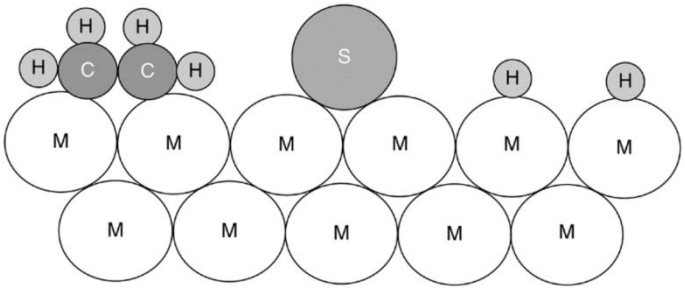

Figure 1.10 – Example of catalytic poisoning (In this case, *via* sulphur on the metal)[97]

There are two categories of chemical ‘poisoning’ which affects the effectiveness of a catalyst, known as inhibitors and poisons. In general terms, a poison is a substance which detrimentally affects the ability of a catalyst to perform, usually by blocking the active sites. Inhibitors are components which can be removed from the catalyst with varying ease and are referred to as temporary, whilst poisons are permanent and cannot be purged.

For work in the field of nitrile hydrogenation, my predecessor Dr Christine Gaskell proposed that potential poisoning of the catalyst is caused by the formation of cyanide ($^{+}C{\equiv}N$) ions in the reaction, due to over hydrogenation and cleavage of the C-C bond. These bind strongly to the surface of the catalyst and result in a high level of poisoning. However, further literature work into potential poisoning has presented an additional potential source. Nitrogen itself can be a potent catalytic poisoner, specifically for the platinum group metals (PGM). Ammonia, especially, has been found to be a catalytic poison, with the ionic form (NH_4) being shielded and therefore non-toxic, but the standard form (NH_3) being toxic to catalysts. The prerequisite for most poisons seems to be the presence of a free pair of valence electrons to form a strong “poison-to-catalyst bond”.[98]

Studies have shown that ammonia is about 40% as toxic to hydrogenating catalysts as a cyanide ion. Although lower, this may still pose a significant issue towards catalytic activity, especially in a system where, as previously stated, a significant amount of ammonia can be produced in the formation of higher amines. This poses a problem as ammonia is also suggested as a way of reducing the formation of higher amines by shifting the reaction equilibrium, and thus increasing selectivity towards the primary amine. Addition of ammonia has previously been proved to do this, but also shown to lower the rate by poisoning.[66]

In the same vein, this applies to the amines products themselves, strongly adsorbing to the surface and acting as a poison, as suggested by Dr Christine Gaskell in her work and by other researchers.[68] The work of Dr Harold Greenfield and his team indicates that if the reaction is performed in an aqueous medium, rather than using the typical organic solvent such as methanol, the catalytic poisoning is significantly reduced. His presumption is that this is caused by the formation of the non-toxic ionic ammonium, rather than remaining in its ‘toxic’ form.[68]

As mentioned earlier, work by Yinyan Huang and colleagues have looked extensively into gas-phase hydrogenation and the processes of product formation and catalytic poisoning. Their findings show that the stability of the catalyst is affected by the medium in which it is performed, in a similar fashion to the work by Greenfield. They indicate that gas-phase hydrogenation highlights a faster rate of deactivation than the same reaction in the liquid phase, suggesting that a liquid phase is needed for the desorption a strongly adsorbing molecule.[99] This expands upon Dr Greenfield's work on the nature of the liquid phase being important to mitigate this.

In regards to the hydrogenation of aldehydes, there is the potential for coking to occur, with some carbonaceous species blocking the porous structure of the catalyst. Although there are some reports on the formation of CO and carbonaceous species upon platinum catalysts when performing aldehyde hydrogenation, it is unlikely for poisoning to occur due to the sheer abundance of hydrogen within these reactions, a point which is also made in the literature.[100] Sintering, however, is a consistent issue for catalysts for a variety of supports and metal nanoparticles, as was indicated by Parkinson et al.[96] As such, this may pose a potential issue for both nitrile and aldehyde hydrogenation.

1.2 Thesis Aims

The aims of this scientific investigation are as follows:

- To garner a better understanding of the mechanistic actions that govern the rates and selectivity of nitrile hydrogenation reactions upon palladium nanoparticle catalysts, and the roles that reaction variables such as catalytic support, temperature, and pressure, have upon this process.
- To develop a better understanding of the processes by which aldehyde hydrogenation may take place, in much the same way as with the previous aim. Specifically, there will be direct comparison to prior work performed within the group utilising platinum catalysts.

1.3 References

1. P. Anastas, J. W., Green Chemistry: Theory and Practice. *Oxford University Press* **1998**, 30.
2. Mizuno, N., *Modern Heterogeneous Oxidation Catalysis*. Wiley: 2009.
3. Berzelius, J. J. *Årsberättelse om framstegen i fysik och kemi (Annual report on progress in physics and chemistry)*; Royal Swedish Academy of Sciences: Stockholm, 1835; p 245.
4. Dictionary, O. E., *"catalyst, n."*. Oxford University Press.
5. P. Atkins, H. d. P., *Elements of Physical Chemistry*. Oxford University Press: Oxford, 2005.
6. Maxwell, J. C., Illustrations of the dynamical theory of gases. Part I. On the motions and collisions of perfectly elastic spheres. *Philosophical Magazine* **1860,** *19*, 19-32.
7. Maxwell, J. C., Illustrations of the dynamical theory of gases. Part II. On the process of diffusion of two or more kinds of moving particles among one another. *Philosophical Magazine* **1860,** (20), 21-37.
8. D. J. Cole-Hamilton, R. P. T., *Catalyst Separation, Recovery and Recycling*. Springer: 2006; Vol. 30.
9. White, R. J.; Luque, R.; Budarin, V. L.; Clark, J. H.; Macquarrie, D. J., Supported metal nanoparticles on porous materials. Methods and applications. *Chemical Society Reviews* **2009,** *38* (2), 481-494.
10. Serp, P.; Corrias, M.; Kalck, P., Carbon nanotubes and nanofibers in catalysis. *Applied Catalysis A: General* **2003,** *253* (2), 337-358.
11. Tasis, D.; Tagmatarchis, N.; Bianco, A.; Prato, M., Chemistry of Carbon Nanotubes. *Chemical Reviews* **2006,** *106* (3), 1105-1136.
12. Glaspell, G.; Hassan, H. M. A.; Elzatahry, A.; Abdalsayed, V.; El-Shall, M. S., Nanocatalysis on Supported Oxides for CO Oxidation. *Topics in Catalysis* **2008,** *47* (1), 22-31.
13. Sandoval, A.; Gómez-Cortés, A.; Zanella, R.; Díaz, G.; Saniger, J. M., Gold nanoparticles: Support effects for the WGS reaction. *Journal of Molecular Catalysis A: Chemical* **2007,** *278* (1–2), 200-208.
14. Astruc, D.; Lu, F.; Aranzaes, J. R., Nanoparticles as Recyclable Catalysts: The Frontier between Homogeneous and Heterogeneous Catalysis. *Angewandte Chemie International Edition* **2005,** *44* (48), 7852-7872.
15. Budarin, V. L.; Clark, J. H.; Luque, R.; Macquarrie, D. J.; White, R. J., Palladium nanoparticles on polysaccharide-derived mesoporous materials and their catalytic performance in C-C coupling reactions. *Green Chemistry* **2008,** *10* (4), 382-387.
16. Ciesla, U.; Schüth, F., Ordered mesoporous materials. *Microporous and Mesoporous Materials* **1999,** *27* (2–3), 131-149.
17. Grün, M.; Unger, K. K.; Matsumoto, A.; Tsutsumi, K., Novel pathways for the preparation of mesoporous MCM-41 materials: control of porosity and morphology. *Microporous and Mesoporous Materials* **1999,** *27* (2–3), 207-216.
18. Davis, M. E., Ordered porous materials for emerging applications. *Nature* **2002,** *417* (6891), 813-821.
19. Van Der Voort, P.; Vercaemst, C.; Schaubroeck, D.; Verpoort, F., Ordered mesoporous materials at the beginning of the third millennium: new strategies to create hybrid and non-siliceous variants. *Physical Chemistry Chemical Physics* **2008,** *10* (3), 347-360.
20. Price, P. M.; Clark, J. H.; Macquarrie, D. J., Modified silicas for clean technology. *Journal of the Chemical Society, Dalton Transactions* **2000,** (2), 101-110.
21. Parlett, C. M. A.; Wilson, K.; Lee, A. F., Hierarchical porous materials: catalytic applications. *Chemical Society Reviews* **2013,** *42* (9), 3876-3893.
22. Parlett, C. M. A.; Isaacs, M. A.; Beaumont, S. K.; Bingham, L. M.; Hondow, N. S.; Wilson, K.; Lee, A. F., Spatially orthogonal chemical functionalization of a hierarchical pore network for catalytic cascade reactions. *Nat Mater* **2016,** *15* (2), 178-182.
23. Biegler, H. 1964.

24. Ruren Xu, W. P., Jihong Yu, Qisheng Huo, Jiesheng Chen, *Chemisty of Zeolites and Related Porous Materials: Synthesis and Structure*. Wiley: 2007.
25. Zhao, D.; Huo, Q.; Feng, J.; Chmelka, B. F.; Stucky, G. D., Nonionic Triblock and Star Diblock Copolymer and Oligomeric Surfactant Syntheses of Highly Ordered, Hydrothermally Stable, Mesoporous Silica Structures. *Journal of the American Chemical Society* **1998,** *120* (24), 6024-6036.
26. Khodakov, A. Y.; Zholobenko, V. L.; Impéror-Clerc, M.; Durand, D., Characterization of the Initial Stages of SBA-15 Synthesis by in Situ Time-Resolved Small-Angle X-ray Scattering. *The Journal of Physical Chemistry B* **2005,** *109* (48), 22780-22790.
27. Kónya, Z.; Puntes, V. F.; Kiricsi, I.; Zhu, J.; Alivisatos, A. P.; Somorjai, G. A., Nanocrystal Templating of Silica Mesopores with Tunable Pore Sizes. *Nano Letters* **2002,** *2* (8), 907-910.
28. Wan, Y.; Zhao, On the Controllable Soft-Templating Approach to Mesoporous Silicates. *Chemical Reviews* **2007,** *107* (7), 2821-2860.
29. Fulvio, P. F.; Pikus, S.; Jaroniec, M., Tailoring properties of SBA-15 materials by controlling conditions of hydrothermal synthesis. *Journal of Materials Chemistry* **2005,** *15* (47), 5049-5053.
30. Gerardin, C.; Reboul, J.; Bonne, M.; Lebeau, B., Ecodesign of ordered mesoporous silica materials. *Chemical Society Reviews* **2013,** *42* (9), 4217-4255.
31. Zhao, D.; Sun, J.; Li, Q.; Stucky, G. D., Morphological Control of Highly Ordered Mesoporous Silica SBA-15. *Chemistry of Materials* **2000,** *12* (2), 275-279.
32. Beck, J. S.; Vartuli, J. C.; Roth, W. J.; Leonowicz, M. E.; Kresge, C. T.; Schmitt, K. D.; Chu, C. T. W.; Olson, D. H.; Sheppard, E. W.; McCullen, S. B.; Higgins, J. B.; Schlenker, J. L., A new family of mesoporous molecular sieves prepared with liquid crystal templates. *Journal of the American Chemical Society* **1992,** *114* (27), 10834-10843.
33. Margolese, D.; Melero, J. A.; Christiansen, S. C.; Chmelka, B. F.; Stucky, G. D., Direct Syntheses of Ordered SBA-15 Mesoporous Silica Containing Sulfonic Acid Groups. *Chemistry of Materials* **2000,** *12* (8), 2448-2459.
34. van Grieken, R.; Calleja, G.; Stucky, G. D.; Melero, J. A.; García, R. A.; Iglesias, J., Supercritical Fluid Extraction of a Nonionic Surfactant Template from SBA-15 Materials and Consequences on the Porous Structure. *Langmuir* **2003,** *19* (9), 3966-3973.
35. Isaienko, O.; Borguet, E., Hydrophobicity of Hydroxylated Amorphous Fused Silica Surfaces. *Langmuir* **2013,** *29* (25), 7885-7895.
36. Christy, A. A., New insights into the surface functionalities and adsorption evolution of water molecules on silica gel surface: A study by second derivative near infrared spectroscopy. *Vibrational Spectroscopy* **2010,** *54* (1), 42-49.
37. Durndell, L. J.; Parlett, C. M. A.; Hondow, N. S.; Isaacs, M. A.; Wilson, K.; Lee, A. F., Selectivity control in Pt-catalyzed cinnamaldehyde hydrogenation. *Scientific Reports* **2015,** *5*, 9425.
38. Garron, A.; Epron, F., Use of formic acid as reducing agent for application in catalytic reduction of nitrate in water. *Water Res.* **2005,** *39* (13), 3073-3081.
39. Djokic, S. S., Electroless deposition of cobalt using hydrazine as a reducing agent. *J. Electrochem. Soc.* **1997,** *144* (7), 2358-2363.
40. Rittmeyer, P., LITHIUM ALUMINUM-HYDRIDE - A VERSATILE REDUCING AGENT IN ORGANIC-SYNTHESIS. *Chim. Oggi-Chem. Today* **1995,** *13* (10), 51-55.
41. Buchner, W.; Niederprum, H., SODIUM-BOROHYDRIDE AND AMINE-BORANES, COMMERCIALLY IMPORTANT REDUCING AGENTS. *Pure Appl. Chem.* **1977,** *49* (6), 733-743.
42. Ogden, J. M., PROSPECTS FOR BUILDING A HYDROGEN ENERGY INFRASTRUCTURE. *Annual Review of Energy and the Environment* **1999,** *24* (1), 227-279.
43. Oxtoby, D. W., *Principles of Modern Chemistry* 5th Edition ed.; Thomson Brooks/Cole: 2002.
44. Kapdan, I. K.; Kargi, F., Bio-hydrogen production from waste materials. *Enzyme and Microbial Technology* **2006,** *38* (5), 569-582.
45. Turner, J. A., Sustainable Hydrogen Production. *Science* **2004,** *305* (5686), 972-974.
46. Perret, R. Development of Solar-Powered Thermochemical Production of Hydrogen from Water. https://www.hydrogen.energy.gov/pdfs/progress07/ii_f_1_perret.pdf.

47. *World Development Report: Agriculture for Development*; The World Bank: 2008.
48. G. Lysenko, V. S., Willy H. Verheye, *Interactions: Food, Agriculture and Environment*. 2010; Vol. 2.
49. Haddenham, D.; Pasumansky, L.; DeSoto, J.; Eagon, S.; Singaram, B., Reductions of Aliphatic and Aromatic Nitriles to Primary Amines with Diisopropylaminoborane. *The Journal of Organic Chemistry* **2009,** *74* (5), 1964-1970.
50. Caddick, S.; Judd, D. B.; Lewis, A. K. d. K.; Reich, M. T.; Williams, M. R. V., A generic approach for the catalytic reduction of nitriles. *Tetrahedron* **2003,** *59* (29), 5417-5423.
51. Sheldon, R. A., Selective catalytic synthesis of fine chemicals: opportunities and trends. *Journal of Molecular Catalysis A: Chemical* **1996,** *107* (1–3), 75-83.
52. Huang, Y.; Sachtler, W. M. H., On the mechanism of catalytic hydrogenation of nitriles to amines over supported metal catalysts. *Applied Catalysis A: General* **1999,** *182* (2), 365-378.
53. Besson, M.; Blanc, B.; Champelet, M.; Gallezot, P.; Nasar, K.; Pinel, C., Diastereoselective hydrogenation of substituted aromatics on supported metal catalysts. *Journal of Catalysis* **1997,** *170* (2), 254-264.
54. Blaser, H.-U.; Jalett, H.-P.; Spindler, F., Enantioselective hydrogenation of α-ketoesters: comparison of homogeneous and heterogeneous catalysts. *Journal of Molecular Catalysis A: Chemical* **1996,** *107* (1–3), 85-94.
55. Gallezot, P.; Richard, D., Selective Hydrogenation of α,β-Unsaturated Aldehydes. *Catalysis Reviews* **1998,** *40* (1-2), 81-126.
56. Landau, R. N.; Singh, U.; Gortsema, F.; Sun, Y. K.; Gomolka, S. C.; Lam, T.; Futran, M.; Blackmond, D. G., A Reaction Calorimetric Investigation of the Hydrogenation of a Substituted Pyrazine. *Journal of Catalysis* **1995,** *157* (1), 201-208.
57. M. Ash, I. A., *Specialty Chemicals Handbook*. Synapse Information Resources: New York, 1997; Vol. 1.
58. Wang, Y.; Yao, J.; Li, H. R.; Su, D. S.; Antonietti, M., Highly Selective Hydrogenation of Phenol and Derivatives over a Pd@Carbon Nitride Catalyst in Aqueous Media. *Journal of the American Chemical Society* **2011,** *133* (8), 2362-2365.
59. Segobia, D. J.; Trasarti, A. F.; Apesteguía, C. R., Hydrogenation of nitriles to primary amines on metal-supported catalysts: Highly selective conversion of butyronitrile to n-butylamine. *Applied Catalysis A: General* **2012,** *445–446* (0), 69-75.
60. Witte, P. T., A new supported rhodium catalyst for selective hydrogenation of nitriles to primary amines. *Collection of Czechoslovak Chemical Communications* **2007,** *72* (4), 468-474.
61. Ortiz-Hernandez, I.; Williams, C. T., In Situ Studies of Butyronitrile Adsorption and Hydrogenation on Pt/Al2O3 Using Attenuated Total Reflection Infrared Spectroscopy. *Langmuir* **2007,** *23* (6), 3172-3178.
62. Hegedűs, L.; Máthé, T.; Kárpáti, T., Selective heterogeneous catalytic hydrogenation of nitriles to primary amines in liquid phase: Part II: Hydrogenation of benzyl cyanide over palladium. *Applied Catalysis A: General* **2008,** *349* (1–2), 40-45.
63. Duch, M. W.; Allgeier, A. M., Deactivation of nitrile hydrogenation catalysts: New mechanistic insight from a nylon recycle process. *Applied Catalysis A: General* **2007,** *318* (0), 190-198.
64. Li, Y.; Gong, Y.; Xu, X.; Zhang, P.; Li, H.; Wang, Y., A practical and benign synthesis of amines through Pd@mpg-C3N4 catalyzed reduction of nitriles. *Catalysis Communications* **2012,** *28* (0), 9-12.
65. Kukula, P.; Studer, M.; Blaser, H.-U., Chemoselective Hydrogenation of α,β-Unsaturated Nitriles. *Advanced Synthesis & Catalysis* **2004,** *346* (12), 1487-1493.
66. Huang, Y.; Sachtler, W. M. H., Catalytic Hydrogenation of Nitriles over Supported Mono- and Bimetallic Catalysts. *Journal of Catalysis* **1999,** *188* (1), 215-225.
67. Kukula, P.; Koprivova, K., Structure-selectivity relationship in the chemoselective hydrogenation of unsaturated nitriles. *Journal of Catalysis* **2005,** *234* (1), 161-171.
68. Greenfield, H., Catalytic Hydrogenation of Butyronitrile. *I&EC Product Research and Development* **1967,** *6* (2), 142-144.

69. Storms, E. A student's guide to cold fusion, Chapter 5, II.2. http://www.lenr-canr.org/StudentsGuide.htm.
70. Bauer, M.; Schoch, R.; Shao, L.; Zhang, B.; Knop-Gericke, A.; Willinger, M.; Schlögl, R.; Teschner, D., Structure–Activity Studies on Highly Active Palladium Hydrogenation Catalysts by X-ray Absorption Spectroscopy. *The Journal of Physical Chemistry C* **2012,** *116* (42), 22375-22385.
71. Kawasaki, A.; Itoh, S.; Shima, K.; Yamazaki, T., Deformation of palladium plates by a small external stress during hydrogen absorption and desorption. *Materials Science and Engineering: A* **2012,** *551*, 231-235.
72. Jalilehvand, F. X-ray Absorption Spectroscopy (XAS). http://www.chem.ucalgary.ca/research/groups/faridehj/xas.pdf.
73. de Groot, F., High-Resolution X-ray Emission and X-ray Absorption Spectroscopy. *Chemical Reviews* **2001,** *101* (6), 1779-1808.
74. Lee, A. F.; Prabhakaran, V.; Wilson, K., Surface X-ray studies of catalytic clean technologies. *Chemical Communications* **2010,** *46* (22), 3827-3842.
75. Ramaker, D. E.; Koningsberger, D. C., The atomic AXAFS and [capital Delta][small mu] XANES techniques as applied to heterogeneous catalysis and electrocatalysis. *Physical Chemistry Chemical Physics* **2010,** *12* (21), 5514-5534.
76. Huang, Y.; Sachtler, W. M. H., Intermolecular Hydrogen Transfer in Nitrile Hydrogenation over Transition Metal Catalysts. *Journal of Catalysis* **2000,** *190* (1), 69-74.
77. Huang, Y.-Y.; Sachtler, W. M. H., Catalytic hydrogenation of nitriles to prim., sec. and tert. amines over supported mono- and bimetallic catalysts. In *Studies in Surface Science and Catalysis*, Avelino Corma, F. V. M. S. M.; José Luis, G. F., Eds. Elsevier: 2000; Vol. Volume 130, pp 527-532.
78. Schärringer, P.; Müller, T. E.; Jentys, A.; Lercher, J. A., Identification of reaction intermediates during hydrogenation of CD3CN on Raney-Co. *Journal of Catalysis* **2009,** *263* (1), 34-41.
79. Hoffer, B. W.; Schoenmakers, P. H. J.; Mooijman, P. R. M.; Hamminga, G. M.; Berger, R. J.; van Langeveld, A. D.; Moulijn, J. A., Mass transfer and kinetics of the three-phase hydrogenation of a dinitrile over a Raney-type nickel catalyst. *Chemical Engineering Science* **2004,** *59* (2), 259-269.
80. Cocchiara, J.; Letizia, C. S.; Lalko, J.; Lapczynski, A.; Api, A. M., Fragrance material review on cinnamaldehyde. *Food and Chemical Toxicology* **2005,** *43* (6), 867-923.
81. Letizia, C. S.; Cocchiara, J.; Lalko, J.; Lapczynski, A.; Api, A. M., Fragrance material review on cinnamyl alcohol. *Food and Chemical Toxicology* **2005,** *43* (6), 837-866.
82. Letizia, C. S.; Cocchiara, J.; Lapczynski, A.; Lalko, J.; Api, A. M., Fragrance material review on cinnamic acid. *Food and Chemical Toxicology* **2005,** *43* (6), 925-943.
83. Shreaz, S.; Wani, W. A.; Behbehani, J. M.; Raja, V.; Irshad, M.; Karched, M.; Ali, I.; Siddiqi, W. A.; Hun, L. T., Cinnamaldehyde and its derivatives, a novel class of antifungal agents. *Fitoterapia* **2016,** *112*, 116-131.
84. Tzortzakis, N. G., Impact of cinnamon oil-enrichment on microbial spoilage of fresh produce. *Innovative Food Science & Emerging Technologies* **2009,** *10* (1), 97-102.
85. Cheng, S.-S.; Liu, J.-Y.; Tsai, K.-H.; Chen, W.-J.; Chang, S.-T., Chemical Composition and Mosquito Larvicidal Activity of Essential Oils from Leaves of Different Cinnamomum osmophloeum Provenances. *Journal of Agricultural and Food Chemistry* **2004,** *52* (14), 4395-4400.
86. Tsang, S. C.; Cailuo, N.; Oduro, W.; Kong, A. T. S.; Clifton, L.; Yu, K. M. K.; Thiebaut, B.; Cookson, J.; Bishop, P., Engineering Preformed Cobalt-Doped Platinum Nanocatalysts For Ultraselective Hydrogenation. *ACS Nano* **2008,** *2* (12), 2547-2553.
87. Fechete, I.; Wang, Y.; Védrine, J. C., The past, present and future of heterogeneous catalysis. *Catalysis Today* **2012,** *189* (1), 2-27.
88. Durndell, L. J.; Wilson, K.; Lee, A. F., Platinum-catalysed cinnamaldehyde hydrogenation in continuous flow. *RSC Advances* **2015,** *5* (97), 80022-80026.
89. Vinod, C. P.; Wilson, K.; Lee, A. F., Recent advances in the heterogeneously catalysed aerobic selective oxidation of alcohols. *Journal of Chemical Technology & Biotechnology* **2011,** *86* (2), 161-171.

90. Shil, A. K.; Sharma, D.; Guha, N. R.; Das, P., Solid supported Pd(0): an efficient recyclable heterogeneous catalyst for chemoselective reduction of nitroarenes. *Tetrahedron Letters* **2012,** *53* (36), 4858-4861.
91. Espro, C.; Donato, A.; Galvagno, S.; Neri, G., On the formation of cinnamyl alcohol during the hydrogenation of cinnamaldehyde under mild conditions on supported palladium catalysts. *Reaction Kinetics, Mechanisms and Catalysis* **2016,** *118* (1), 223-233.
92. Satagopan, V.; Chandalia, S. B., Selectivity aspects in the multi-phase hydrogenation of α,β-unsaturated aldehydes over supported noble metal catalysts: Part I. *Journal of Chemical Technology & Biotechnology* **1994,** *59* (3), 257-263.
93. Zhang, Y.; Liao, S.; Xu, Y.; Yu, D., Catalytic selective hydrogenation of cinnamaldehyde to hydrocinnamaldehyde. *Applied Catalysis A: General* **2000,** *192* (2), 247-251.
94. Delbecq, F.; Sautet, P., Competitive CC and CO Adsorption of α-β-Unsaturated Aldehydes on Pt and Pd Surfaces in Relation with the Selectivity of Hydrogenation Reactions: A Theoretical Approach. *Journal of Catalysis* **1995,** *152* (2), 217-236.
95. Bartholomew, C. H., Mechanisms of catalyst deactivation. *Applied Catalysis A: General* **2001,** *212* (1–2), 17-60.
96. Parkinson, G. S.; Novotny, Z.; Argentero, G.; Schmid, M.; Pavelec, J.; Kosak, R.; Blaha, P.; Diebold, U., Carbon monoxide-induced adatom sintering in a Pd–Fe3O4 model catalyst. *Nat Mater* **2013,** *12* (8), 724-728.
97. C. H. Bartholomew, R. J. F., *Fundamentals of Industrial Catalytic Processes*. 2nd edition ed.; Wiley-Interscience: 2006.
98. Maxted, E. B.; Biggs, M. S., The catalytic toxicity of nitrogen compounds. Part I. Toxicity of ammonia and of amines. *Journal of the Chemical Society (Resumed)* **1957,** (0), 3844-3847.
99. Huang, Y.; Adeeva, V.; Sachtler, W. M. H., Stability of supported transition metal catalysts in the hydrogenation of nitriles. *Applied Catalysis A: General* **2000,** *196* (1), 73-85.
100. Singh, U. K.; Vannice, M. A., Liquid-phase hydrogenation of citral over Pt/SiO2 catalysts 1. Temperature effects on activity and selectivity. *Journal of Catalysis* **2000,** *191* (1), 165-180.

Chapter 2

Experimental

2.1 Catalyst Synthesis

2.1.1 Materials

All materials used in the preparation of the catalyst series used within this thesis were acquired from Sigma Aldrich. These included tetraaminepalladium (II) nitrate as the metal precursor, fumed silica for the amorphous series, with Pluronic P-123 and tetraethyl orthosilicate (TEOS) for the SBA-15 series. Crotononitrile (99%) and cinnamaldehyde (99%) were both sourced from Sigma Aldrich, along with all reaction substrates and intermediates required for GC testing or systematic study. All solvents, specifically methanol for nitrile work and anisole for aldehyde work, were obtained from the same provider. Deionised water was produced in-house utilising a Merck Millipore purification system.

2.1.2 SBA-15 synthesis

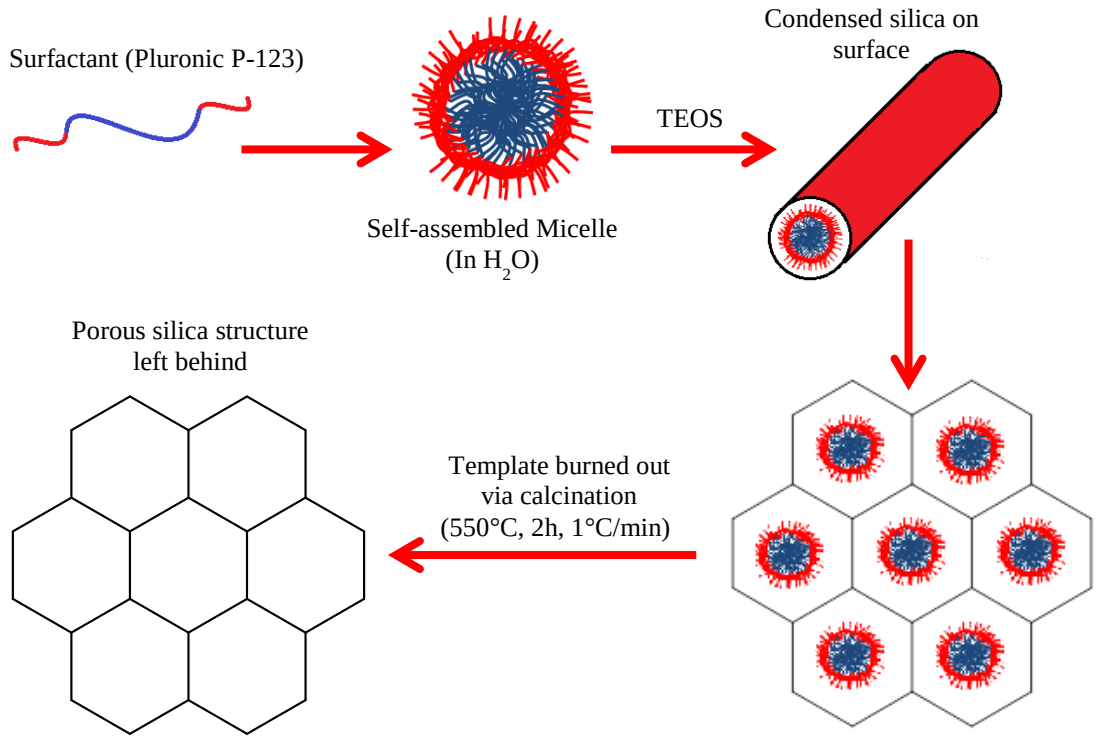

Figure 2.1 – Illustration of the process behind SBA-15 formation within solution

SBA-15 was synthesised based on work by Zhao et al. and described above in **Figure 2.1**.[1] The triblock copolymer Pluronic P-123, (20g) was added to a sealed polypropylene bottle (2 L). Deionised water (614 ml) and 12M hydrochloric acid (114 ml) were then added to the bottle to achieve an aqueous mixture of 2M hydrochloric acid.

A large magnetic stirrer flea was added to the bottle and the contents mixed at 35°C until the P-123 was fully dissolved. Tetraethyl orthosilicate (TEOS, 46 ml) was added to the dissolved mixture and the contents stirred for a further 24 hours at temperature. The resulting mixture was then aged at 80°C within an oven for an additional 24 h. Upon removal, the milky-coloured mixture was filtered and washed with ethanol to extract the suspended solid. The solid was then dried overnight at 80°C before undergoing calcination within a furnace (1°C/min ramp rate, 6h dwell at 550°C). The resulting solid support was then ground with a mortar and pestle, to result in a fine power of around 15 g.

2.1.3 Catalyst impregnation (Incipient Wetness)

To begin, a stock solution of metal precursor was prepared. Tetraaminepalladium (II) nitrate solution (10 Wt %, 4.375g, 41.11 mmol) was added to a 25ml volumetric flask. Additional deionised water was added up to the volumetric line. This stock solution was then used in the synthesis of catalyst series.

For both the amorphous silica series, and the SBA-25 series, five batches were prepared. 5g of support material were added to 50 ml beakers upon a multi-point stirrer plate, equipped with a stirrer flea of equal radius to the beaker to ensure efficient homogenisation. The previously prepared metal precursor solution was then added in varied amounts, calculated to achieve the desired metal loadings (0.1-5.0 wt. %). Additional deionised water was added to each beaker, up to a liquid content of ~12ml. This was done in order to achieve a slurry-like mixture for efficient mixing without excessive water creating issues with deposition of the salt on the support surface.

The mixtures were stirred for approximately 18 h to homogenise, before heating to 50 °C and stirring for a further 5 hours, or until sufficiently dried. The catalysts were then dried within an oven for 24 h (50°C). Upon removal from the oven, the samples were ground to a fine powder. Calcination of the samples took place within a muffle furnace (1 °C/min ramp to 500 °C, 2 hour dwell) and were then placed within a tube furnace and outgassed (N_2, 1 h), prior to reduction (10 °C/min ramp to 400 °C, 2 hour dwell, 10cm^3/min H_2). Upon completion of the reduction, the catalysts were further outgassed with nitrogen as they cooled to room temperature.

2.2 Material Characterisation

2.2.1 Titrations

2.2.1.1 Nitrogen porosimetry

Within catalysis, typically it can be agreed that the larger the surface area of the support, the more dispersed your metal nanoparticles may become, and thus the more active sites and subsequent activity you will incur.[2] One method for detecting and quantifying surface area is known as Nitrogen porosimetry. Nitrogen porosimetry is performed using the process of gas adsorption manometry. Under cryogenic conditions (liquid nitrogen, 77K), a known quantity of catalyst is placed within a porosimetry tube, a long gas tube of calibrated volume. This is then heated and outgassed at 120 °C for several hours to remove all potential gas and moisture from the surface/pores of the compound. At this point, specific volumes of nitrogen gas are introduced to the sample tube, and the change in pressure up to a maintained equilibrium is detected. In this manner the volume of adsorbed gas can be calculated. The surface area and porosity of all catalyst samples and supports for this work were calculated using nitrogen porosimetry. The machines used were both the Quantachrome Nova 4000e & 4200e. The approximate amount of sample added was within the range of 100 mg, accurately weighed to 4 decimal places.

The data obtained regarding the adsorption of nitrogen onto the surface can then be manipulated by several different equations. Surface area is calculated using the Brunauer, Emmett and Teller (BET) isotherm.[3] The BET theory asserts that a monolayer of molecules forms on the surface, and this then acts as the adsorption site for subsequent layers, infinitely. An assumption is made that the behaviour of all layers are the same as the initial monolayer, with the amount of adsorbed gas for a monolayer denoted by n_m. The total amount of adsorbed gas, n, is therefore related to the equilibrium pressure, p (**Equation 2.1**).[3] The constant C is calculated using the energy of adsorption for the initial monolayer, E_1, and subsequent layers E_L (**Equation 2.2**). Specific surface area is determined from the linear region of the BET plot between the partial pressure of 0.03-0.19 and related to total adsorbed gas, n, through the adsorbate cross section σ (**Equation 2.3**).[4]

$$\frac{p}{n(p_0 - p)} = \frac{1}{n_m C} + \frac{C - 1}{n_m C} \times \frac{p}{p_0}$$

Equation 2.1 – BET isotherm in a linear form, with p/p_0 indicating relative pressure, n for total adsorbed gas, n_m for monolayer coverage, and the constant C.[3]

$$C \approx \exp\left(\frac{E_1 - E_L}{RT}\right)$$

Equation 2.2 – Approximate definition of the constant C. Utilising the energy of monolayer adsorption E_1, and of subsequent layers E_L. T is temperature and R is the gas constant.

$$\alpha(BET) = n_m N_A \sigma$$

Equation 2.3 – Specific surface area α(BET) as calculated from monolayer coverage n_m, Avogadro's number N_A 6.022×10^{23}, and cross sectional area of the adsorptive gas σ, 0.162 nm^2 for N_2 at 77 K.[4]

Pore diameters were calculated using the desorption section of the resulting isotherm. This is achieved using the Barrett, Joyner and Halenda (BJH) method, which is an adapted version of the Kelvin equation (**Equation 2.4**).[5] $\ln p/p_0$ (Natural log of partial pressure) is used to indicate the change in gas pressure as a function of the kelvin radius, r_k, or the average curvature of the condensed gas' meniscus. V_m is the molar volume of the liquid, and γ is used for surface tension.

$$ln\frac{p}{p_0} = \frac{-2\gamma V_m}{r_k RT}$$

Equation 2.4 – The Kelvin equation, relating partial pressure, p/p_0, to the average meniscus curvature of the condensed gas, rk, which is adapted for capillary condensation in mesoporous analysis. γ is surface tension and Vm the molar volume of liquid. T is temperature, and R is the gas constant.[5]

This model must be adapted for mesoporous calculations, to assume that the pores are filled through capillary action. This model is based on the supposition that the filling of a pore is easier than the evacuation. Loss of surface area reduces adsorption, whilst this capillary action increases it. These opposing forces are accounted for by including two radii for curvature, with opposite signs related to the opposing processes.

Finally, micropore volume was determined using the de Boer 't-plot' method, which utilises the BET calculated surface area. The total adsorbed gas, n, is plotted as a function of multilayer thickness, t. The gradient of the linear segment of this t-plot graph,

prior to capillary condensation (~0.25-0.49 partial pressure), corresponds to external surface area. By subtracting this value to the BET calculated surface area, the discrepancy can be attributed to micropore volume.

2.2.1.2 Carbon monoxide pulse chemisorption

The term 'dispersion' is used to define the number of metal sites available for adsorption, as a percentage of the total number of metal atoms in the sample. Carbon monoxide (CO) will selectively adsorb onto the surface of a metal and not its support and is therefore ideal for this calculation. It has previously been determined that CO will bind to palladium in a bridging manner, meaning that an average stoichiometry of 2 is used in dispersion calculations.[6] By dosing a known volume of CO onto the surface of a catalyst, dispersion can be calculated. The total number of metal atoms (M_{tot}) can be calculated using the moles of Pd in the sample, determined by the mass of sample, the weight loading, and the molecular weight of palladium. This is then multiplied by Avogadro's number to give the number of atoms present (**Equation 2.5**). The number of metal atoms at the surface (M_{surf}) is determined using the volume of CO adsorbed per gram of the catalyst sample, and the multiplying by 2 due to the bridging alignment of the CO on palladium (**Equation 2.6**).

$$M_{tot} = n_{Pd} \times N_A$$

Equation 2.5 – Total number of metal atoms M_{tot} as calculated by the number of moles of Palladium n_{Pd}, multiplied by Avogadro's number N_A

$$M_{surf} = 2\left[\frac{V_{CO}/V_m N_A}{w_{cat}}\right]$$

Equation 2.6 – Total number of surface metal atoms calculated by the number of moles of CO adsorbed. V_{CO} is the volume of CO, V_m the molar volume, and w_{cat} the catalyst mass. The equation is multiplied by two to account for the stoichiometry of 2.

Catalysts and supports were measured using a Quantachrome ChemBET, using TPRWin software. Samples ranged from 50 mg-300 mg depending on the metal loading (the lower the loading the more sample needed for an accurate measurement). Samples

were out-gassed under nitrogen for 10 minutes, before being dried/reduced under 1 bar hydrogen at 20 ml/min 150°C for 1 hour, before being cooled to room temperature under helium. Samples were exposed to 50 µl pulses of 1 bar CO until at least three peaks of consecutive size were detected with the software (**Figure 2.2**).

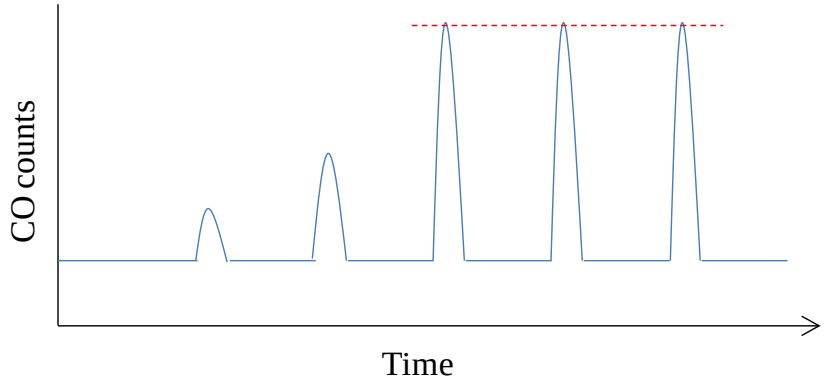

Figure 2.2 – Illustration of the raw spectrum obtained with CO chemisorption. As more CO adsorbs to the surface, less subsequent CO adsorbs, and so more is detected. Once the surface is saturated, all pulsed CO will be detected and will result in a repeating maximum peak.

2.2.2 X-ray techniques

2.2.2.1 X-ray diffraction

Metal particles consist of a repeated, ordered crystal structure. These crystal structures will diffract X-rays due to the relation between atomic distance and X-ray wavelengths. This trait is utilised in X-ray diffraction to characterise the crystal structure of a sample. This in turn can be used to evaluate the bulk phases and generate an estimate of particle size.[7] The angle at which an X-ray is diffracted off the surface of a sample depends on the wavelength of the X-ray itself and the distance between the lattice planes of the crystal structure. This interaction is defined in the Bragg equation (**Equation 2.7**).

$$\lambda = 2d \sin\theta$$

Equation 2.7 – The Bragg equation, with λ indicating the wavelength of the incident X-rays, d as the lattice plane distance, and θ as the glancing angle between the lattice plane and the incident X-ray.

Palladium, the metal of choice for the research detailed herein, has a face-centred cubic structure (**Figure 2.3**). The three most visible facets are noted as (111), (200) and (220). These are known as miller indices, and correspond to the coordinates h, k and l.

Miller indices are used as a way to describe three-dimensional crystal structures, referring to the location of the nearest atoms of a repeating unit cell. For a cubic lattice such as is found in palladium, the lattice parameters are all equal. This value can be calculated using the distance between planes determined by Braggs law (**Equation 2.8**).

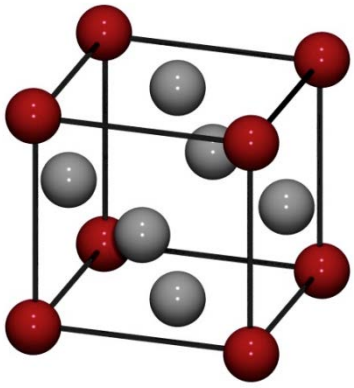

Figure 2.3 – Face centred cubic (FCC) structure

$$d = \frac{a}{\sqrt{h^2 + k^2 + l^2}}$$

Equation 2.8 – Equation indicating how the distance between lattices planes, d, can be calculated for a cubic unit cell using the lattice spacing a, and the h, k and l miller indices.

X-ray diffraction was also used as one method to determine particle size. Because the crystal structure of a metal nanoparticle is finite, these differences affect the diffraction angle of the X-rays. This in turn results in a line broadening on the spectrum. Using the Scherrer equation, an estimated particle size can be determined based on the extent of this broadening.[8] By taking the Bragg angle and the full-width half-maximum (FWHM) of the peak, and assuming a shape factor depending on the particle in question (0.9 for an assumed spherical particle), an approximate particle size is determined (**Equation 2.9**).[8]

$$\tau = \frac{K\lambda}{\beta Cos\theta}$$

Equation 2.9 – The Scherrer equation, where K is the shape factor, set to 0.9 for spherical particles. λ is the X-ray wavelength, β the full-width half-maximum (FWHM) of the peak, and θ the Bragg angle.[8]

All catalysts and supports were characterised using a Bruker D8-Advance powder X-ray diffractometer, fitted with a Cu Kα (1.54 Å) radiation source, and nickel filter.

2.2.2.2 X-ray photoelectron spectroscopy

X-ray photoelectron spectroscopy is a surface sensitive technique used for elemental analysis of samples. Because X-ray energy is within the same range as core electrons, exposing an atom to a photon with energy in excess of that of the electrons causes them to excite and eject from the atom as a photoelectron, leaving a hole within the core (**Figure 2.4***)*. This core hole is then filled by an outer electron, and its excess energy given off as fluorescence, which is covered in the next section.

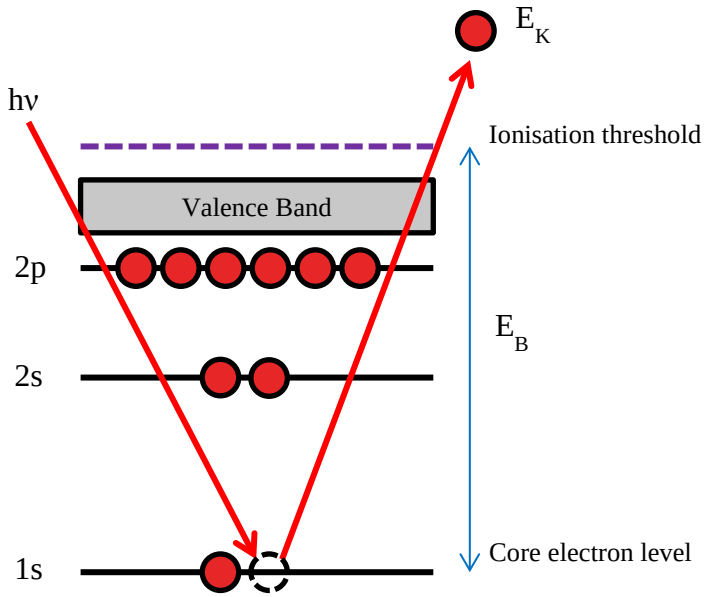

Figure 2.4 – Generation of a photoelectron using an incident X-ray photon (hν) with h representing Planck's constant, and ν the x-ray frequency. E_K is the photoelectrons kinetic energy, and E_B is the binding energy.

The detector of the XPS will then identify the kinetic energy of the released photoelectron. The binding energy (E_B) of the electron can then be calculated by subtracting the detected kinetic energy from the energy of the X-ray photon (**Equation 2.10**).[9] The binding energy of the electron is a unique fingerprint of its parent atom. Due to this, XPS analysis is an invaluable means of elemental analysis. The binding energy of the electron can be affected by bonding and oxidation states, and so detecting these shifts in kinetic energy can be used to determine these traits.

$$E_B = h\nu - E_K$$

Equation 2.10 – Relationship between an electron binding energy E_B, and the detected kinetic energy E_K of the photoelectron, with the x-ray photon energy represented as hν.[9]

The filling of the core-hole to relax the atom from its excited ionic state leads to the formation of two other states, due to the concept of spin-orbital coupling (**Equation 2.11**). For a single unpaired electron, the spin component 's' equates to ±½ and the orbital angular momentum 'l' to 0, 1, 2, 3 corresponding to s, p, d or f orbitals respectively. As such, for any state where the orbital component is > 0 with an unpaired electron present, you will observe a doublet peak. To apply this to the work herein, the XPS peaks for the Pd 3d state will display as a doublet peak relating to the $3d_{5/2}$ and $3d_{3/2}$ states.

$$j = l + s$$

Equation 2.11 – To calculate total angular momentum 'j', the vector sum of the orbital 'l' and spin 's' components must be calculated. As such, spin-orbit coupling and doublet peaks will be observed for spectra where l is > 1 and s equals ±½

XPS data was obtained for this work using a Kratos AXIS HSi instrument equipped with three X-ray sources, an Al monochromator, and a Mg and Al duel anode. The work detailed within was obtained using the Al monochromator source (1486.6 eV). Spectra were processed using CasaXPS software and corrected to adventitious carbon (285 eV). Data on aspects such as binding energy and peak separation was obtained from the National Institute of Standards and Technology (NIST) database.[10]

2.2.2.3 X-ray Fluorescence Spectroscopy

X-ray fluorescence is a bulk sensitive technique used for the elemental analysis of samples. As detailed in **Figure 3.6** for XPS, using X-rays a core electron of an atom can be excited and leaves as a photoelectron. The removal of this electron causes the structure to become electronically unstable. To counteract this, an electron from a higher valence will move to fill the core-hole left behind. When this occurs the electron will lose energy equal to that of the difference between the two orbitals. This energy is released as a photon and is referred to as fluorescence (**Figure 2.5**).[11]

As with XPS, the photon, or secondary X-ray will be characteristic of the element of origin, in much the same way as a photoelectron. By detecting the energies and ratios of the photons being detected, this can then be extrapolated into elemental analysis of the sample. Due to the low X-ray yields of lighter elements, this process is unable to detect elements lighter than beryllium (Z = 4), although most instruments will be unable to detect anything lighter than sodium (Z = 11) due to sensitivity issues.

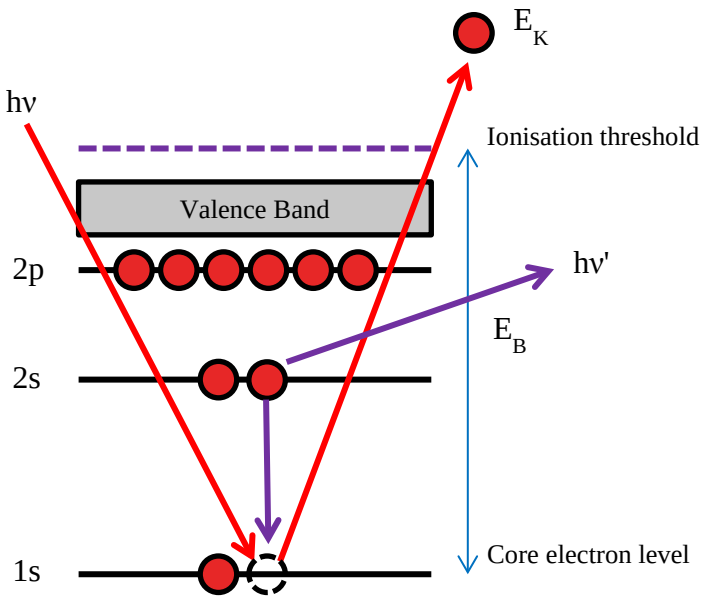

Figure 2.5 – As with XPS, a core electron is excited and released as a photoelectron. The resulting core-hole is filled by the electron of an outer valence, and the energy difference between the orbitals released as a photon.[11]

XRF data was obtained using a Bruker S8 Tiger instrument, fitted with a standard X-ray source. Preparation was simple, with powdered samples packed into PTFE holders with microfilm PTFE windows (transparent to X-rays) and placed in the device.

2.2.2.4 X-ray Absorption Spectroscopy

X-ray Absorption Spectroscopy is a technique used to generate information on the bulk structure of a sample through the use of high energy x-rays, generated through synchrotron radiation. Although this technique is hard to perform due to the rarity of establishments that can produce synchrotron radiation, there are significant benefits to the process. Notably, as this technique does not require a vacuum to proceed, in-situ analysis may be performed on reactions to track real-time effects upon the nature of the sample.[12]

By increasing the x-ray energy and tracking the absorption from the sample you can identify aspects such as the elemental phase (*ie*. Pd or PdO). In a similar fashion to XPS, once the binding energy of an electron is exceeded by the x-ray energy, it is released as a photoelectron. Specifically, for palladium we would be looking for excitation of the K-edge, at 24,365 eV. With palladium oxide, or any other form of elemental phase change, we will see a difference in the occupation of orbitals. The occupation of higher/lower orbitals will have an effect upon the intensity of the absorbance peak and can thus be detected through this technique.[13]

Once the sudden increase in absorption is detected, you will also observe several subsequent oscillations in absorption. Known as the Kronig Structure, these arise from backscattering interactions between neighbouring atoms within the sample, with electron waves clashing and forming constructive and deconstructive interference.[14] From this information, geometric data such as inter-atomic distance and coordination number can be determined.[15] The precise nature of the oscillations can be determined through computer algorithms, and with the use of the EXAFS equation, as shown in **Equation 2.12**, can be converted into the information stated above.[16]

$$\chi(k) = \sum_i \frac{\left(N_i {S_0}^2\right) F_i(k)}{k {R_i}^2} \sin\left[2kR_i + \delta_i(k)\right] e^{-2{\sigma_i}^2 k^2} e^{-\frac{2R_i}{\lambda(k)}}$$

Equation 2.12 – The EXAFS equation.[16]

XAS can be split into separate regions as defined by the actions occurring at each point. X-ray Absorption Near Edge Structure (XANES) and X-ray Absorption Fine Structure (XAFS). XANES focuses on the activity within the first 100 eV of the absorption edge, whilst XAFS is concerned with the 1000 eV range (or as far as the oscillations can be accurately analysed).[13]

Experimental analysis for XAS was performed at the Diamond Light Source (DLS). Specifically, the B18 line was used for its particular focus, a high flux versatile multi-pole wiggler, which allowed for x-rays between 4-35 keV. Pd (24,365 eV) K-edge data was obtained using solid catalyst samples arranged within a ‘washer’ o-ring and coated in x-ray translucent PTFE. Data was processed using Athena (V 0.9.1)

2.2.3 Microscopy and elemental analysis

2.2.3.1 Transmission Electron Microscopy

Transmission Electron Microscopy (TEM) is a technique which utilises a beam of electrons to provide up to atomic level resolution upon the surface of the given sample. As the electron beam is passed through the prepared ultra-thin sample, the elements present upon the surface will absorb the energy at different rates. In turn, this will result in the transmitted beams intensity varying as a function of the energy absorbed on the surface. The collected transmitted energy is then focused by a lens, to produce an image upon a

phosphorescent screen.[17] The resultant image will display different bright or dark intensities that can be attributed to each individual elemental type.

In exception to its sister technique, Scanning Electron Microscopy (SEM), TEM images are two dimensional. In addition, this technique is very sensitive to sample thickness, with results degrading as the sample gets thicker. Samples were prepared within ethanol, and vigorously shaken to disperse within the medium. Liquid was then dropcast onto a holey carbon film upon a copper grid (Agar Scientific).

Data was collected using a JEOL 2100F model instrument, with a field emission gun source running at 200 keV HT and using a Gatan digital micrograph camera. Data was processed using the imaging software ImageJ (V1.41).

2.2.3.2 Inductively Coupled Plasma Spectroscopy

Inductively Coupled Plasma – Atomic Emission Spectroscopy (ICP or ICP-AES) is a bulk elemental analysis technique. The technique relies upon the production of argon plasma. This is generated by entering the argon gas into a highly infused chamber of electromagnetic radiation, generated by high powered radio frequencies (RF). The argon is ignited by a tesla unit, and ionised within the electromagnetic field to produce plasma in the range of 7000 K.[18]

Into this argon plasma, the sample in question can be introduced. For the purposes of catalytic analysis, the sample must first be digested in a strong acid so as to be completely within the liquid phase. Upon introduction to the system, the liquid enters a nebuliser chamber where it is nebulised into a mist and introduced to the plasma. Upon interaction, the various constituents will collide with the charged plasma ions and undergo a cycle of atomic breakdown and recombination. The resultant radiation given out by this process is unique for each element within the sample, and can thus be used for quantitative analysis. The radiation is transmitted, often through optical fibres, and may undergo different analysis depending on the instrument model. In general, the radiation is separated out into a variety of wavelengths, which can be determined within the device depending on the unique fingerprint of the elements you are looking for. These wavelengths are then analysed for their varying intensity, and this can be compared against reference standards to obtain a quantitative analysis of the samples elemental composition.

Data was collected using a ThermoFisher iCAP 7000 ICP-AES. Standards were sourced from Sigma. Calibrations were consigned to an R^2 value of above 0.995 for all analysis.

2.3 Catalyst Testing

2.3.1 Nitrile selective hydrogenation

2.3.1.1 Crotononitrile hydrogenation (ambient)

To allow for a simpler medium in which to work, crotononitrile was incorporated into a solution with the chosen solvent of methanol. The amount of crotononitrile utilised depended on the parameters of the experiments, but as a general standard, a concentration of 33.6 mmol was used. For this concentration, crotononitrile (22.56 g) was measured into a 100 ml volumetric flask, and topped to the mark with methanol. Mesitylene (1 ml) was subsequently added as the internal standard for analysis. 10 ml of this stock solution was used in each subsequent experimental reaction, so as to maintain minimal human error with chemical quantities.

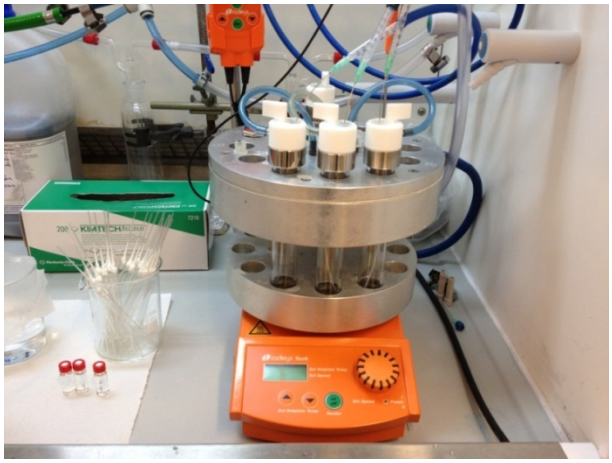

Figure 2.6 – Photograph of the original reaction setup for ambient condition testing

Initial work into the processes of nitrile hydrogenation involved the use of a test-tube 12-point Radley™ reactor. Crotononitrile stock solution (10 ml) was added into a reaction vial containing a magnetic stirrer flea, and slotted into the heating mantle (**Figure 2.6**). Temperature was set to a standard of 30°C for thermostatic conditions, with a baseline stir-rate of 800 rotations per minute (rpm). By use of a gas valve and PTFE tubing, nitrogen gas was bubbled through the solution to outgas the reaction (~ 10 min). Catalyst was added (typically 50 mg) into the vial and a flow of hydrogen replacing that of nitrogen (1 bar, 60 ml/min flow as standard). Samples were taken at key time intervals (t = 0, 5, 10, 60, 120, 180, 240, 300, 360, 420 min) *via* syringe, filtered to remove catalyst, and analysed using a ZB-50 column within a Varian 450-GC with an FID, or leading to a 240-MS if peak identification was required. Reaction variables were altered as necessary.

2.3.1.2 Crotononitrile hydrogenation (under pressure)

Figure 2.7 – Images of the Büchi Miniclave™ (Left) and Parr 5500 Autoclave (Right)

For a number of reactions, conditions were altered to observe the effects of hydrogen pressure upon catalyst activity and selectivity. To this end, pressure reactions were performed initially within a Büchi Miniclave™ reactor, and then within a Parr 5500 autoclave upon acquiring the new equipment (**Figure 2.7**). For the Miniclave™ the experimental parameters remained the same as the test-tube Radley™ reactor, but with the ability to utilise hydrogen pressures up to 10 bar.

With the standard autoclave, a larger, slightly diluted stock solution of 25 ml was incorporated to allow for more effective sampling in a larger reaction vessel. Pressures could be set between 1-130 bars, and run at temperatures up to 350°C. Perturbation was accomplished with an overhead mechanism, turning an internal impeller and reaching speeds of 1500 rpm, rather than the standard magnetic stirrer flea. Temperature was regulated by the heating manifold and controlled by the electronic display panel located to its left as displayed in **Figure 2.7**.

For both reactor types, a custom designed sampling technique was added so as to allow sample taking under pressure. Using a dip tube connected to a first valve, a small headspace tube immediately follows, with a second valve beyond it before finally attaching the exit pipe. In this way, the first valve can be opened to allow a sample into the middle-tube, before being closed and having the second valve opened to allow collection.

2.3.2 Aldehyde selective hydrogenation

2.3.2.1 Cinnamaldehyde hydrogenation (ambient)

In a similar nature to the nitrile hydrogenation stock solution, a batch of cinnamaldehyde (22.4g) with a reference standard of dodecane (1 ml) was added to a 100 ml volumetric flask, and topped to the level with the chosen solvent of anisole. As before, this allowed for 10 ml samples to be taken for each reaction and with a minimisation of human error.

Experimentation for aldehyde hydrogenation was performed within a Radley™ Starfish carousel, utilising 25 ml round bottomed flasks, with the same dip-tube setup for hydrogen bubbling. Standard reaction conditions included heating to 90 °C and stirring at 800 rpm. Samples were taken at the same time points outlined for the crotononitrile work.

2.3.2.2 Cinnamaldehyde hydrogenation (under pressure)

As with the crotononitrile work, several experiments with cinnamaldehyde involved the use of increased hydrogen pressure. As such these tests were performed within the Parr 5500 autoclave system. Parameters were the same as with the ambient reaction conditions within the Radley™ carousel (with the clear exception of pressure). Samples were run upon the Varian 450-GC, through the ZB-50 column.

2.4 References

1. Zhao, D.; Huo, Q.; Feng, J.; Chmelka, B. F.; Stucky, G. D., Nonionic Triblock and Star Diblock Copolymer and Oligomeric Surfactant Syntheses of Highly Ordered, Hydrothermally Stable, Mesoporous Silica Structures. *Journal of the American Chemical Society* **1998,** *120* (24), 6024-6036.
2. Parlett, C. M. A.; Bruce, D. W.; Hondow, N. S.; Newton, M. A.; Lee, A. F.; Wilson, K., Mesoporous Silicas as Versatile Supports to Tune the Palladium-Catalyzed Selective Aerobic Oxidation of Allylic Alcohols. *ChemCatChem* **2013,** *5* (4), 939-950.
3. Brunauer, S.; Emmett, P. H.; Teller, E., Adsorption of Gases in Multimolecular Layers. *Journal of the American Chemical Society* **1938,** *60* (2), 309-319.
4. Wedler, G., An Introduction to Chemisorption and Catalysis by Metals. Von R. P. H. Gasser. Oxford Science Publishers, Clarendon Press, Oxford 1987. XII, 260 S., paperback, £ 12.95. – ISBN 0-19-855271-8. *Angewandte Chemie* **1988,** *100* (8), 1145-1145.
5. von Helmholtz, R., Untersuchungen über Dämpfe und Nebel, besonders über solche von Lösungen. *Annalen der Physik* **1886,** *263* (4), 508-543.
6. Conrad, H.; Ertl, G.; Koch, J.; Latta, E. E., Adsorption of CO on Pd single crystal surfaces. *Surface Science* **1974,** *43* (2), 462-480.
7. Cullity, B. D.; Weymouth, J. W., Elements of X-Ray Diffraction. *American Journal of Physics* **1957,** *25* (6), 394-395.
8. Hammond, C., *The Basics of Crystallography and Diffraction*. Fourth ed.; Oxford University Press: 2015.

9. J. F. Watts, J. W., *An Introduction fo Surface Analysis by XPS and AES*. Wiley: 2003.
10. NIST X-ray Photoelectron Spectroscopy Database. http://srdata.nist.gov/xps/.
11. Glocker R, S. H., Ouantitativ Rontgenspektralanalyse mit Kalterregung des Spektrums. *Annalen der Physik* **1928,** *85*, 1089.
12. Newton, M. A.; van Beek, W., Combining synchrotron-based X-ray techniques with vibrational spectroscopies for the in situ study of heterogeneous catalysts: a view from a bridge. *Chemical Society Reviews* **2010,** *39* (12), 4845-4863.
13. Ramaker, D. E.; Koningsberger, D. C., The atomic AXAFS and [capital Delta][small mu] XANES techniques as applied to heterogeneous catalysis and electrocatalysis. *Physical Chemistry Chemical Physics* **2010,** *12* (21), 5514-5534.
14. de Groot, F., High-Resolution X-ray Emission and X-ray Absorption Spectroscopy. *Chemical Reviews* **2001,** *101* (6), 1779-1808.
15. Richards, R., *Surface and Nanomolecular Catalysis*. CRC Taylor & Francis: 2006.
16. D. C. Koningsberger, R. P., *X-Ray Absorption: Principles, Application, Techniques of EXAFS, SEXAFS and XANES*. Wiley: 1987.
17. J. John, W. H., K.L Klomparens, *Scanning and Transmission Electron Microscopy: An Introduction*. Oxford University Press: 1993.
18. Huang, M.; Hieftje, G. M., Simultaneous measurement of spatially resolved electron temperatures, electron number densities and gas temperatures by laser light scattering from the ICP. *Spectrochimica Acta Part B: Atomic Spectroscopy* **1989,** *44* (8), 739-749.

Chapter 3

Selective hydrogenation of allylic nitriles using tuneable palladium-based catalysts

–

An investigation on the effect of nanoparticle characteristics and support architecture on butylamine selectivity

3.1 Introduction

The formation of primary amines is vital in the agrochemical industry to facilitate the formation of insecticides and fungicides, to help alleviate the strain on global food production.[1] Substantial work has been done into the area of selective hydrogenation as a potential source of these chemicals.[2,3,4] Of these, the use of nitrile compounds has shown to be a promising route.

The work detailed in the following chapter follows research into the field of nitrile hydrogenation. Rather than utilising the complex multi-faceted compounds typically involved in the industrial-scale production of pesticides, this work rather focuses on a simplified analogous system. As such crotononitrile, a four carbon nitrile containing a single centralised alkene bond, was chosen due to its simplicity and ease of use for systematic studies. With the acquired data, it is hoped that the information gained can then be applied to the more complex systems utilised by Syngenta and other such manufacturers.

Herein, catalytic activity is compared over two series of catalysts, one supported upon amorphous silica, and the other upon structured mesoporous silica (SBA-15). Comparisons are also made to the current commercially used 5 wt. % Pd/C catalyst. Reaction conditions were varied to better understand the mechanisms behind the hydrogenation process, including temperature, pressure, catalyst mass and metal loading, perturbation, *etc*.

3.2 Results and Discussion

3.2.1 Characterisation of parent commercial silica support

Commercial amorphous silica is a commonly used support for many catalysts, due to its sufficiently accessible surface area, naturally non-reactive nature, versatility, and ease of use. Working with readily available amorphous silica means that tuneable catalysts can easily be synthesised, in a cost and time effective manner.

With a standard surface area, as determined by porosimetry of 230 m^2/g, there are few other distinguishable factors to reference with the blank material support.

3.2.2 Characterisation of parent SBA-15 support

As outlined in the experimental **Chapter 2**, Santa Barbara Amorphous 15 (SBA-15) is an ordered structured mesoporous silica, created as detailed prio r, and first developed by Zhao *et al*[5] and exhibiting long-range porous hexagonal channels.

3.2.2.1 Powder x-ray diffraction (XRD)

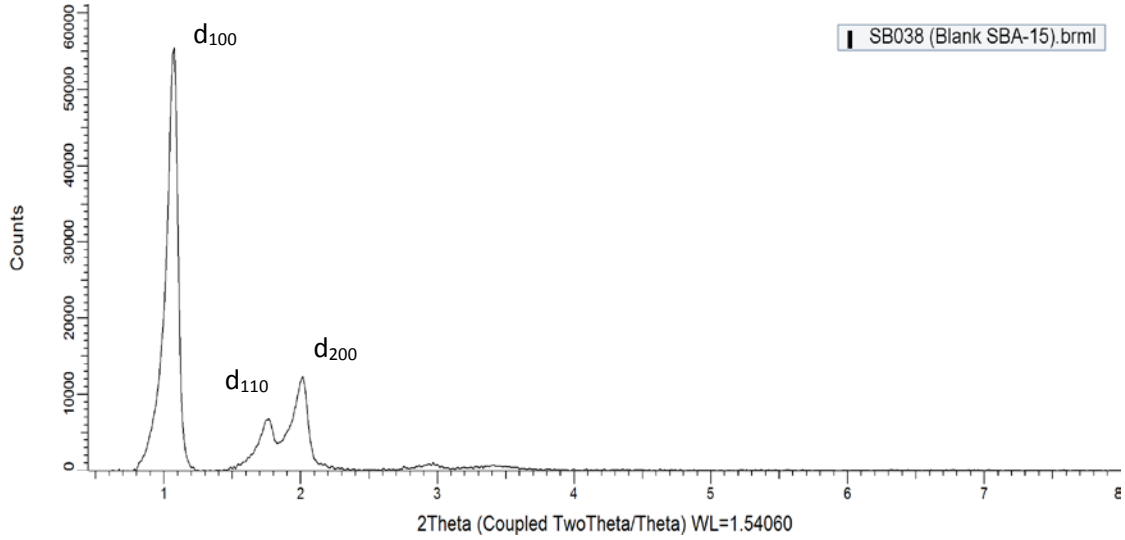

Figure 3.1 – Low angle XRD pattern for synthesised parent SBA-15 support

As highlighted with **Figure 3.1**, low angle XRD highlights the three major reflection peaks that correlate with the presence of a long-range crystallinity correlating to the presence of SBA-15, with the core d_{100}, and the minor d_{110} and d_{200} peaks. Small additional peaks at 3 θ and 3.5 θ indicate a very well ordered crystallinity.

3.2.2.2 Nitrogen porosimetry

For nitrogen porosimetry of the support mesoporous silica SBA-15, the following **Figure 3.2** shows the plotted absorption isotherm, along with the BET calculated surface area of **707 m^2/g**. Inset into the plot we can see the BJH calculated pore diameter, with the distribution shown to range from **5.0- 6.5 nm**, with an average of **5.66 nm**. These values correlate well with those obtained from samples synthesised in both literature and also within this research group.

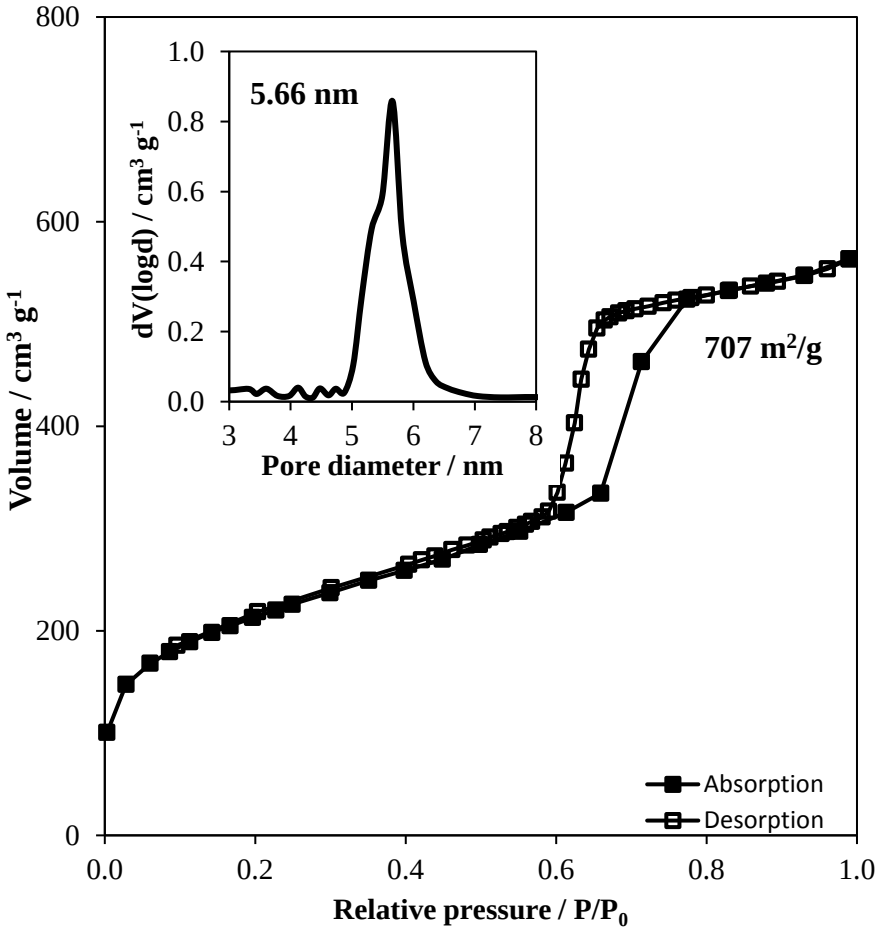

Figure 3.2 –Nitrogen absorption isotherm of support SBA-15 with BJH calculation (*inset*)

3.2.3 Characterisation of commercial 5 wt. % Pd on carbon

The basis of this chapter, and the research within, rests on the optimisation and elucidation of the nitrile hydrogenation reaction undertaken by palladium-based catalysts. As mentioned, as of writing, Syngenta utilises a 5 wt. % Pd/C catalyst for this process. The catalyst in question is a commercially available product which is purchased in bulk by

Syngenta for this reaction. As such, at the beginning of this research, we were supplied with a large batch of the material, informed that it was defined as a Pd catalyst supported upon microporous carbon catalyst, with a nominal loading of 5 wt. %. This defined the initial standard by which synthesised catalysts would be based, and by which subsequent work and findings would be based. With little known about the specific material properties of the catalyst, it was decided to characterise it to the full extent of available resources. Several techniques were utilised, including XRD (**Figure 3.3**), Porosimetry (**Figure 3.4**), and Bright/Dark Field TEM (**Figure 3.5**).

3.2.3.1 Inductively coupled plasma optical emission spectrometry (ICP-OES)

As mentioned, for bulk elemental analysis, ICP was utilised so as to break down and dissolve a known quantity of catalyst and take the relative amounts of every element within. Bulk elemental analysis of this material, nominally of **5 wt. %** Pd, shows a true bulk loading of **2.47 wt. %**. Clearly, this is a large discrepancy from the quoted nominal loading as acquired from the commercial source.

3.2.3.2 Powder X-ray diffraction (XRD)

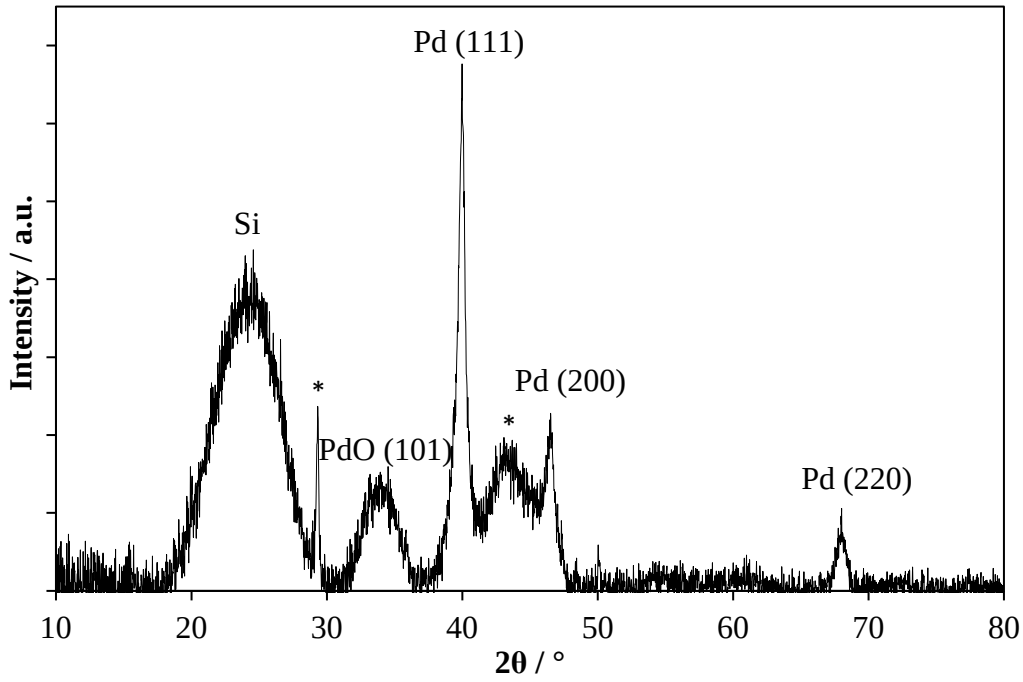

Figure 3.3 – Wide angle XRD pattern of the 5 wt. % Pd/C catalyst. Labelled to indicate corresponding Pd & PdO planes (* indicates presence of graphite).

Powder XRD, as highlighted in **Figure 3.3**, was used primarily for an indication of metal particle size, and also to affirm the presence of metal oxide, or any other potential

contaminants or species. Using the Scherrer equation, as detailed earlier in the experimental chapter, on the three primary peaks of Pd an average particle size of 16.3 nm was determined. The presence of fingerprint PdO peaks also highlights the presence of the oxide, also corroborated by XPS (**Section 3.2.3.6**). Additionally, the peaks at 29 and 43 degrees (*) indicate some small presence of graphite. One of the drawbacks with XRD is the inability to detect particles below 5 nm. As such an average particle size may be artificially increased, as these particles are not taken into account while only accommodating for large agglomerates of metal.

3.2.3.3 Nitrogen porosimetry

As shown in **Figure 3.4**, porosimetry indicated a fresh surface area of 757 m^2/g, suggesting a similar surface area to the synthesised blank SBA-15. Using a de Boer t-plot, it was deduced that microporous structure contributed almost 60% of the surface area, with 444 m^2/g, and so although it has a high surface area, much of it will be unusable within the reaction, as the pores are too small to contain palladium metal active sites, and to facilitate the movement of our model reagent, let alone the more sterically bulky compounds used in the formation of pesticides.

Analysis of a simple spent catalyst from a single ambient condition reaction, as detailed in subsequent sections, showed a significant decrease in surface area down to 400 m^2/g. This decrease is likely due to micropore blocking.

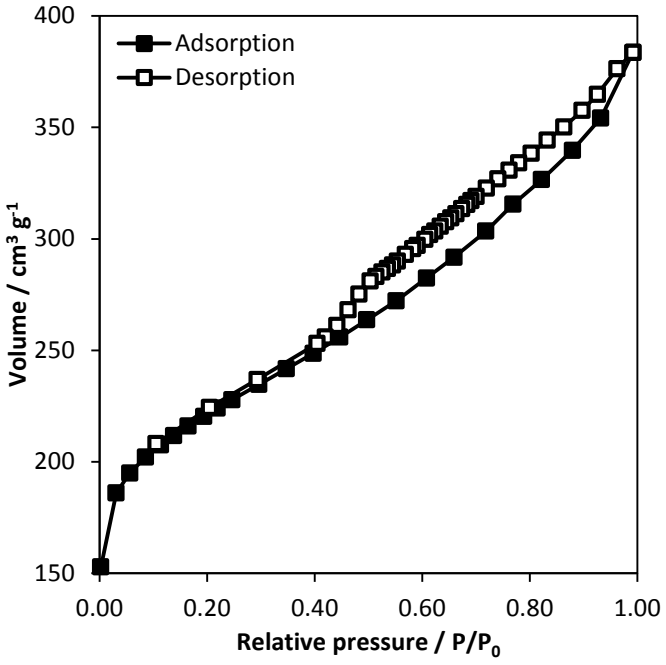

Figure 3.4 - Nitrogen sorption isotherm for 5 wt. % Pd/C

3.2.3.4 CO pulse chemisorption

For CO pulse chemisorption, the 2.47 Wt. % Pd on carbon catalyst was run with the group ChemBET and indicated a particle size of **1.95 nm**, with **57.41%** dispersion. This is a surprisingly high dispersion for such a high metal loading, but is corroborated by the very low average particle size. However, this low value does not match the one obtained through XRD analysis. In order to better understand the particle size of this catalyst, TEM was run.

3.2.3.5 Transmission electron microscopy (TEM)

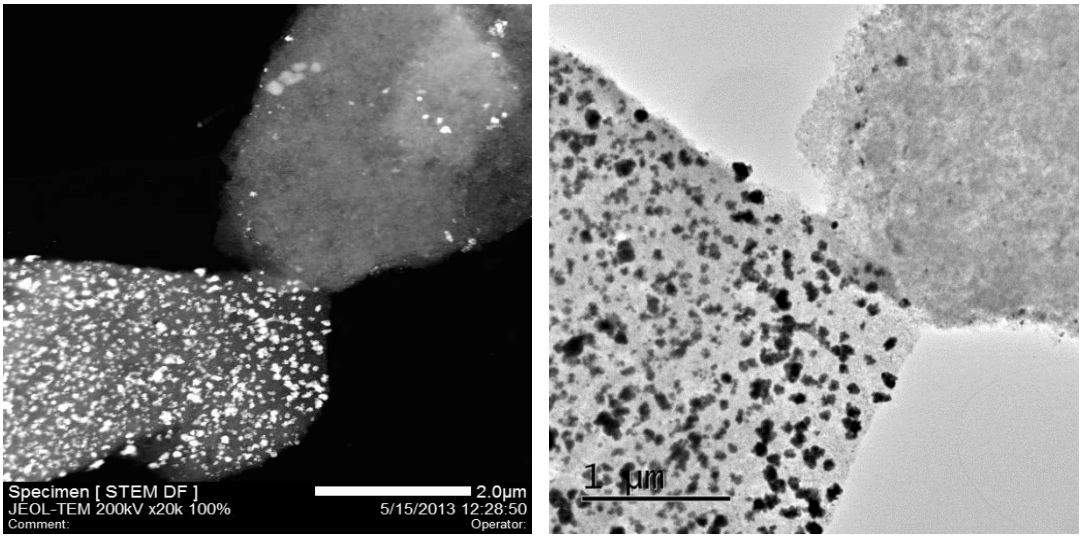

Figure 3.5 - Bright & Dark field TEM image of 5 wt. % Pd/C catalyst

For the most accurate particle size distribution, Transmission Electron Microscopy (TEM) must be used. The process by which these images are taken is again detailed in the experimental chapter. To garner an accurate particle size distribution typically at least 100, but preferably more, individual particles must be analysed within the electron microscope image, so as to avoid experimental error that may arise from analysing a small sample size. It is interesting to note in **Figure 3.5** that the 5 wt. % Pd/C catalyst shows indications of non-homogeneous distribution. Within two directly adjacent carbon particles, one has a dense population of palladium nanoparticles, whilst the other is almost entirely devoid of these nanoparticles. This is likely due to the process by which the commercial catalyst was synthesised and may in part explain some of the batch inconsistency issues evidenced by Syngenta.

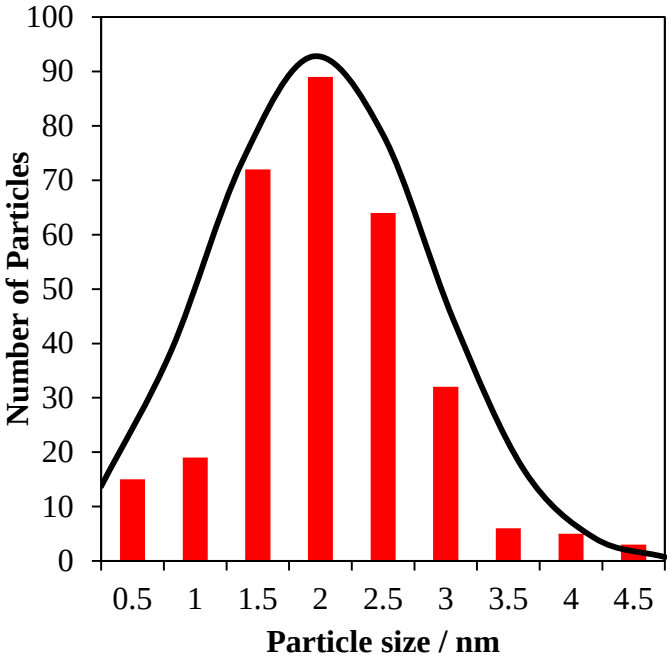

Figure 3.6 – Particle size distribution of 2.47 wt. % Pd/C as determined by TEM imaging

After collating multiple TEM images of the commercial palladium on carbon catalyst, a particle size distribution graph was created, as shown in Figure **3.6**. As is evident, the range of particles seen in the imaging technique range from 0.5-4.5 nm, with the largest percentage falling within the 2 nm range. Additionally, the mean average particle size also comes to 2 nm. This is in stark contrast to the Scherrer equation generated average particle size of 16.3 nm, as shown in the XRD spectrum. In addition, these results correlate strongly with those found using CO pulse chemisorption.

As mentioned under the XRD segment, the reasoning for this anomalous data lies within the detection limit of the technique. With all the observable particles falling below 5 nm, we can determine that none of these would be observable within x-ray diffraction, and as such we generate an artificially large value, with only the anomalous larger metal particles or clusters falling within the detectable range.

3.2.3.6 X-ray photoelectron spectroscopy (XPS)

For elemental analysis, the two techniques readily available to this group are XPS, and ICP. For surface elemental analysis, XPS was utilised. As shown in **Figure 3.7**, the overall surface content of palladium is 2.97 wt. %. This is almost always lower than the true elemental value, as XPS only penetrates a small way through the surface of the sample. Subsequently, much of the metal loading may be discounted as it is below the depth that is detectable with the technique. For a true bulk analysis one must utilise Inductively Coupled Plasma (ICP) spectrometry.

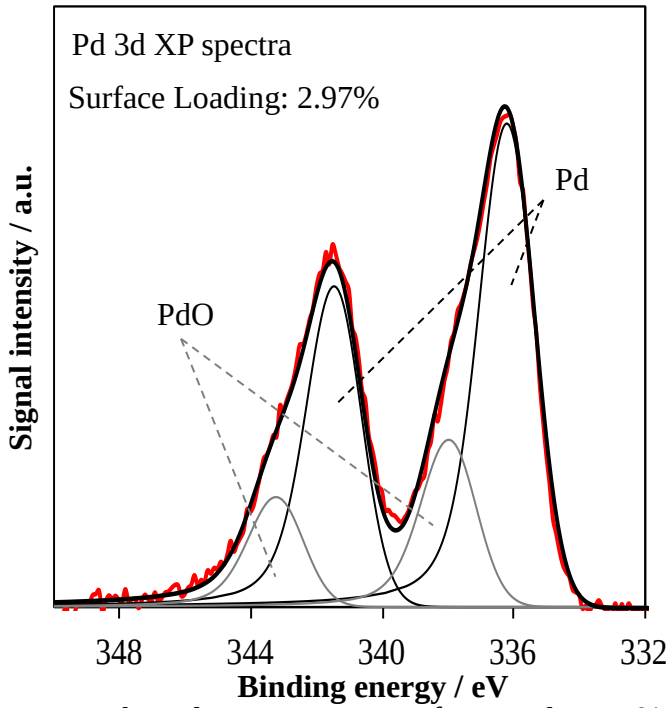

Figure 3.7 – X-ray photoelectron spectrum of nominal 5 wt. % Pd/C catalyst

3.2.3.7 Summary

In summary of the techniques detailed above, **Table 3.1** shows a condensed and detailed account of the material properties of this commercial catalyst.

5 wt. % Pd/C	
Surface Area (Porosimetry)	757 m^2/g (±75)
Micropore Surface Area (Porosimetry)	444 m^2/g (±44)
Pd Loading – Surface (XPS)	2.97 wt. % (±0.05)
Pd Loading – Bulk (ICP)	2.47 wt. % (±0.01)
Average particle size (XRD)	16.30 nm (±0.5)
Average particle size (TEM)	2 nm (±0.2)
Metal distribution (ChemBET)	57.41 % (±5)

Table 3.1 - Compendium of commercial palladium on carbon catalyst characteristics

3.2.4 Characterisation of Pd impregnated tailored supports

With the carbon-supported catalyst provided by Syngenta, sourced from an industrial supplier, it would be difficult to fully explore the activity and behaviour of the reaction. This was due to the difficulty of obtaining a support identical to that used in the catalyst, thus making it impossible to effectively reproduce the catalyst and safely alter factors such as loading without dealing with unaccounted variables from the support. Thus,

in an effort to better understand the mechanisms behind the reaction, new catalysts were synthesised with the flexibility to have key components altered to better understand how each factor affects the reaction as a whole.

Amorphous silica was chosen as the ideal support for this work, for the initial set of catalysts, for a multitude of reasons. From a general standpoint, the chemistry of silica is much better understood than that of carbon supports. This allows for far simpler analysis and makes the subsequent catalytic activity much easier to attribute to a specific trait. Furthermore, it gives access to a markedly wider range of morphologies and can be tailored to incorporate mesopores and macropores with tuneable sizes. Silica is also acid tolerant and relatively thermally stable, making it more desirable as it can be utilised under a wider range of conditions that carbon-based supports. A series of catalysts was produced with varying loadings of palladium, ranging from 0.1 wt. % up to 5 wt. %. In line with the flexibility of porous structure and surface area, it was also decided that the synthesis of SBA-15-supported catalysts would allow us to investigate the effect that mesoporosity has upon the activity of these catalysts in the chosen reactions. In the same manner as with the amorphous silica, a series of catalysts with the same varying loadings of palladium metal were synthesised.

3.2.4.1 Inductively coupled plasma optical emission spectrometry (ICP-OES)

With ICP, as detailed in the experimental **Chapter 2**, a sample of the catalyst is dissolved and passed through the spectrometer, whereby the parts per million (ppm) of each element are collated and relayed to the user. From these values, the metal loading of a catalyst can be extrapolated, as shown in **Table 3.2**.

Catalyst Series	Nominal Loading (wt. %)	ICP Loading (wt. %)
Pd/SBA-15	**0.1**	**0.09**
	0.5	**0.43**
	1.0	**0.88**
	2.0	**1.75**
	5.0	**3.87**
Pd/SiO_2	**0.1**	**0.12**
	0.5	**0.59**
	1.0	**0.93**
	2.0	**1.87**
	5.0	**4.61**

Table 3.2 – Overview of the ICP generated wt. % of Pd compared to nominal values

As is evident, there is a small discrepancy between the nominal loading applied to the support, and the calculated value after impregnation. With the exception of the highest SBA-15 loading, the trend is linear, and the difference is typically quite low, as evidenced in **Figure 3.8**. As is expected, the bulk loading evidenced here is consistently larger than the quoted XPS surface loading, due to aforementioned issues with penetration depth.

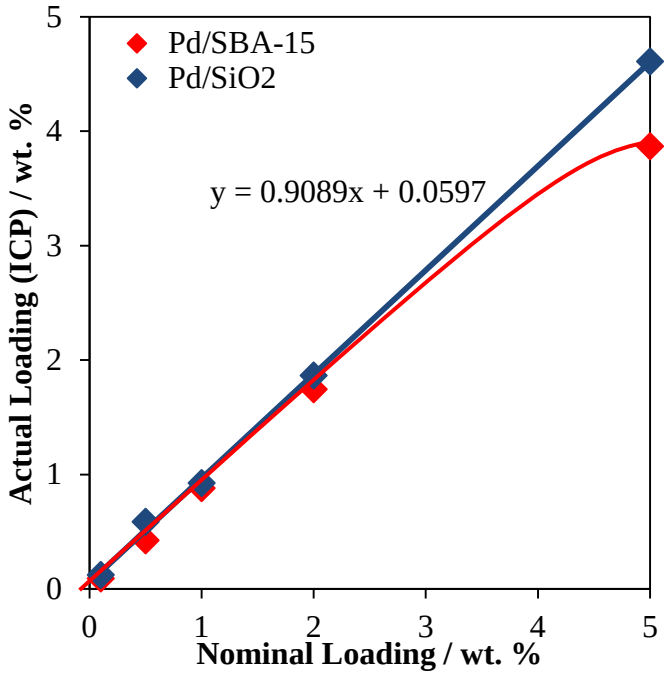

Figure 3.8 – Plotted overview of the difference between nominal loading determined in the experimental method, and ICP analysed Pd loading of the resultant catalyst.

3.2.4.2 Powder X-ray diffraction (XRD)

With powder XRD, as shown in the previous section on support characterisation, it is possible to deduce long range crystallinity within a material. This same principle can be applied to metal impregnated materials, in order to both confirm the presence of a metal, and also to extrapolate the average particle size of the metal through the use of the scherrer equation as outlined in **Chapter 2**.

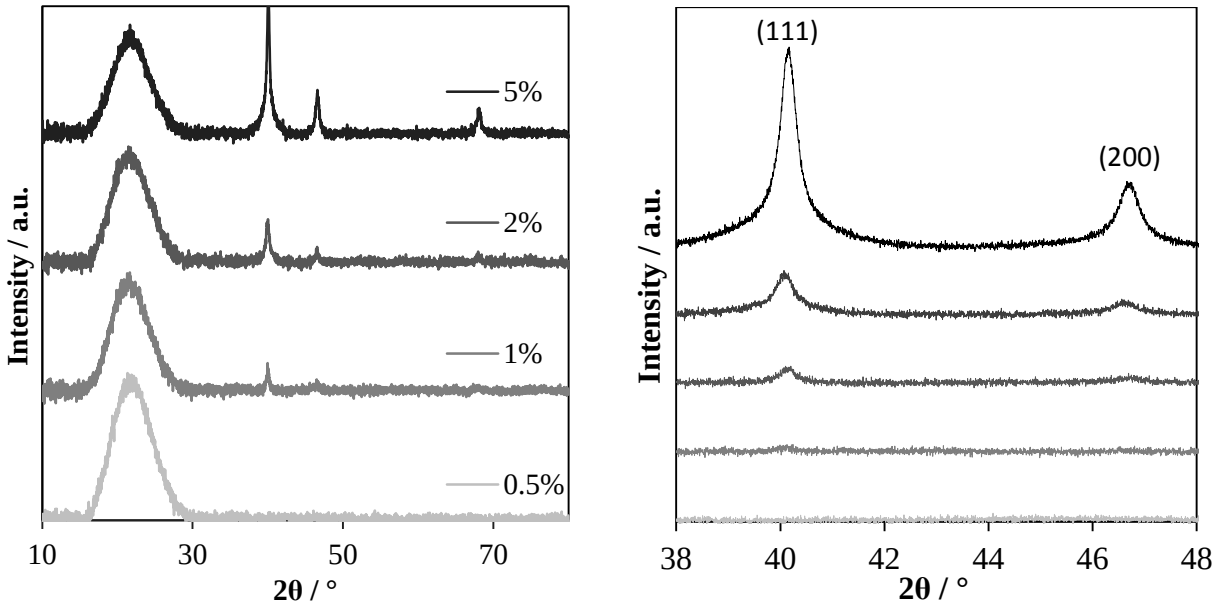

Figure 3.9 – Background subtracted stacked wide angle XRD plot of palladium upon amorphous silica support (*left*) and a higher resolution of the d_{111} and d_{200} Pd region (*right*)

With the amorphous silica catalysts, as shown in **Figure 3.9**, you can see the clearly apparent peak correlating to the presence of silica at just over 20°. As with the commercial Pd/C catalyst, the three subsequent peaks at 40, 46, and 68degrees correlate to the d_{111}, d_{200}, and d_{220} reflections respectively. What can be immediately noted for this series is the significant shortening in the peak signal as the metal loading decreases. This effect becomes so pronounced that only the nominal 1 wt. % loading and above are detectable. In terms of explanation, this means that only these loadings have particles greater than 5 nm, as that is the lower detection limit of the technique. To consider it from another angle, this also means that the lower loadings all contain particles below this level.

With the Scherrer equation and taking the average from all three Pd peaks, the average particle size for the nominal catalysts are detailed below in **Table 3.3**.

Nominal Loading	5 wt. %	2 wt. %	1 wt. %	0.5 wt. %	0.1 wt. %
Avg. Particle Size	15.7 nm	14.6 nm	10.2 nm	-	-

Table 3.3 – Average palladium particle size compared against the nominal metal loading

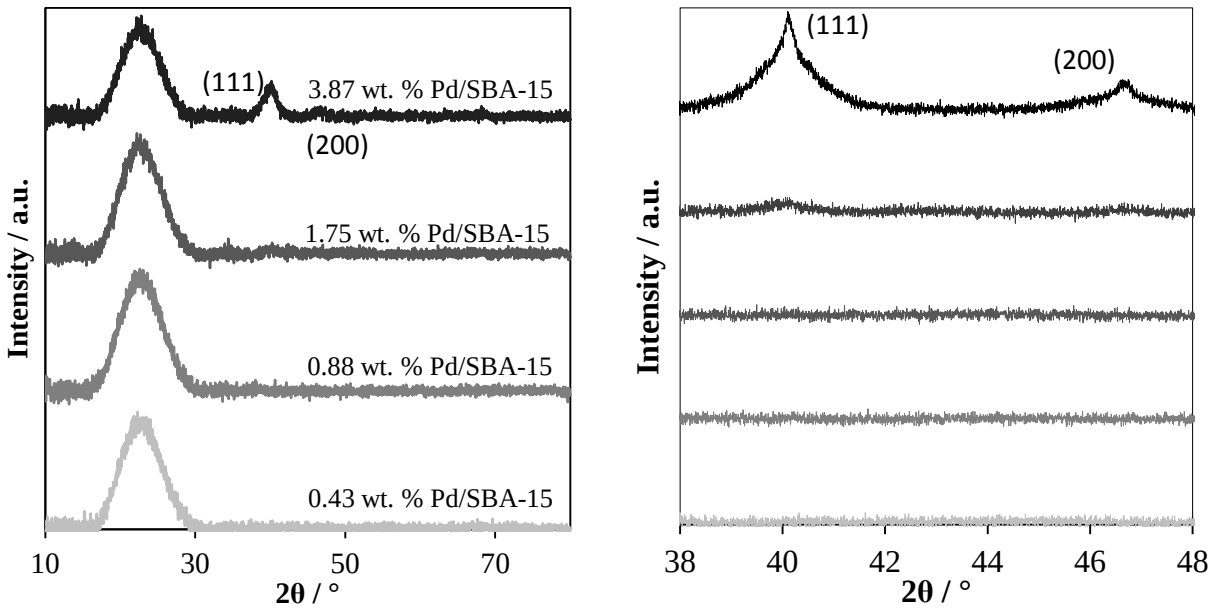

Figure 3.10 – Stacked wide angle XRD plot of palladium upon SBA-15 support (*left*) and a high resolution scan of the d_{111} and d_{200} Pd peak region (*right*)

When looking at the XRD spectra for the SBA-15 supported catalysts (**Figure 3.10**), as with the amorphous silica, the large peak at ~20 degrees indicates the obvious presence of silica. Notably, whereas the top three loadings on the amorphous silica displayed notable Pd metal reflections, only the highest loading catalyst has a calculable particle size, as it is the only one with metal peaks that can be distinguished from the background noise. As with the other series, this suggests the particles are all generally very small. For the highest loading, the nominal 5 wt. % catalyst, the average metal particle size can be calculated at **6.85 nm**. The knowledge that metal particles on the SBA-15 support appear to be smaller is likely due to the much larger surface area available to the metal.

3.2.4.3 Nitrogen porosimetry

Nitrogen porosimetry, as outlined in **Chapter 2**, was utilised to generate accurate surface area data. In addition, pertinent information such as pore diameter can be generated for the mesoporous SBA-15 support. Nitrogen (N_2) isotherm data was generated, and the plots stacked for ease of comparison, as shown in **Figure 3.11** for the amorphous silica series and **Figure 3.12** for the SBA-15.

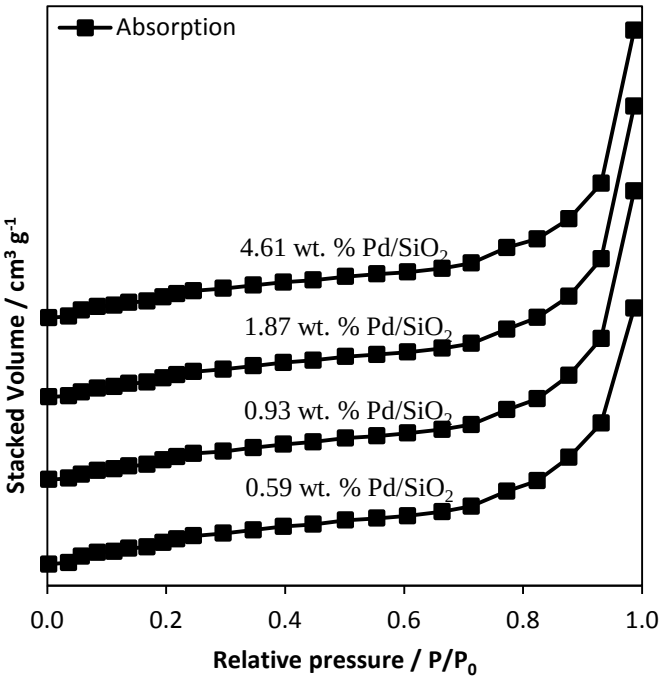

Figure 3.11 – Offset stacked N_2 isotherm plot for Pd/SiO_2 catalyst series

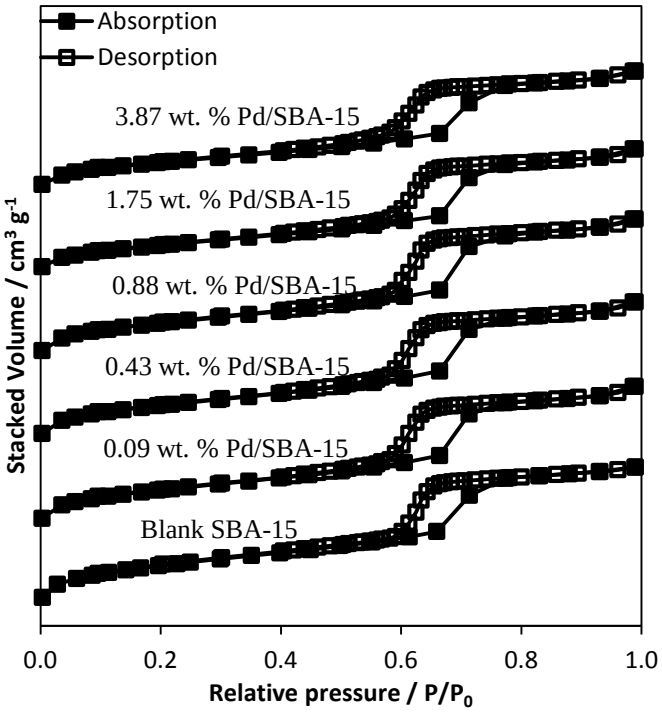

Figure 3.12 – Offset stacked N_2 isotherm plot for Pd/SBA-15 catalyst series

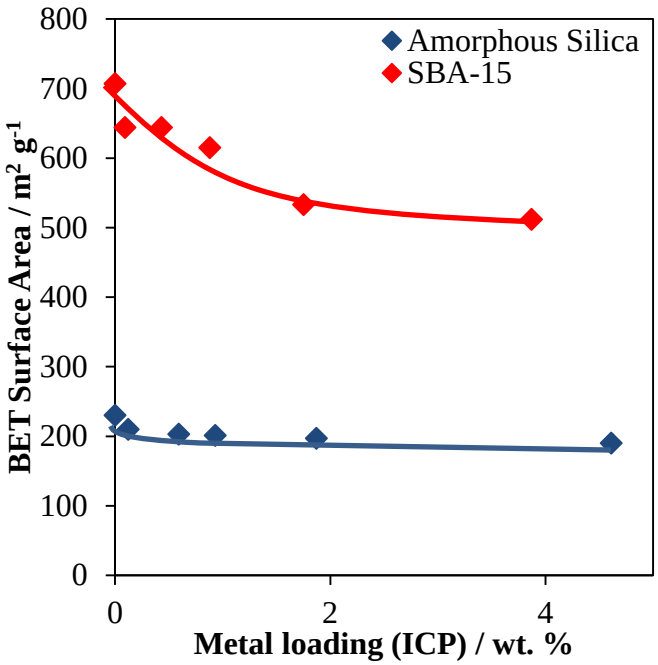

Figure 3.13 – Plotted view of the respective BET calculated surface area for both catalyst series using ICP calculated loading and porosimetry generated surface area.

Using a multi-point Brunauer-Emmett-Teller (BET) calculation, the comparative surface area of each catalyst was generated, and then shown as above in **Figure 3.13**. The surface area of the blank support always undergoes a marked decrease in surface area upon introduction of the metal nanoparticles. Then, upon addition of further metal to increase the loading wt. %, we see a continued decrease, though on a smaller scale. This can be explained by the presence of the metal nanoparticle on the surface blocking a portion of the surface area as it is deposited upon the surface. Initially, these particles will be quite dispersed and will take up a large initial percent of the surface. Larger metal loadings however will usually result in larger nanoparticles rather than additional individual sites. As such the initial trends effect is diminished. This effect is particularly prevalent in the SBA-15, due to its high count of micropores being easily blocked by the metal particles.

Another calculation than can be performed is to generate the Barrett-Joyner-Halenda (BJH) isotherm. With this you can generate a plot which details the pore diameter distribution of the sample material, along with identifying the median average pore diameter. For the amorphous silica samples there is no generated pore structure, so this method is only applicable to the mesoporous SBA-15. The generated data was stacked and plotted as in **Figure 3.14 below**. Upon comparison it is clear that the average pore diameter maintains at a fixed value of approximately **5.5 nm**. The lack of any particular

change to the pore diameter suggests that there is little to no pore blockage or coating occurring as more metal is added to the support.

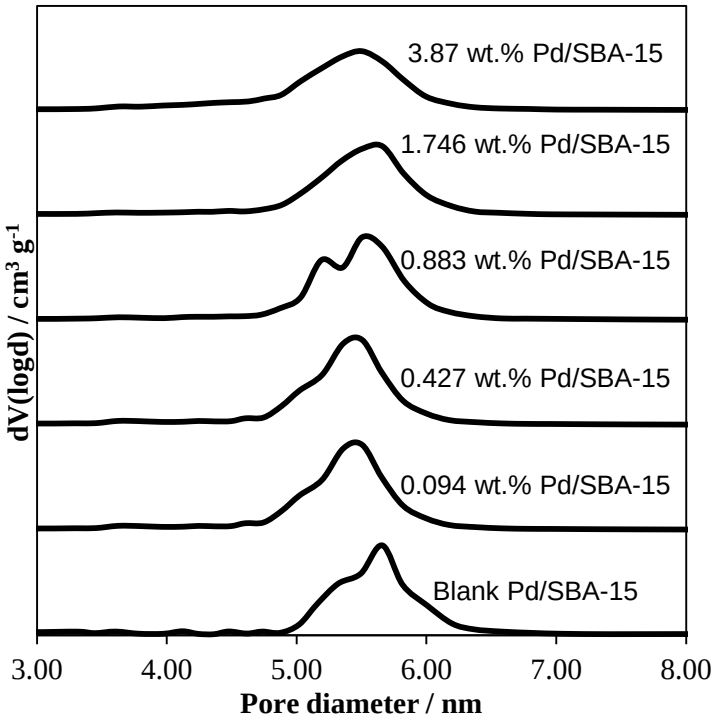

Figure 3.14 – Offset stacked plot of the BJH calculated pore size distribution for SBA-15 series of catalysts including the blank support.

3.2.4.4 CO pulse chemisorption

For pulse chemisorption with carbon monoxide (CO), as detailed in the experimental section, the data acquired can be combined with information such as accurate metal loading to determine the metal dispersion upon the supporting material. As detailed in **Table 3.4**, we can see a clear trend of decreasing metal dispersion as the loading increases. This conforms to findings typical in literature and within the group, with low loadings lending themselves towards small, highly dispersed particles. With higher loadings, the metals will collect together into larger particles and occupy less of the materials surface, as highlighted in the decreasing dispersion values.

	0.1 wt. %	**0.5 wt. %**	**1.0 wt. %**	**2.0 wt. %**	**5.0 wt. %**
SiO_2	40.2	37.7	25.1	22.0	8.9
SBA-15	49.1	42.4	37.6	32.1	28.7

Table 3.4 – Calculated metal dispersion percentage compared to nominal metal loading

3.2.4.5 Transmission electron microscopy (TEM)

With Transmission Electron Microscopy (TEM) it is possible to observe the catalytic material down to the atomic level. As such this is a useful technique for both confirming any ordered porous structure such as the characteristic honeycomb structure of mesoporous silica (SBA-15) in **Figure 3.15**, and also to directly observe the metal nanoparticles upon the surface as in **Figure 3.16**, outlined as contrasted spots of light or darkness upon the backdrop of the support structure. By these means, it is also possible to measure the diameter of the particles, and generate a particle size distribution by measuring a large demographic of them over a TEM sample grid.

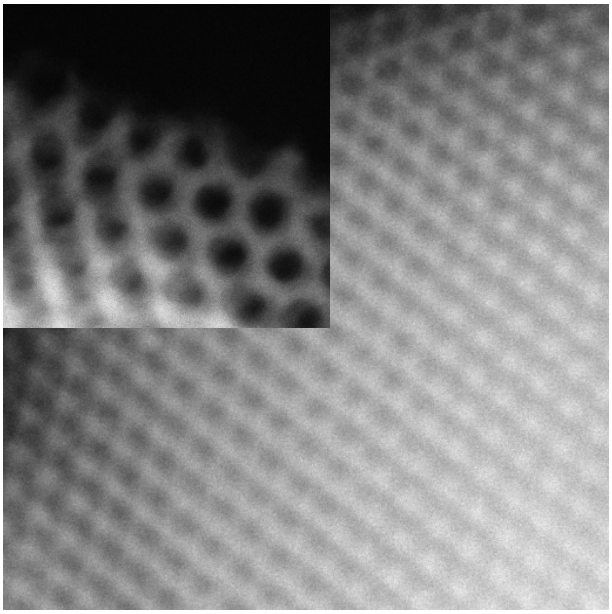

Figure 3.15 – TEM image of blank SBA-15 support highlighting the hexagonal structure

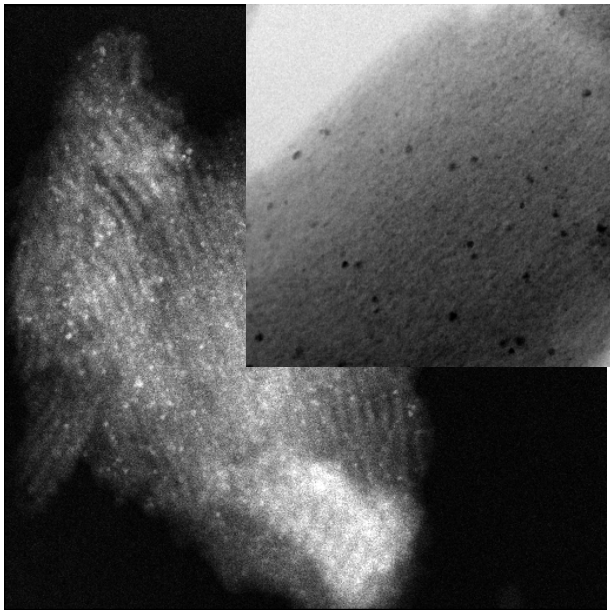

Figure 3.16 – TEM image of a Pd impregnated SBA-15 support in Bright and Dark Field

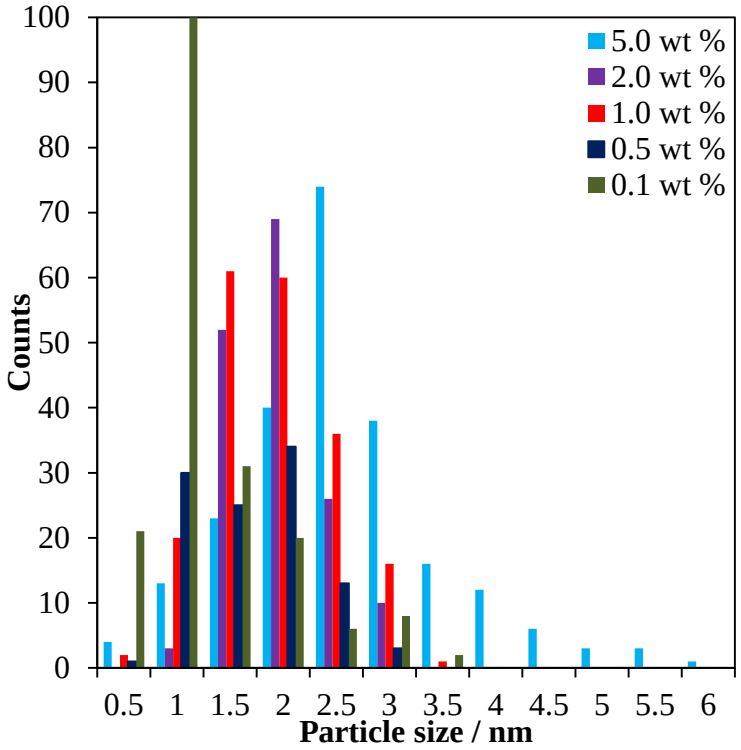

Figure 3.17 – Particle size distribution as determined by TEM for amorphous silica supported Palladium catalysts

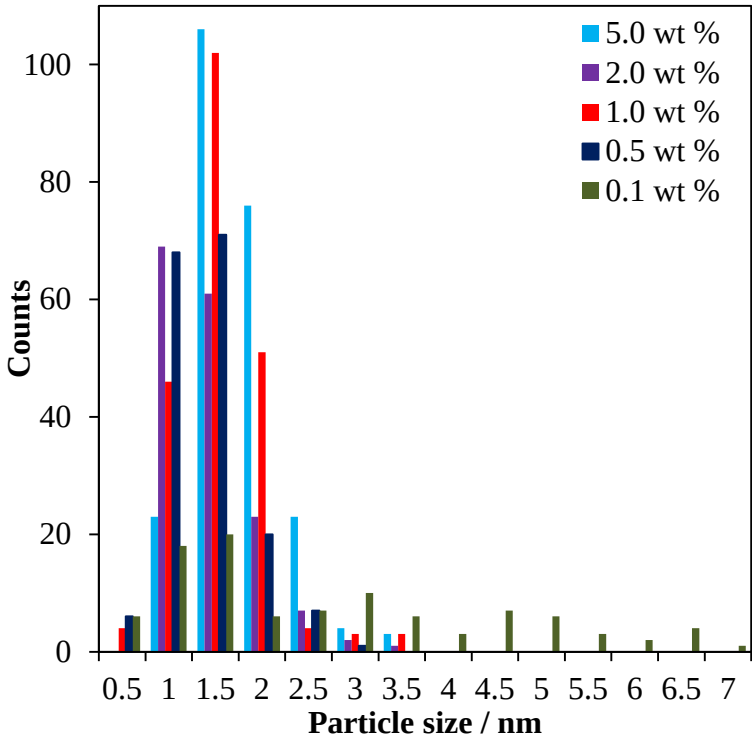

Figure 3.18 – Particle size distribution as determined by TEM for SBA-15 supported Palladium catalysts

By imaging samples of each synthesised catalyst with the TEM, and determining the particle size distribution of each one using the imaging software 'Image J', plotted distributions can be generated, along with normalised distribution plots as shown above, for both the amorphous silica (**Figure 3.17**) and SBA-15 supports (**Figure 3.18**).

As is evident in the data above, the particle size distribution of palladium metal upon both the amorphous silica and SBA-15 supports is very small, with all metal loading values giving particles that rarely extend beyond around 3.5 nm. By taking the average from the normalised distribution we can plot a graph that compares the average particle size against the metal loading of the catalyst, as detailed below in **Figure 3.19**.

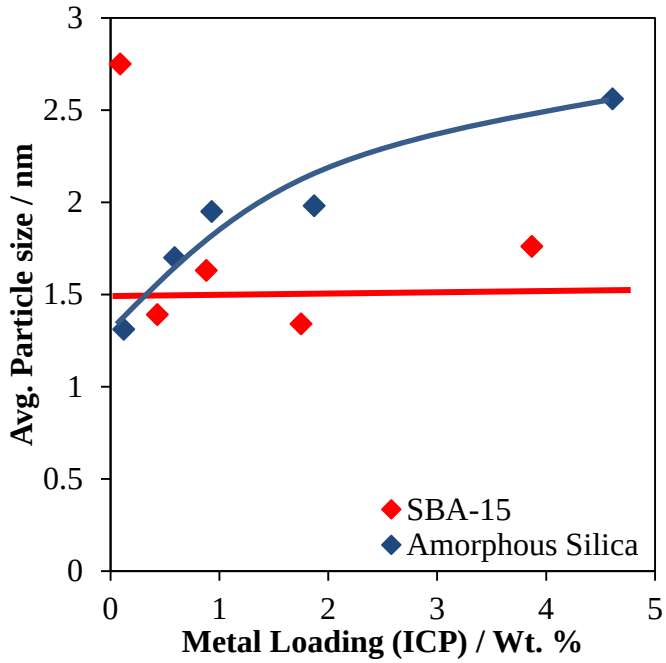

Figure 3.19 – Condensed plot of the mean particle size from TEM for catalysts on both amorphous silica and SBA-15

By observing the data in this way it becomes clear that there is very little in the way of alteration to the average particle size of the catalyst, regardless of the metal loaded onto the support. With amorphous silica we observe a steady upward trend from 1.3 nm up to 2.5 nm. This slow increase is likely due to the much lower surface area available with this support, and so the particles will naturally agglomerate into larger ones as more metal is added. In comparison, aside from an erroneous value for the lowest loading SBA-15 catalyst, the particle size has no discernible trend and remains much the same at around 1.5 nm. The reason for this can also be explained with surface area.

With such an excess of surface area in comparison to the amorphous silica, a supposition can be made that as more metal is added, there still remains plenty of 'free' surface area that can be occupied, thus reducing the need for particles to increase in size. If larger amounts of metal were to be added we would see that this trend would eventually end, and begin to reflect the pattern shown for the amorphous silica catalysts.

On comparison of the particle size distribution calculated from TEM, and the value generated by the Scherrer equation upon the XRD pattern, we observe a stark difference. Whilst the majority of the catalysts have metal particles which are undetectable within XRD, we do observe peaks within the highest catalyst loadings. XRD generates particle sizes of 6.85 nm for the highest SBA-15 catalyst, and up to 15.7 nm for the highest loading on amorphous silica.

Clearly, these values disagree heavily with the TEM generated particle sizes which indicate 2.5 nm and 1.75 nm for the highest metal loading amorphous silica and SBA-15 respectively. In this situation the most likely reasoning is that the highest loading catalysts contain some small sections in which large agglomerated clusters of palladium metal can be found.

Though these clusters might be uncommon anomalies upon the support, their presence could easily affect the XRD data with their presence during the scans, and thus artificially inflate the value generated in the Scherrer equation. Indeed, without these particles, based on the average size generated by TEM, we would not see any palladium peaks within a diffraction scan at all. As such it is considered in this author's opinion, best to consider the TEM values as the more accurate of the two, as we have first-hand observable data for these, calculated by hand.

3.2.4.6 X-ray photoelectron spectroscopy (XPS)

As mentioned within both the experimental chapter (Chapter 2) and with the previous section on the palladium on carbon catalyst, XPS is used as a surface elemental analysis technique. As shown in **Figure 3.20**, the spectra can be plotted and the weight % of each element can be generated. For both series we can observe that there is a steadily increasing loading in line with the nominal loading.

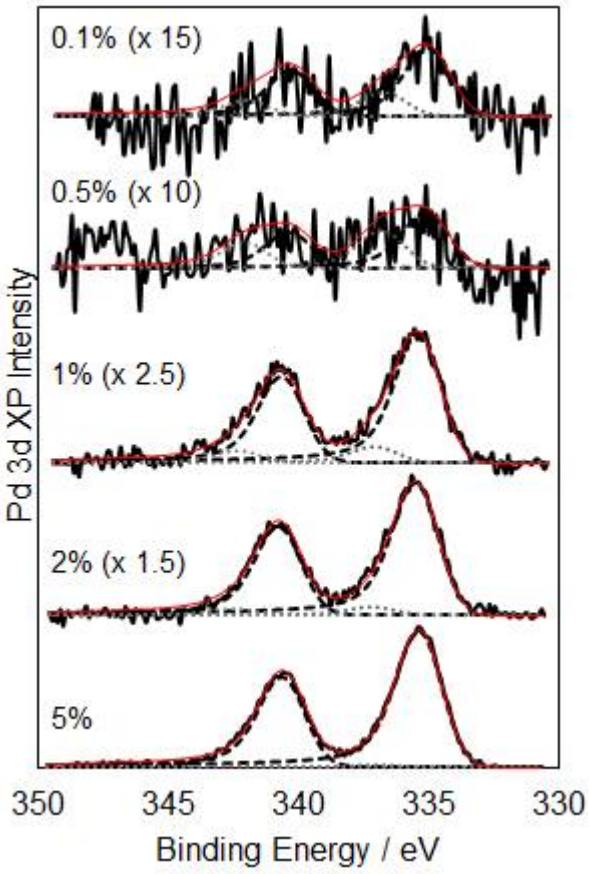

Figure 3.20 – Stacked XPS plots for the Pd/SBA-15 catalyst series, indicating increased metal loading from top to bottom 0.1-5 Wt.%. Magnification used for ease of representation, indicated within brackets.

3.2.4.7 Summary of data

With the culmination of the characterisation data detailed in this section, the following tables (**Table 3.5** & **Table 3.6**) contain the condensed data for both catalyst series.

Pd/SiO_2	**0%**	**0.1%**	**0.5%**	**1%**	**2%**	**5%**
Surface Area (Porosimetry) [m^2/g]	**230**	**210**	**203**	**201**	**197**	**190**
Micropore Area (Porosimetry) [m^2/g]	**31**	**31**	**32**	**30**	**31**	**31**
Pd Surface Loading (XPS) [wt. %]	**-**	**0.08**	**0.16**	**0.51**	**0.72**	**1.74**
Pd Bulk Loading (ICP) [wt. %]	**-**	**0.12**	**0.59**	**0.93**	**1.87**	**4.61**
Average Particle size (XRD) [nm]	**-**	**-**	**-**	**10.2**	**14.6**	**15.7**
Average Particle size (TEM) [nm]	**-**	**1.31**	**1.70**	**1.95**	**1.98**	**2.56**
Metal Dispersion (ChemBET) [%]	**-**	**40.2**	**37.7**	**25.1**	**22.0**	**8.9**

Table 3.5 – Summary of data for the Pd upon amorphous silica catalysts

Pd/SBA-15	**0%**	**0.1%**	**0.5%**	**1%**	**2%**	**5%**
Surface Area (Porosimetry) [m^2/g]	**707**	**644**	**644**	**615**	**533**	**512**
Micropore Area (Porosimetry) [m^2/g]	**256**	**160**	**160**	**140**	**104**	**101**
Pore Diameter (Porosimetry) [nm]	**5.66**	**5.51**	**5.51**	**5.51**	**5.66**	**5.5**
Pd Surface Loading (XPS) [wt. %]	**-**	**0.1**	**0.13**	**0.53**	**0.85**	**1.98**
Pd Bulk Loading (ICP) [wt. %]	**-**	**0.09**	**0.43**	**0.88**	**1.75**	**3.87**
Average Particle size (XRD) [nm]	**-**	**-**	**-**	**-**	**-**	**6.85**
Average Particle size (TEM) [nm]	**-**	**2.75**	**1.39**	**1.63**	**1.34**	**1.76**
Metal Dispersion (ChemBET) [%]	**-**	**49.1**	**42.4**	**37.6**	**32.1**	**28.7**

Table 3.6 – Summary of data for the Pd upon SBA-15 catalysts

3.2.5 Crotononitrile hydrogenation

Due to the importance of creating a process that is both effective and environmentally friendly or 'green', initial experimental efforts were put into ensuring that experiments were run with the intention of reaching both significant reaction rates and high selectivity towards the desired amine product, whilst maintaining as close to ambient conditions as possible. With this in mind, initial work was performed at effectively room temperature and pressure. To begin, preliminary work with the commercial Pd/C catalyst showed a propensity towards the hydrogenation of the C=C bond which defines the bulk structure of crotononitrile (CrCN). In this way its two isomeric cis & trans forms are converted to one saturated compound, N-butyronitrile ^{n}(BuCN). At ambient conditions, with a thermostatic temperature of 30°C and 15 ml/min H_2 (1 bar), no evidence for the nitrile hydrogenation was observed. In an attempt to determine if the C=C bond was either causing issues with surface alignment, or in consumption of available hydrogen, the process was tested by running pure butyronitrile (BuCN) as the substrate. The results further enforced the notion of inactive amine formation, with no conversion of reagent (within ~2% GC error) or erroneous peaks noted from GC analysis.

Having determined that only C=C hydrogenation of CrCN could proceed within these conditions, other possible ways to tailor the conditions had to be considered, in an attempt to first facilitate any amine formation at all, and then to optimise its yield. Firstly, the effect of increased catalyst mass within the reaction medium was explored (**Figure 3.21**). Predictably, this experiment showed that as the mass of catalyst was increased, so too was the conversion of crotononitrile (**Figure 3.22**).

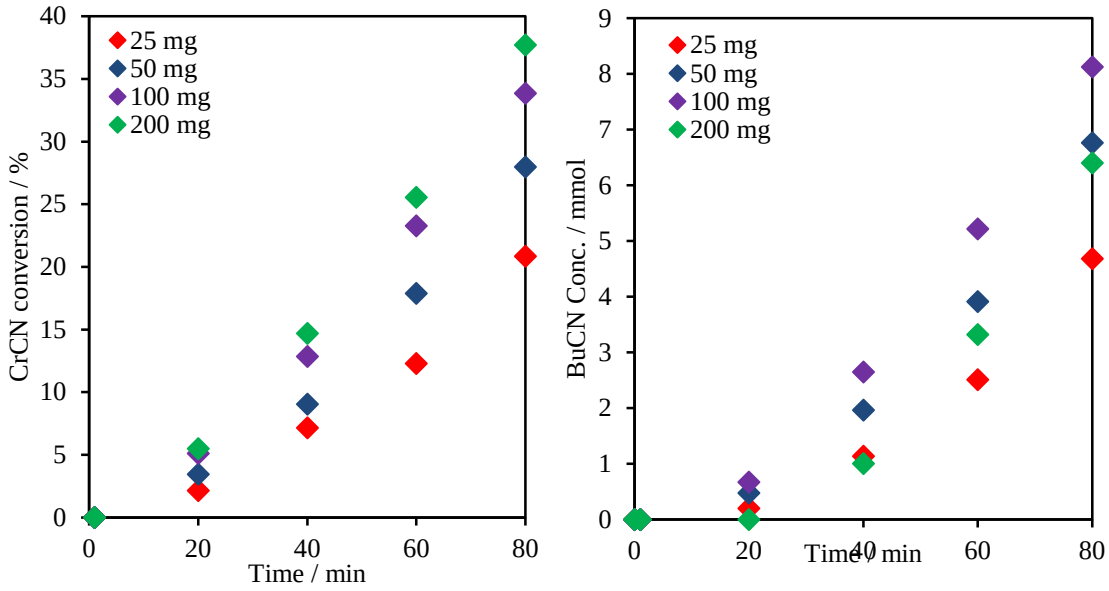

Figure 3.21 – Initial tests for crotononitrile conversion (left) and the production of butyronitrile (right) under thermostatic 30 °C, 800 rpm, and 15 ml/min H_2.

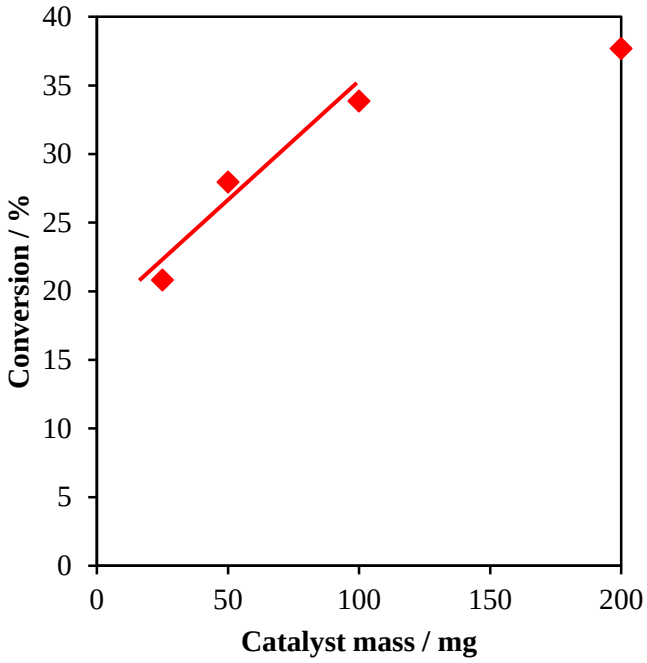

Figure 3.22 – Total CrCN conversion as a function of Pd/C catalyst mass from 25-200 mg (30 °C, 800 rpm, 15 ml/min H_2, 80 minute sample.)

Interestingly, it was noted that the overall conversion of CrCN followed a linear trend with increase in catalyst mass up to 100 mg, at which point the trend begins to plateau. This likely suggests that the limit reached here is in the accessibility of hydrogen rather than the number of active sites present within the reaction. Additionally, the detectable production of butyronitrile followed the same trend, with the exception of the 200 mg run. This could be due to an erroneous data-point, but in this author's opinion it is likely to suggest that due to the volume of the catalyst, it is retaining some of the product upon its surface, as no other product peaks can be detected through GC analysis. At no point in these tests were any amines detected, either through GC analysis or through testing of the spent catalyst material using characterisation techniques for the tell-tale amine moieties. Further work would have to be done to determine if amine yield was even a possibility under these ambient-like conditions.

In an effort to determine if the presence of palladium oxide was detrimental to the reaction in any way, the effects of pre-reduction of the catalyst were explored. Initial synthesis of the silica catalysts should not have allowed for any oxide, but some may have formed over time from exposure to air. Additionally, the commercial Pd/C contained a significant quantity of PdO (**Fig 3.7**). Results from two comparative reactions indicated that there was negligible change from the pre-reduction and removal of oxide from the

catalyst (**Figure 3.23**). It is suggested that regardless of whether the oxide is poisoning or totally inactive, the presence of such large quantities of hydrogen gas under reaction conditions easily converts to pure palladium with such a rate as to make the pre-reduction needless.

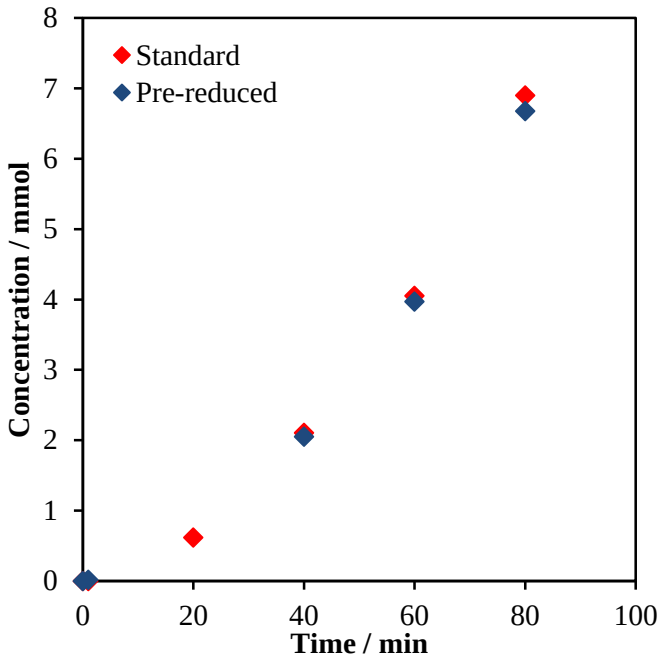

Figure 3.23 – BuCN production over fresh and pre-reduced 2.97% Pd/C catalyst (30 °C, 800 rpm, 100 mg catalyst, 15 ml/min H_2, 80 minute sample.)

Having determined that pre-reduction would have no effect upon the activity of the commercial catalyst, the next logical step was considered to be altering the reaction conditions themselves. The effect of altering the temperature, from the base standard of 30°C, up to 60°C, yielded predictable results. Butyronitrile still indicated no evidence of conversion, while the crotononitrile double bond was hydrogenated at a higher rate as temperature increased. A doubling of temperature elicited an almost double initial rate (**Figure 3.24**). To be able to calculate activation energy, the Arrhenius equation (**Equation 4.1**) was used. By taking the natural log of the initial rate (k), and plotting them as a function of 1/T in Kelvin, we get an Arrhenius plot. Using the gradient of the trend-line, which corresponds to $-E_a/R$, and multiplying this value by the gas constant R (8.314 J K^{-1} mol^{-1}), we obtain an activation energy for the reaction of 16.07 kJ/mol. This value is significantly lower than the typical non-catalytic cleavage of a C=C bond,[6] and falls in line with quoted values in literature and within the group for palladium hydrogenations.

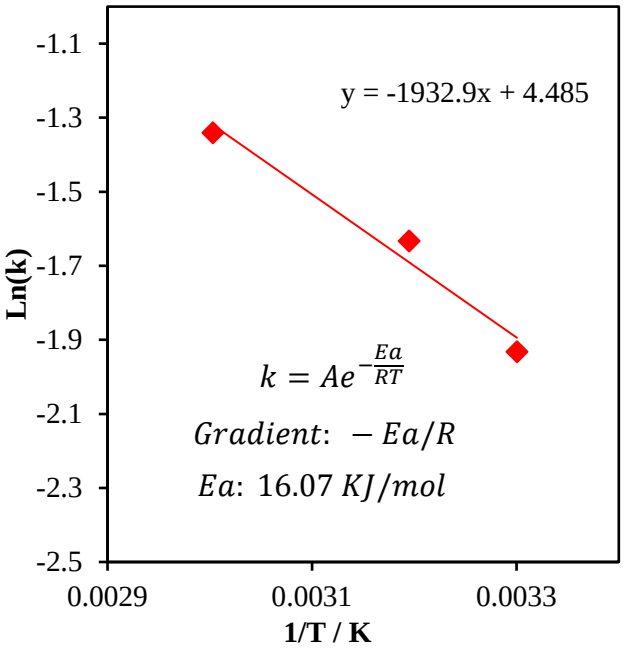

Figure 3.24 – Arrhenius plot of crotononitrile hydrogenation under ambient pressure (30-60 °C, 800 rpm, 100 mg catalyst, 15 ml/min H_2, 80 minute sample.)

$$k = Ae^{-\frac{Ea}{RT}}$$

Equation 4.1 – The Arrhenius equation

The work so far focused predominantly on the activity of the commercial Pd/C, and identifying some of the parameters which would affect the rate of reactions and attempting to alter the selectivity. Having exhausted the avenues of research with a commercial catalyst, it was then time to begin focusing upon the tuneable silica-supported catalysts synthesised for this work.

Under the same conditions as the commercial Pd/C, the reaction was tested with each catalyst on the amorphous silica support at the three different temperatures previously used in the Arrhenius plot; 30°C, 40°C and 60°C. Their initial rates were calculated and plotted against the palladium loading of the catalysts (**Figure 3.25**). It is evident that increasing the temperature also increases the rate, as expected. All temperatures showed evidence of diminishing returns in regards to the initial rate achieved. This trend is similar in nature to that seen with increased catalyst mass, as the rate determining step in this reaction is then the accessibility of hydrogen, not the number of active sites. With the results of this experimental set, it was decided to utilise the nominal catalyst loading which provided the best rate as a comparison of the metal needed to synthesise it, 2 wt. %.

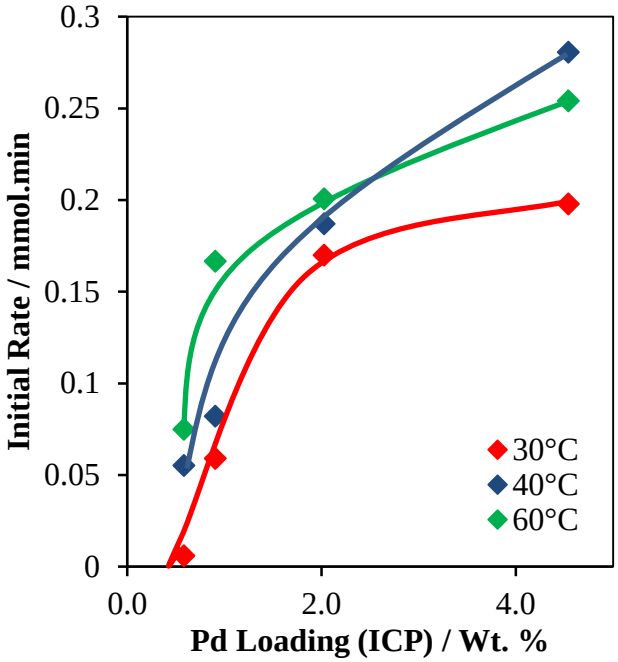

Figure 3.25 – Temperature dependence of CrCN hydrogenation initial rate as a function of Pd/SiO_2 loading (30-60 °C, 800 rpm, 100 mg catalyst, 15 ml/min H_2, 80 minute sample.).

Working on prior research reported in both the literature and within the group, the standard stirrer speed for ambient pressure reactions within a Radley set-up was 800 rpm. In an effort to identify if this was the most effective speed to work at, or if in fact the mass-transfer limit is reached as a lower level of perturbation, a series of tests were run at varying speeds. The experiments were run with both the highest loading fumed silica catalyst, and the commercial Pd/C catalyst (**Figure 3.26**).

Within the setup of a Radley reactor, any speed exceeding 800 rpm started to cause disturbances in the rotation of the rare-earth magnetic stirrer flea and as such was discounted for higher speeds. On observation of the data we can determine that there is a linearly increasing trend for both catalysts, running in parallel with a trending augmentation of rate using the silica based catalyst between 200-800 rpm.

Attempts at running a 900 or 1000 rpm test yielded the aforementioned issues with the magnetic flea and thus make it difficult to confirm if mass transfer limit was achieved. However, the conversion rates over time that were obtained followed in close agreement to that at 800 rpm. Based on the reported literature and previous work within the group it was agreed that 800 rpm be the standard for work going forward, until the issue of stirrer stability could be addressed.

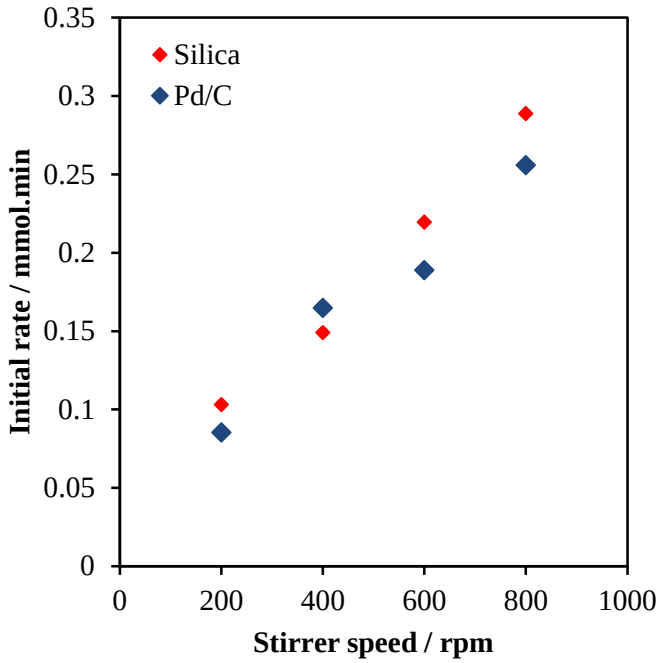

Figure 3.26 – Stirrer speed dependence of CrCN hydrogenation initial rate as a function of Pd loading over fumed silica and carbon supports (30 °C, 100 mg catalyst, 15 ml/min H_2.).

3.2.5.1 Probing the reaction pathway

Previous work both within the group and that reported in the literature have denoted a particular reaction sequence for the hydrogenation of crotononitrile, as shown in full for **Figure 3.27**.[7,8,9,10] In order to ascertain this if this was the true process, and to determine if any additional reactions were taking place, a series of experiments were run, utilising both the starting material and also the subsequent intermediates. In this way it was determined that starting from butyronitrile garnered no additional rate or selectivity.

Although the primary imine itself cannot be purchased due to its instability, reactions with butylamine produced zero products, and thus confirmed its requirement for progression. Similarly, reactions containing dibutylamine could not proceed, and tributylamine undergoes no additional steps if reacted alone. These reactions also confirmed that the amine to imine step is not reversible, although this was to be expected.

The conclusion of these experiments was the confirmation of the reaction profile, with reassurance that the presence of one or more species do not have any unforeseen detrimental effects and most importantly that imine is the key step in this reaction proceeding, without the possibility of a reverse reaction occurring under these conditions.

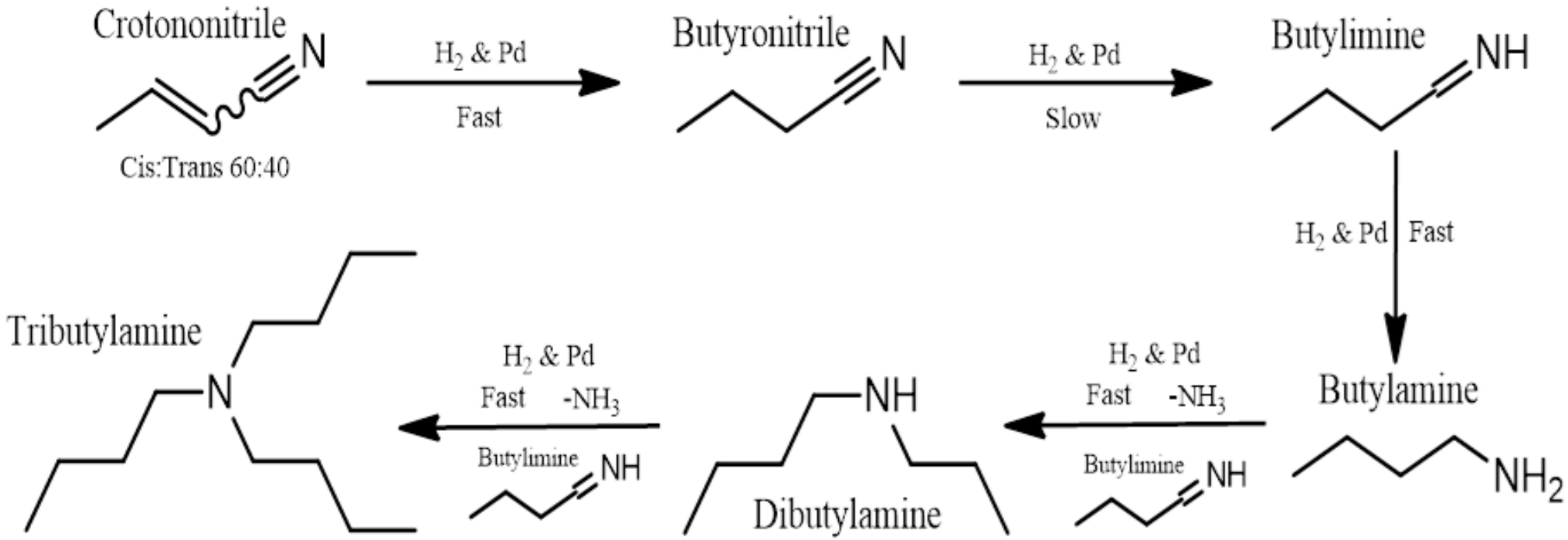

Figure 3.27 – Proposed reaction scheme for the catalytic hydrogenation of crotononitrile (Adapted from literature).[10]

3.2.5.2 Effect of H_2 pressure

To reiterate the initial desires of this chapter, the hope was to achieve hydrogenation of the nitrile bond under as close to ambient conditions as possible. Work up to this point clearly indicated that working under these mild conditions yields easy C=C hydrogenation but has absolutely no effect upon modifying the selectivity towards nitrile hydrogenation. As a result, it was decided to begin work within a Parr autoclave system. With this, experiments could be run at higher pressures (exceeding 100 bar), whilst also allowing for higher temperatures and a more uniform perturbation due to the installed impeller rod.

Initial reactions within the Parr autoclave, with 1 bar of hydrogen injected into the system, showed reaction rates in general agreement with that obtained from bubbled hydrogen within a Radley reactor. The initial rate was slightly faster within the autoclave, likely due to the much easier infusion of hydrogen gas when within an autoclave as opposed to the slightly more outdated technique of bubbling hydrogen through.

Preliminary tests within the autoclave were done with the view to observe any potential changes to the activity over varying catalyst mass within the reaction. As mentioned before, with the Radley system it was found that 100 mg of the Pd/C catalyst was the limit before reaching the mass-transport limitation whereby extra active sites had no effect. Under the pressurised system, two sets of reactions were run under both 'ambient' 1 bar H_2, and at the higher pressure of 10 bar H_2 (**Figure 3.28**).

When considering the 1 bar H_2 set we can immediately see some differences from the bubbled Radley reaction. Previously the reaction rate limit was achieved at 100 mg, but here we see that the point is reached at only 50 mg. This suggests that although the rate is slightly higher than within a bubbling reactor, the access to hydrogen at 1 bar stifles the total initial rate that can be achieved.

This concept is further reinforced when considering the 10 bar H_2 reaction set. Here we see a significantly higher initial rate, with a plateau at 100 mg of catalyst. This suggests that at this pressure, under a standard stirrer speed of 800 rpm, we have similar hydrogen diffusion to that seen with a bubbling flow reaction. As a result, subsequent work was performed with 100 mg of catalyst within the reaction medium.

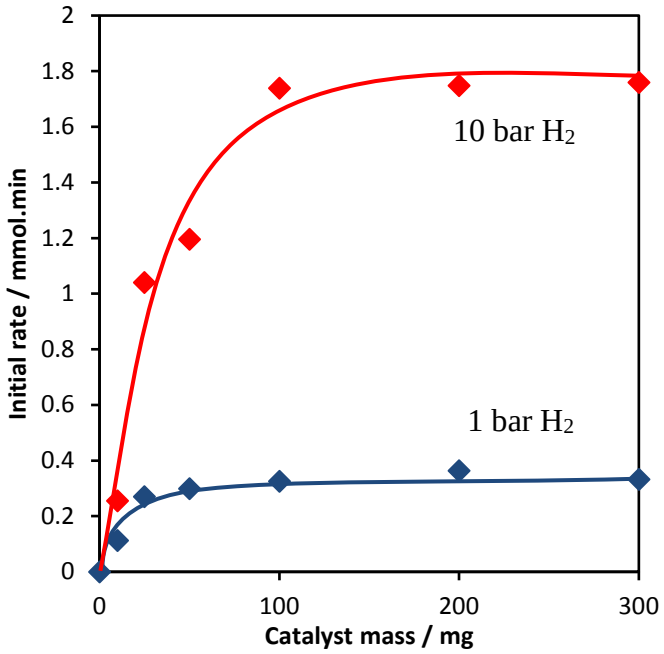

Figure 3.28 – Catalyst mass test within a Parr autoclave at both 1 and 10 Bar H_2, mixed with an overhead stirring impeller. (30 °C, 800 rpm, 0-300 mg catalyst)

As mentioned, a stirring speed of 800 rpm was utilised when testing the effect of catalyst mass on the reaction rate due to the precedence already set in previous reactions. However, with use of the Parr autoclave also included the use of a new type of perturbation system. In order to ascertain if the hydrogen accessibility changes between a magnetic stirrer and an impeller blade, a similar stirrer-speed test was run within (**Figure 3.29**).

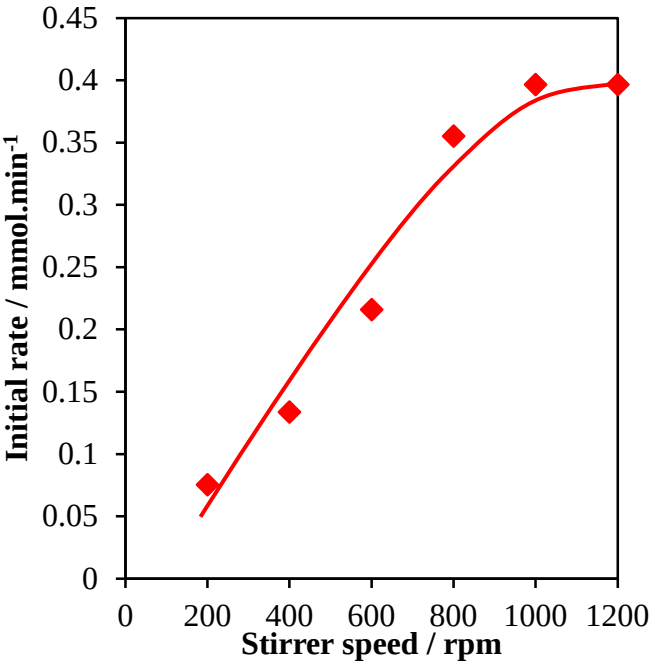

Figure 3.29 – Hydrogen perturbation test within the same Parr autoclave system

As evidenced by the data, it is apparent that the limit of hydrogen accessibility is achieved at just above 800 rpm, justifying the decision to work at this level. Any further increase in speed has a diminished effect upon the initial rate, and plateaus at 1200 rpm. Having determined the ideal stirrer-speed and catalyst mass to utilise, along with the previous knowledge on the ideal metal loading, work progressed into observations of the effect of increased temperature and pressure within the hydrogenation reaction.

To begin with, tests were performed whilst maintaining an 'ambient' pressure level of 1 bar H_2, whilst altering the temperature of the reaction. However, within the autoclave it was possible to exceed the limits set by the boiling point of methanol (~65 ° C). A series of systematic experiments were run, altering the temperature of the reaction whilst maintaining a liquid-phase medium through autogenous pressure. The results gained from this showed that whilst the C=C hydrogenation step could be performed as ever increasing rates, with full consumption of the reagent occurring within minutes, there was still no evidence of any nitrile hydrogenation.

With this evidence in mind, a series of tests were performed where the temperature was retained at a thermostatic level, while the hydrogen pressure was drastically increased up to 100 bar H_2. Upon observing the data gathered, it was clear that although the C=C hydrogenation pathway was occurring, we still could not generate any selectivity towards the nitrile bond. After referring to the literature on this process, it was decided that for the reaction to proceed we would need a combination of higher temperature and pressure.

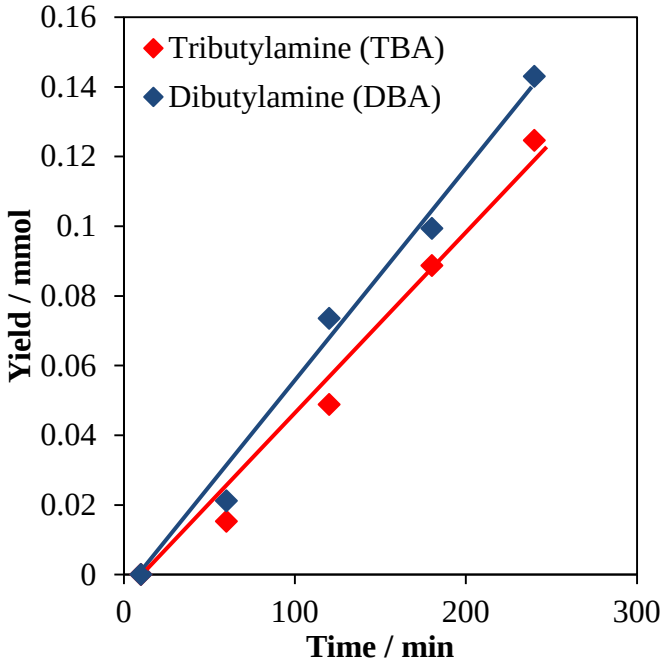

Figure 3.30 – Evidence of amine formation at 30 bar H_2 (120 °C, 800 rpm, 100 mg cat.)

With initial hydrogen pressure experiments, as shown previously, it was noted that although initial rate for C=C hydrogenation increased, no amines were produced. However, upon increasing the pressure to 20 bar and above, we began to observe peaks correlating to the secondary and tertiary amine products. By increasing the pressure again to 30 bar H_2, even higher yields of the two amine structures were produced. From a series of systematic experiments it was determined that the optimum temperature conditions at this pressure was in the range of 120 °C, with any higher temperature exhibiting diminishing returns.

Having successfully detected both secondary and tertiary amines, focus was then turned towards running a systematic set of experiments over a range of pressures, under the temperature and conditions that were known to generate detectable yields of amine products. With that in mind, a series of tests run at 120 ° C and spanning from 0-60 bar H_2 at 10 bar intervals were performed (**Figure 3.31**). As the experiments were run, the generated data was expected to show a steady increase in the total yield of amine product as a function of pressure, or to observe some sort of plateauing event at a certain point.

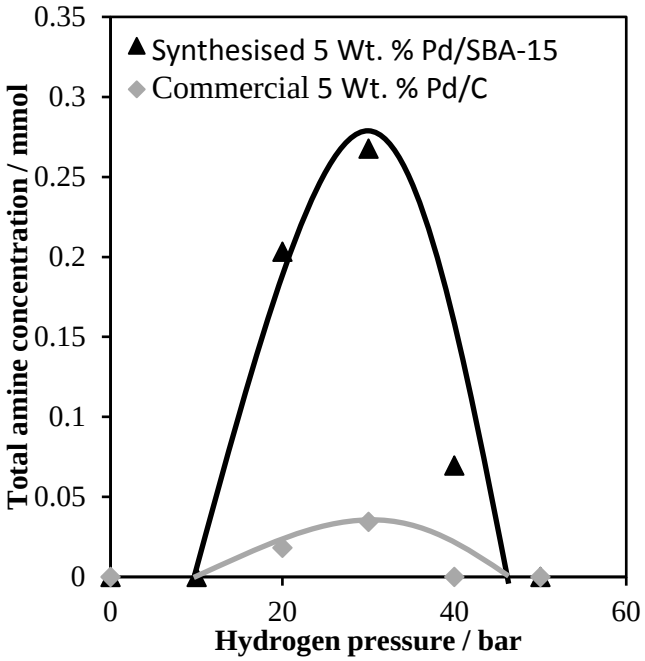

Figure 3.31 – Comparison of the effect of H_2 pressure upon amine yield for Pd catalysts. Experiments run over 7 hours at 120 °C and 800 rpm with 100 mg of catalyst.

What became immediately apparent was the unexpected volcano-plot curve observed with the catalysts tested in this reaction. Typically, it is expected that graphs dealing with total yield of a product will have either a linear or a plateauing trend. For the formation of amines in this hydrogenation reaction it would be expected to see the 40 and 50 bar H_2 reactions to show a similar or higher yield than that of 30. For there to be such a

drastic decrease in the total amine product concentration (accounting for both secondary and tertiary) suggests that the increased pressure has somehow poisoned the catalyst.

With the only variable within the reaction being hydrogen pressure, then whatever effect was causing the inactivity or poisoning of the palladium catalyst must be due to the presence of hydrogen. With no literature precedence for mono-atomic hydrogen causing any kind of poisoning within a hydrogenation reaction, interest turned towards more irregular or less well understood processes which could explain this trend. With this in mind, research was done into the characteristics of palladium hydride (Pd-H), a poorly documented phase of palladium in which hydrogen atoms insert themselves within the crystal structure of palladium itself, affecting both its physical and electronic structure.

With x-ray absorption spectroscopy being the only technique by which the subtle signs of this metal-hydride structure can be detected, time was acquired at the Diamond Light source, utilising the high energy X-rays generated by the synchrotron there.

3.2.6 The effect of hydride formation – XAS

With confirmation of the unanticipated 'volcano plot' interplay between pressure and yield of amine in the hydrogenation reaction, it was clear that further research into the cause was needed. Although the literature in this field is scarce, it is known that under suitable conditions palladium nanoparticles may undergo a structural transformation in the presence of hydrogen.[11,12] Rather than the standard adsorption of hydrogen species upon the surface such as in the Langmuir-Hinshelwood mechanism, the hydrogen may instead merge with the bulk structure of the palladium to form what is referred to as a palladium-hydride (Pd-H). The typical crystal structure of palladium metal (Pd^0) is that of the face-centred cubic (FCC) model, as shown in **Figure 3.32**.[13] A unit cell contains four total atoms within its structure, with eight 1/8 from the corners and six 1/2 from the sides.

Figure 3.32 – Face Centred Cubic (FCC) structure of palladium metal[13]

Under appropriate conditions, and the presence of hydrogen, the structure of palladium metal can be altered to incorporate hydrogen atoms within the interstitial octahedral sites of the FCC structure. In this manner, it forms what can be referred to as an alloy of palladium and hydrogen, with the hydrogen binding between the palladium atoms as shown in **Figure 3.33**.

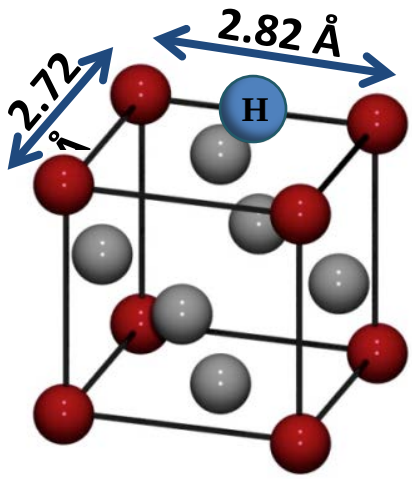

Figure 3.33 – Modified representation of the palladium-hydride (Pd-H) crystal structure[14]

As with any structural augmentation, the modification of its constituent parts will result in several detectable changes within the material, as is highlighted in **Figure 3.33**. The first, and clearest, example is in the increase of inter-atomic distance for the newly formed alloy. Pure palladium metal demonstrates a 2.72 Å distance between the nuclei of two adjacent Pd atoms. However, this distance increases by an average of 0.1 Å to 2.82 Å when accommodating for the newly inserted hydrogen atom.[12] Although a change in inter-atomic distance this small is usually undetectable, it is possible to determine if this has indeed occurred through the processing of X-Ray Absorption Spectroscopy. It is at this point that we must consider that Pd-H in fact exists within two specified phases, that of α Pd-H and β Pd-H (Sometimes referred to as α' Pd-H) as shown in **Figure 3.34**.[11] Rather than a conventional phase, these two are determined by the ratio of palladium to hydrogen.

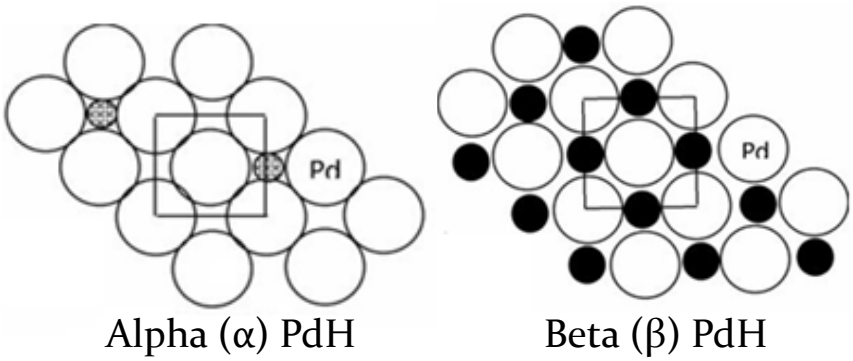

Figure 3.34 – Visual representation of the two 'phases' of palladium-hydride (Pd-H)[11]

When the Pd:H ratio is less than 0.017 then it is said to be of the pure alpha phase. Conversely, a higher ratio than 0.58 indicates it is a purely beta phase. Between these two values a material is referred to as mixed phase. In short, these phases denote the how packed the palladium metal is with hydrogen, with α phase being scarcely populated and β being highly populated. Most notable from this information is that when determining the inter-atomic distance *via* XAS, we can thus establish which hydride phase we are observing. Due to the nature of the technique, as detailed in the sections to follow, the inter-atomic distance is taken as a bulk average. Because of the variability of hydrogen presence in the sample at different phases, this will present itself as a shifting scale. This means that a small increase in detectable distance would correlate with the presence of an alpha phase hydride, whilst a larger increase (to the literature determined value of +0.1 Å) indicates the presence of a beta phase hydride.

The second change within the palladium material upon incorporation of hydrogen to its structure is that of an electronic effect. The excitation energy of a core 1s orbital electron from palladium, referred to as its K edge, is 24,365 eV (24.365 keV).[15] However, in the literature it is noted that in controlled environments, the excitation energy of a core-shell palladium electron within Pd-H structure decreases by a calculated 6.7 eV as indicated within literature (**Figure 3.35)**.[12] It is also referenced that this energy shift discrepancy is diminished for partial hydride formation, and thus the presence of alpha or beta hydride could theoretically be distinguished from the K-edge excitation energy. This, coupled with the aforementioned change in Pd-Pd inter-atomic distance, results in a two-fold method of hydride detection when working with the XAS technique.

There is little in the way of concrete literature to generate a phase diagram for the formation of Pd-H in a supported nanoparticle system, but there have been attempts in other areas to create one, as shown in **Figure 3.36**.[16] As indicated, it is clear that the temperature and pressure of a reaction will affect the formation of palladium-hydride. This further reinforces the suggestion that the sudden loss of amine yield during the increase in hydrogen pressure between 30-40 bar correlates to the formation or phase-change of the hydride. To that end, beam-time was applied for and successfully gained at the Diamond Light Source, at the Harwell Science and Innovation Campus in Oxfordshire. In the sections to follow, I detail the principles behind X-ray Absorption Spectroscopy (XAS), the procedure and technology utilised on site, and the results obtained therein.

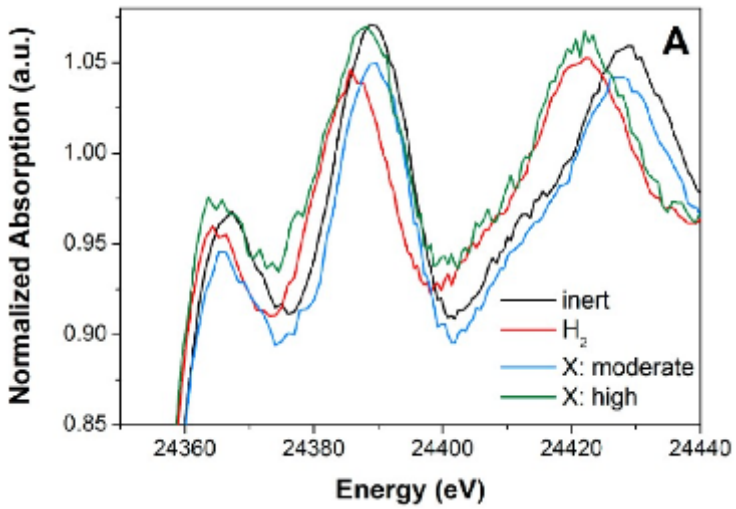

Figure 3.35 – Graph demonstrating the change in core electron excitation energy of palladium upon transition to a palladium-hydride structure. Indicating an inert atmosphere (black), hydrogen atmosphere (red) and moderate/high propyne reaction rate (blue/green).[12]

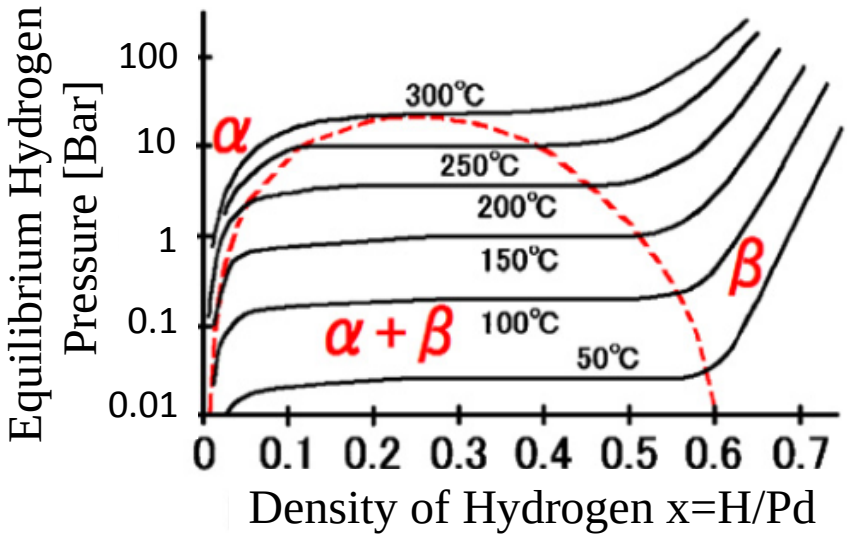

Figure 3.36 – Proposed phase diagram for the delineation of the alpha, beta, and mixed phases of palladium-hydride (Pd-H). Diagram indicates a dependence upon both hydrogen pressure and temperature for hydride formation.[16]

3.2.6.1 XAS – The Principle

X-ray Absorption spectroscopy (XAS) is a bulk analysis technique, used to determine the properties of materials such as electronic structure and geometric properties. More specifically for this work, it can be used to determine the inter-atomic distance within a material, along with the excitation energy of the elements within (which can also indicate aspects such as oxidation state).

XAS can accomplish this by utilising the unique 'fingerprint' nature of core electron excitation in atoms. Using pre-calculated values for the energy needed to excite electrons from an elements K, L or M orbitals, and observing the step-edge detected, the electronic state can be ascertained. Following from this, the subsequent energy oscillations can be used to determine inter-atomic distances.

To begin, this particular technique is viable only if x-rays of sufficient energy can be generated, and finely tuned before being applied to the experiment. To this end, the most viable source is *via* a synchrotron radiation site such as the Diamond Light Source. Often associated with their sibling technology, particle-colliders like the Large Hadron Collider (LHC), synchrotrons rely on the acceleration of particles to relativistic speeds. By generating a beam of electrons and accelerating them to a maximum of roughly 3 GeV (3 billion electron volts) and forcing them to travel in a curved path through the use of high powered electromagnets, they will release synchrotron radiation.[17]

This electromagnetic radiation can then be passed through various devices designed to filter and focus the desired wavelengths of light (**Figure 3.37**). In this way a synchrotron facility may accommodate for many different kinds of experiment, depending on the type and energy of electromagnetic radiation desired. Specifically in the interests of this work, the B18 line was utilised, as its particular focus (a high flux versatile multi-pole wiggler) generates a tuneable X-ray source of 4-35 keV. This allows for the K-edge excitation energy of palladium to fall well within the range of the apparatus.

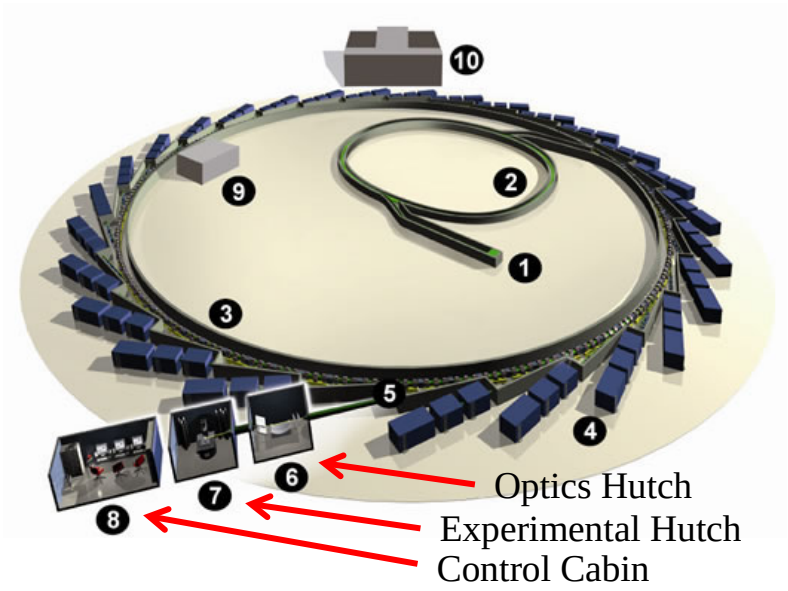

Figure 3.37 – Annotated design schematic for the Diamond Light Source synchrotron.[17]

The design of the experimental hutch allows for the experimental cell you are using to be aligned between the exit-point of the light source and the detection unit that is positioned directly across from it. The principle of XAS is that by knowing the energy of the x-rays that have passed through your reaction (and steadily increasing it), you can generate data which highlights the point at which excitation energy is achieved, producing a photoelectron, through the sudden energy discrepancy between incident and transmitted x-rays, as highlighted in **Figure 3.38**.

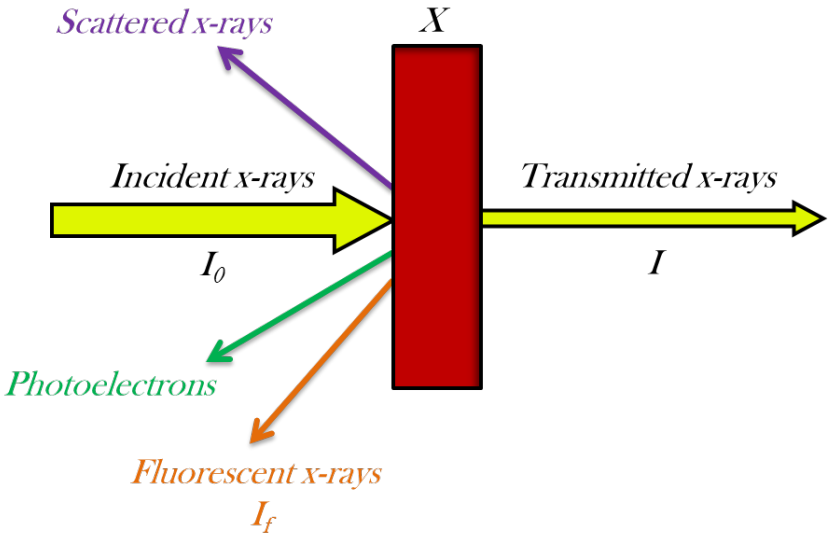

Figure 3.38 – Graphic representation of X-rays interactions upon an experimental sample.

As the energy of the incident x-rays introduced to the experiment gradually increases, the spectrometer will detect the transmitted x-rays and generate a graph with the energy level of the incident rays as the x-axis, and the discrepancy between that and the

transmitted rays (absorption coefficient - I/I_0), as the y-axis. At the point of electron excitation there is a sudden change in the coefficient, known as a step-edge or rising-edge. Data generated typically appears as in **Figure 3.39**.

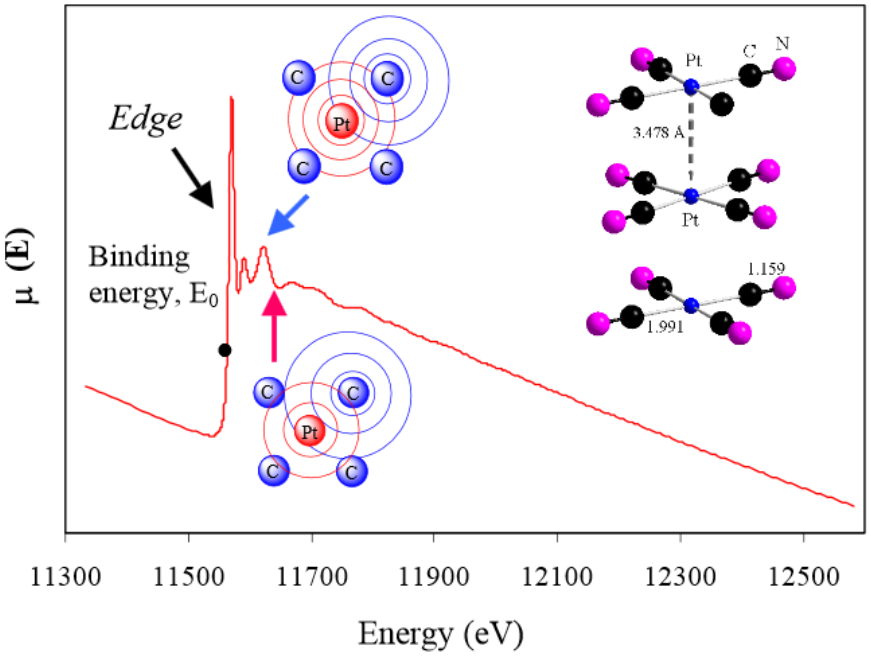

Figure 3.39 – Annotated representation of a typical X-ray absorption spectrum.

A typical XAS spectrum can be delineated into distinct regions in regard to the rising-edge (E). First is the x-ray absorption near-edge structure (XANES), also known as near edge x-ray absorption fine structure (NEXAFS), which incorporates the region prior to the step-edge ($E < E_0$), aptly named the pre-edge, and the rising-edge and immediate structure that and follows (10-150 eV > E_0). Following from this is the extended x-ray absorption fine structure (EXAFS) which deals with the long range structure of the spectra (50-1000 eV > E_0). With the XANES region, it is possible to determine both the element's oxidation state, but also any shifts in energy that may be observed, such as in the formation of Pd-H. Beyond this, the behaviour of the spectra becomes more complicated.

As demonstrated in **Figure 3.39**, following the immediate step-edge we see a series of oscillations. This region is known as the "Kronig Structure" named after its discoverer.[18] These fall within the EXAFS region and can be used to determine the local structure of the material being analysed, including the elemental identity of neighbouring atoms, as well as the inter-atomic distance. To understand the origin of these oscillations, and how this data can be derived from them, we must look to quantum mechanics.

When the excitation energy of the core electron is achieved, and it is ejected as a photoelectron, we can treat this ejection as the propagation of a wave. Subsequently, we can treat the atoms surrounding the centrally excited atom as scatter points, in much the same way as blockades on a beach. As the electron wave interacts with these scatterers, backscattered waves will be generated, which will in turn begin to interact with the originally propagating waves. In this manner, they will experience constructive and de-constructive interference such as with any interacting waves. This pattern results in a modulation of the absorption coefficient that is observed with the XAS, and is the origin of the oscillations we can see.

The structure of the oscillations can be analysed to determine the amplitude and phase of the backscattered photoelectron wave. These are influenced by the element acting as the scatter point, and its distance from the source atom. To put it another way, by working backwards from the modulation of the absorption coefficient, we can calculate the fingerprint pattern of constructive and de-constructive interference of the wave. From this unique pattern we can determine both how far away the backscattered waves propagated from, and from what scatter point (which element) they were formed. From this we can calculate the percentage metal (Pd-Pd) and oxide (Pd-O), as well as the aforementioned stretching of the Pd-Pd atomic distance from 2.72 Å to 2.82 Å.

3.2.6.2 XAS - experimental

In order to adequately observe the pressure-based interactions of the nitrile hydrogenation reaction, it was necessary to construct a custom-made reaction cell. Taking the schematics of one of our standard Parr autoclave systems, we requested a modified unit which contained pressure-sealed portals so that the x-rays could successfully penetrate into the reaction medium and travel outwards into the XAS detector (**Figure 3.40**). A third view port, placed at a 90° angle, was installed with the intention of enabling *in-situ* infra-red (IR) techniques. Initially the device was designed with pressure resistant silica windows, however some short calculations suggested that these would absorb >99.9% of the x-ray energy before reaching the detector. As such some custom ordered vitreous (glassy) carbon windows were requested and installed in the laboratory. Vitreous carbon, although opaque to visible light and therefore black in appearance, are readily permeable by x-ray radiation. This, coupled with the standard pressurising system as described in previous sections in regards to autoclave work, were brought on-site to the Diamond Light Source.

Figure 3.40 – Schematic of the custom windowed autoclave and components

Due to the unique nature of this procedure, some modifications to the standard reaction protocol were needed. First was the need for a perturbation test within the cell. The reaction had to be mixed enough by the impeller to suitably mix the reagent and the hydrogen gas, whilst ensuring that no gas bubbles or vortices disturbed the line of sight through the windows and reaction matrix. Because both the impeller speed and the reaction temperature (which affects the liquid viscosity) can lead to the formation of a vortex or bubbling, a short series of tests were performed prior to the beam-time. Experimenting at ambient temperature and pressure 800 rpm was noted as the upper limit before perturbation occurred. At ambient pressure but higher temperature, it was confirmed that the chosen temperature of 120° C affected no further changes, but at higher pressures it was noted that at 800 rpm there occurred some slight bubbling through the windows. As such it was determined that the impeller speed should not exceed 800 rpm, and should in fact be limited to around 650-700 rpm to ensure that perturbation would not negatively affect the quality of data received.

Once on-site, several reactions were performed over the course of the 4 day beam-time. Firstly, several ex-situ samples were generated in washers, so that the catalyst use for the subsequent experiments during the beam-time could be analysed on their own, outside of the reaction matrix. Following this, due to the size of the *in-situ* cell, and because we needed to achieve the highest signal possible to better distinguish the minuscule step-

changes associated with hydride formation, the reaction was scaled up. Using 750 mg of the 5 wt. % Pd/SBA-15 and 50 ml of solution, one reagent-deficient reaction was performed with only 50 ml of the solvent methanol. This was to observe the actions of the catalyst without the additional interaction of the reacting species. Heated to 120° C and stirred at 650 rpm, clusters of scans were performed as hydrogen was introduced at 2, 10, 20, 30 and 40 bar, along with scans run after cooling and purging under nitrogen. Following this, a reaction with 24 ml methanol and 26 ml crotononitrile (319 mmol) was performed with 750 mg of the catalyst, and with the same pattern of incremental hydrogen pressure ramping. The following sections are a recounting of the experiments run, and the results obtained from them.

3.2.6.3 XAS – Results

3.2.6.3.1 Solvent Only

A control experiment was first conducted to establish catalyst behaviour in the absence of the crotononitrile reagent. In this way, we could eliminate the experimentally confusing variable of a reaction undergoing upon the surface, possibly affecting any detectable formation or consumption of the Pd-H species. As mentioned in the previous section, the first salient piece of data generated with XAS is the comparison of incident energy and the absorption coefficient observed. Typically, multiple scans will be run each lasting several minutes. In this manner, several scans can be taken and normalised together, as shown in **Figure 3.41**. By taking multiple scans and normalising them, we can smooth out the rough edges that would be apparent with of the absorption spectra of only one scan. This is the method by which the subsequent data was processed.

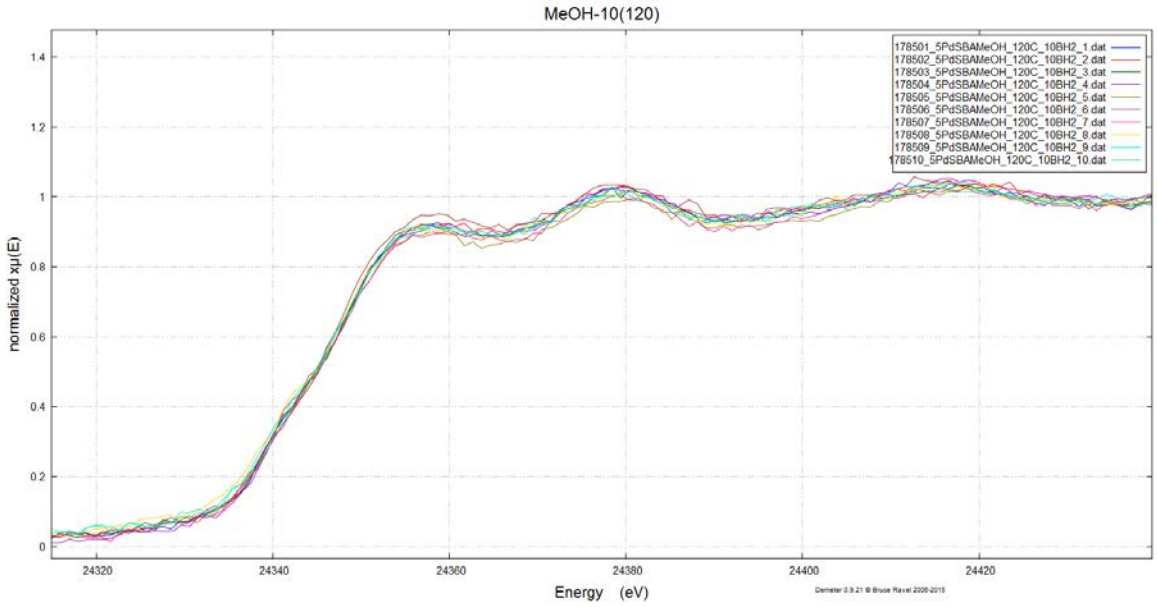

Figure 3.41 – Snapshot example of the multiple XAS scans plotted in Athena, in this case the 10 scans run at 10 bar hydrogen with the 5 wt. % Pd/SBA-15 and within the solvent-only system. This data is then normalised to create a smoothed plot for each scan cluster.

This refined data can then be compared against database samples of known materials to determine the studied samples composition. In the case of this work, reference samples of palladium metal and palladium oxide were used. These are generated by running XAS on sheets of the pure constituent (*ie*. pure Pd, or pure PdO). These can then be applied using a computer algorithm to calculate the percentile value of each phase within the sample. As a result a fitted x-ray absorption near-edge structure (XANES) plot can be produced, which

combines the obtained XAS scan, the shape of the reference material scans, the 'fitted' line shape which combines the reference material scans together. Finally the 'residual' line is added, which is a visual representation of any discrepancies between the true scan plot and the fitted plot, and thus can be used to identify if any potential species have been unaccounted for. In summation, the result is a plot as detailed in **Figure 3.42**.

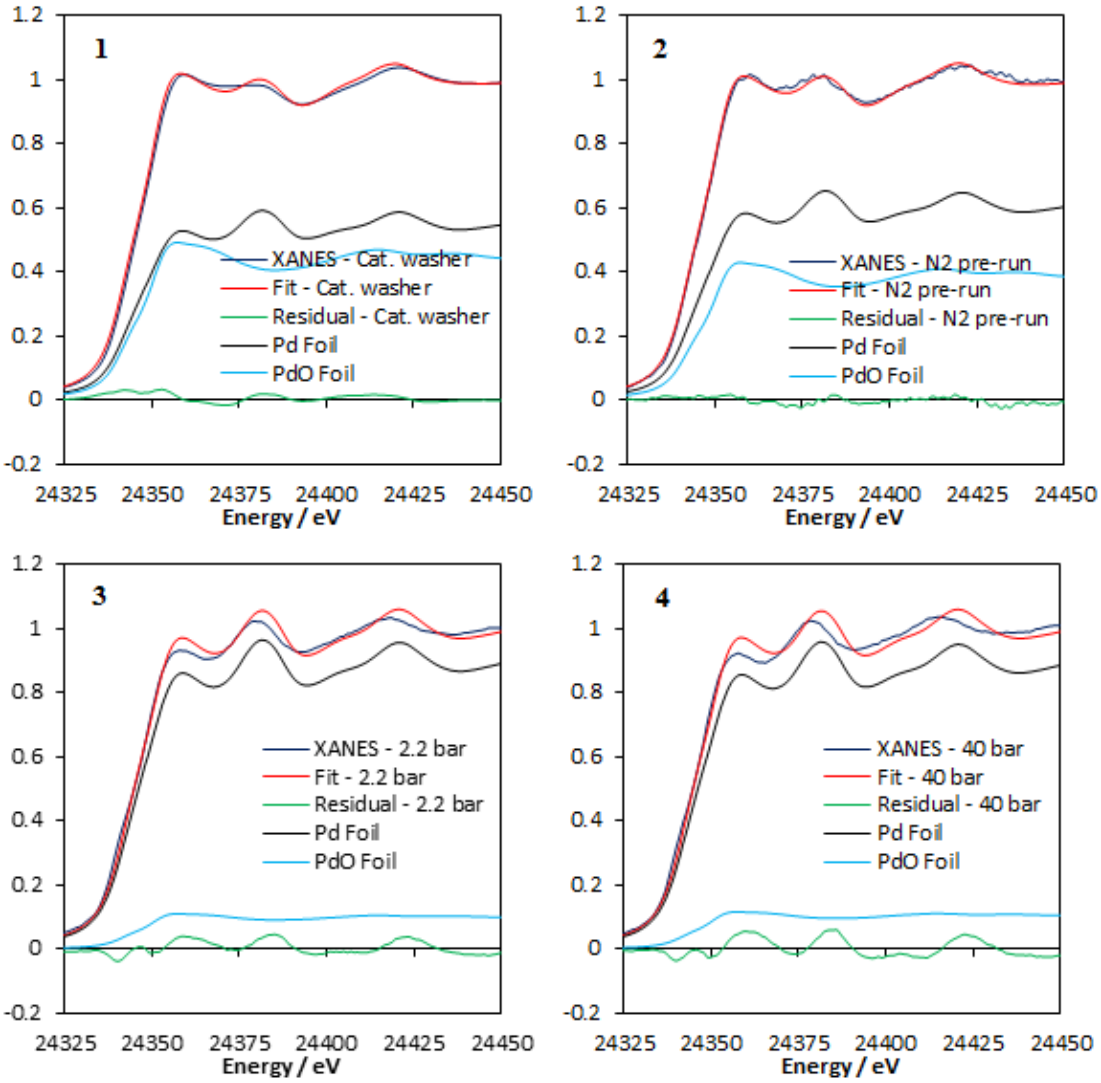

Figure 3.42 – Fitted XANES plots for catalyst powder (**1**), reaction mixture under nitrogen (**2**), reaction mixture under 2.2 bar H_2 (**3**), and reaction mixture under 40 bar H_2 (**4**).

Several pieces of information can be discerned from these initial fitted XANES plots. The catalyst powder washer indicates a PdO content of around 40%, with a slight decrease whilst within the methanol solvent, likely due to its innate reductive properties. Upon introduction of the hydrogen gas at 2.2 Bar we see a significant loss of PdO within the material, which is to be expected as the hydrogen will reduce it back to its pure metal form. This reduction is not much changed between 10 and 40 Bar H_2, and the comparative percentage of composition is demonstrated in **Figure 3.43**.

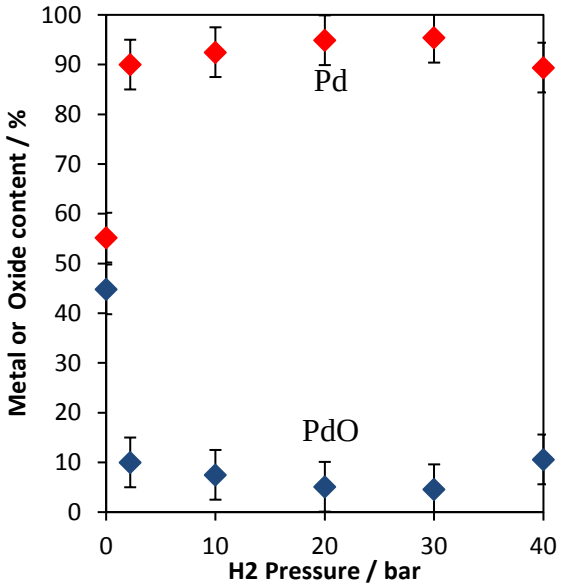

Figure 3.43 – Comparison of the metal/oxide composition percentage of the catalyst prior to the reaction, and at varying hydrogen pressures within the solvent-only system. Data indicates an instant conversion of any present oxide with little variation thereafter.

When looking at these results it is clear that there is an unaccounted variable With hydrogen gas in the system the oxide content should become negligible, and coupled with this we can see that for the 2.2 bar hydrogen scans, and most prominently for the 40 bar scans, the 'fit' does not align properly with the physical data.

Whilst this may be discounted through basic error, this may be the first indication that we are observing the formation of a palladium-hydride (Pd-H). Because the program takes reference samples as its input, if there is an additional material that is unaccounted for, discrepancies will arise in the data. If it were possible to isolate a Pd-H material and apply its reference plot, we would likely generate a much better fit, and have a more negligible PdO content after introducing hydrogen.

The next step that can be taken with the generated data is to focus on the step-edge and oscillations of the scans taken at each pressure range. When overlaid, it becomes apparent that there are subtle shifts in the electron excitation energy of the Pd in the catalyst. These changes correlate to a gentle down-shift in the excitation energy as the hydrogen pressure of the system increases, as shown in **Figure 3.44**. With suitable magnification this shift is apparent to the naked eye, but it can also be quantifiably measured within the processing programs. As such we can generate a plot as shown in **Figure 3.45**, which details the trend of energy down-shift as a function of pressure.

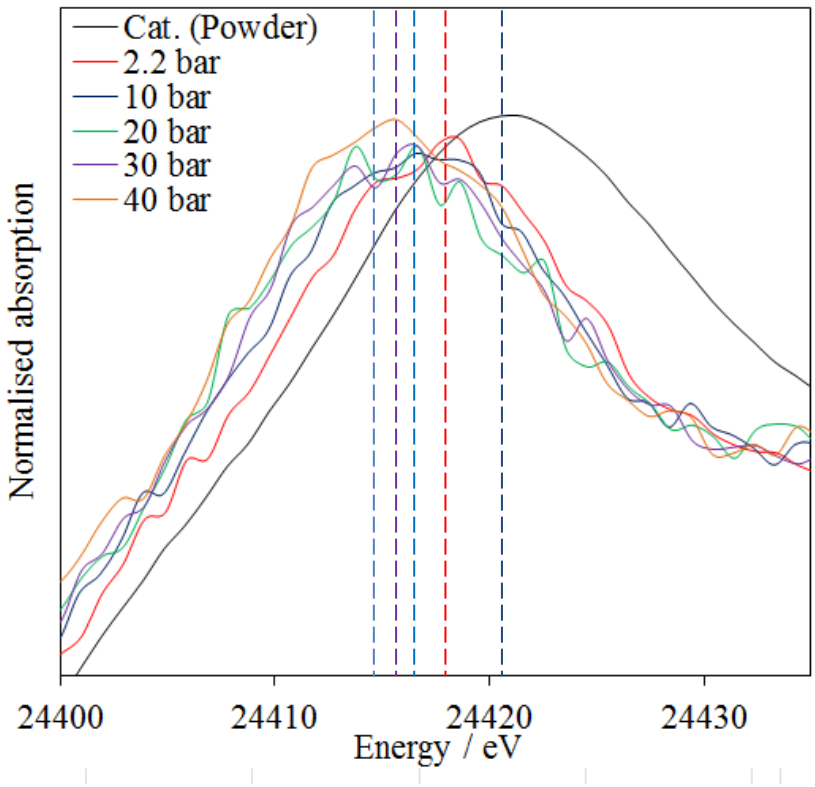

Figure 3.44 – Comparison of the generated XAS spectra at increasing hydrogen pressure, for the experimental set within the solvent-only system. Data highlights the subtle down-shift in electron excitation energy maxima as the pressure increases, as indicated by dashed lines.

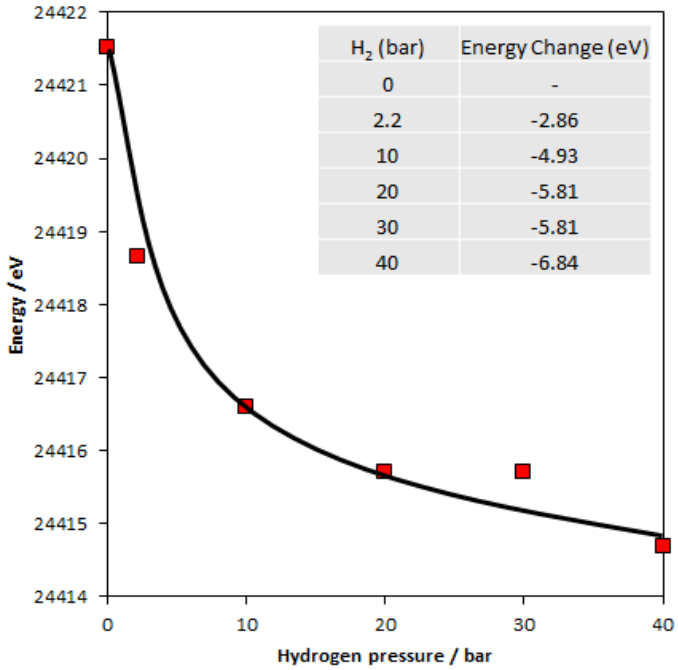

Figure 3.45 – Generated plot of the relative shift in the first absorption maxima energy as a function of pressure, showing a clear downward trend as hydrogen pressure is increased

As highlighted in **Figure 3.45**, upon introduction of hydrogen to the reaction we can see a sharp initial shift of -2.86 eV followed by a steady down-shift as the pressure increases, to a maximum of -6.84 eV. As mentioned previously, a negative shift in excitation energy is a significant indicator for the presence of Pd-H within the material. Furthermore, the shift of 6.84 eV closely matches that documented in the literature, with a quoted shift of 6.7 eV.[12] With this evidence we gain our first suggestive proof for the successful formation and *in-situ* detection of a palladium-hydride species.

To further justify these results we then looked to the change in Pd- interatomic scattering distance. As explained in previous segments, the insertion of a hydrogen atom between the palladium atoms forces a subtle shift in the Pd-Pd distance. By observing the oscillations of the x-ray absorption spectra, we can generate a radial distribution function (RDF) plot, which highlights any changes in the distance as the hydrogen pressure increases, as shown in **Figure 3.46**. As with the previous plots for excitation energy shift, we can clearly see by sight alone a subtle increase in the Pd-Pd interatomic distance. This fits in accordance with the literature that suggests a shift of approximately 0.1 Å for hydride formation.

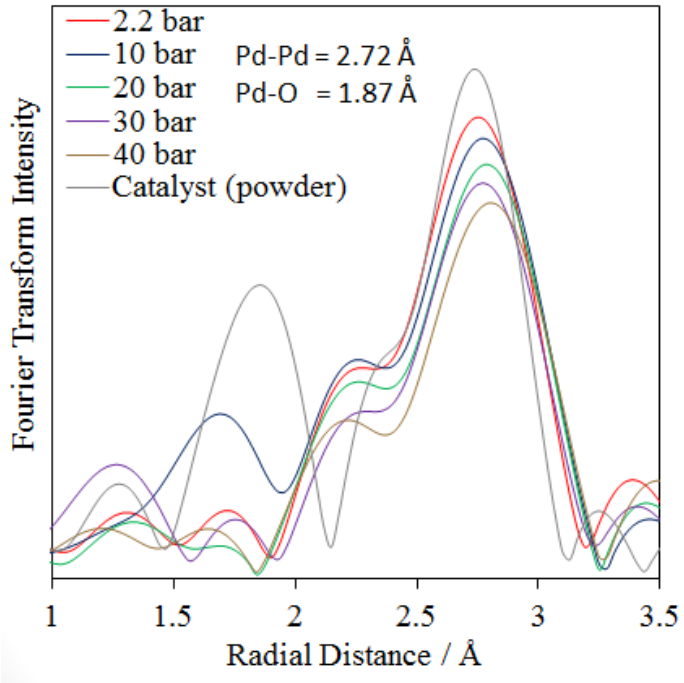

Figure 3.46 – Overlaid plot of the generated RDF plots within the solvent-only system for each hydrogen pressure, indicating a subtle increase in interatomic distance.

As with the excitation energy data, we can accurately calculate the maxima of the peaks, and compare these as a function of hydrogen pressure. This can then be plotted to generate a graph as shown in **Figure 3.47**, and extrapolated to calculate the lattice constant, as shown in **Table 3.7**.

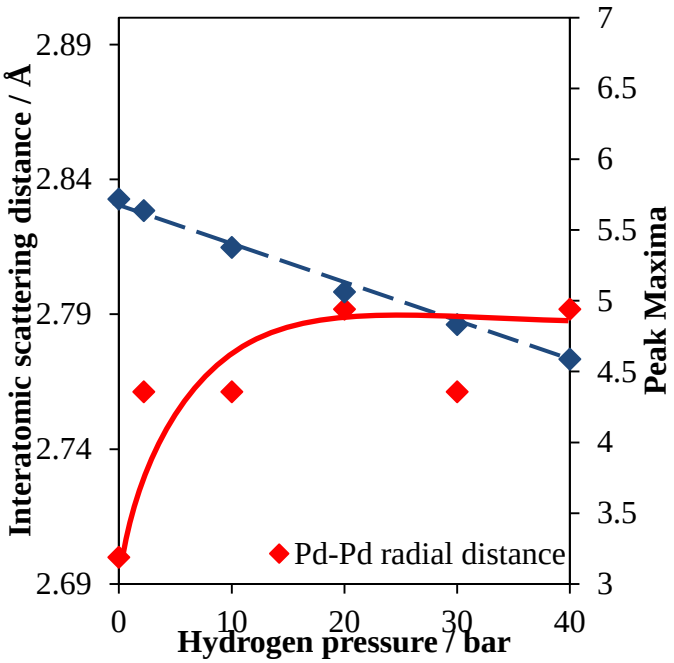

Figure 3.47 – Plotted data of the peak maxima and magnitude for Pd-Pd interatomic scattering distance against hydrogen pressure, indicating a clear increase in distance as pressure increases

Pressure / bar	Radial distance / Å	Atomic radius / Å	Lattice constant / Å
0	**2.70**	**1.35**	**3.82**
2.2	**2.76**	**1.38**	**3.91**
10	**2.76**	**1.38**	**3.91**
20	**2.79**	**1.40**	**3.95**
30	**2.76**	**1.38**	**3.91**
40	**2.79**	**1.40**	**3.95**

Table 3.7 – Calculated Pd-Pd interatomic scattering distance at varying pressures, and the lattice constant of the crystal structure as extrapolated from these values

As highlighted, there is a clear and empirical change in the Pd-Pd radial distance as the hydrogen pressure of the reaction is increased. With a maximum alteration of 0.092 Å, this is also in close agreement with the literature quoted value of 0.1 Å. As a result, there are now two separate sources of data that enforce the suggestion that a hydride species is forming upon introduction of hydrogen. Notably, it seems that the formation is gradual, with what we would quote from literature as substantial Pd-H content arising at 40 bar H_2.

One final piece of reinforcing data can be found in the magnitude of the radial distance peaks. Within the experimental data, the height of the peak correlates to the coordination number of the atom in question. What we see in our experimental set is a steady decrease in peak magnitude over pressure. Importantly, the XAS technique is unable to detect coordinated hydrogen atoms, as they cannot effectively be interacted with. Therefore, the steady decrease in magnitude, and thus coordination number, can in fact be attributed to the steady 'replacement' of palladium neighbours with hydrogen atoms.

With several coinciding pieces of data pointing towards successful *in-situ* hydride formation within the pressure cell, it was then time to run the same experiment, but with the standard reagent, crotononitrile, included in the reaction matrix.

3.2.6.3.2 Solvent & Crotononitrile Experiment

As with the previous solvent-only experiment, the reaction was run at steadily increasing hydrogen pressure steps, ranging from the baseline of 2.2 bar, through 10, 20, 30 and finally 40 bar H_2. At 40 bar, due to the high excess of reactant, it was possible to re-pressurise the system and allow for multiple scans at this particular range. The raw data obtained was again compiled into fitted XANES and ChiR plots, and subsequently scrutinised to elucidate data on the potential shifts in excitation energy and Pd- interatomic scattering distance.

With the plotted XANES data as shown in **Figure 3.48**, it became clear that a similar effect was being observed as with the solvent-only system. The initial scans show a good agreement between the physical data and the fitted plot. With the 2-30 bar scans there was the notable shift from mixed metal/oxide content to almost pure metal, and at the 40 bar point there was a clear discrepancy between the data and the fitted plot, suggesting a third species at play. Interestingly, upon cooling and purging of the system under nitrogen gas, the comparison between the two plots becomes much less divergent. This in itself may suggest that the act of purging may be reversing any effects seen, if not completely.

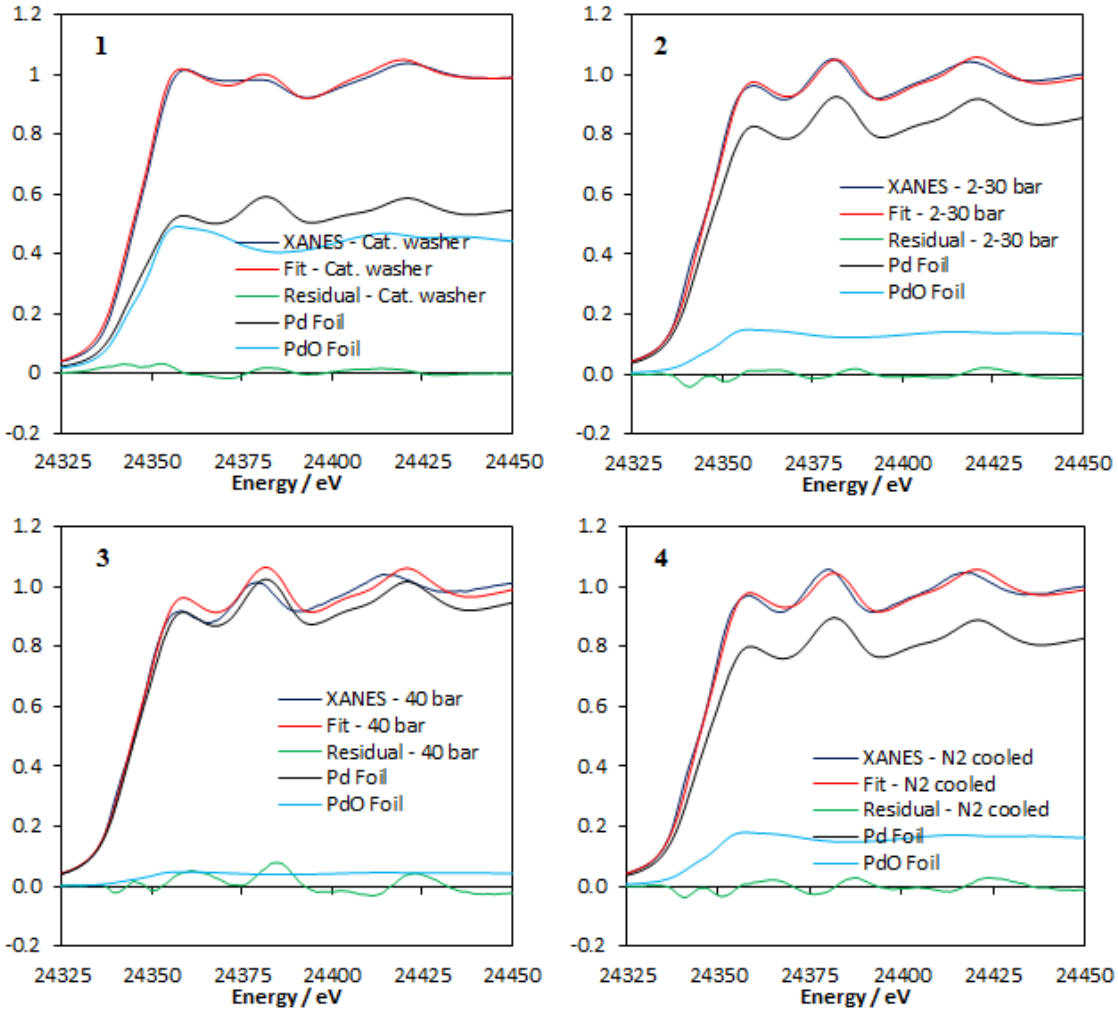

Figure 3.48 – Fitted XANES plots for catalyst powder (**1**), merged scans for 2.2 - 30 bar H_2 (**2**), reaction mixture under 40 bar H_2 (**3**), and the cooled reaction mixture under N_2 (**4**). (24 ml methanol and 26 ml CrCN) [319 mmol], 650 rpm, 750 mg 5 Wt.% Pd/SBA-15)

Taking the data generated by the program on the ratio between the oxide and metal present within the combined scans, we obtain the results shown in **Figure 3.49**. As expected, the oxide content is immediately diminished upon introduction of hydrogen into the matrix, causing near instantaneous reduction of the oxide to the pure metal form. As with the solvent-only system, the program suggests there is still a small amount of oxide present, which would be almost impossible in a hydrogen infused environment. This further reinforces the concept that a third palladium species, Pd-H, is present, causing the programs results to become skewed due to the lack of data on the third agent.

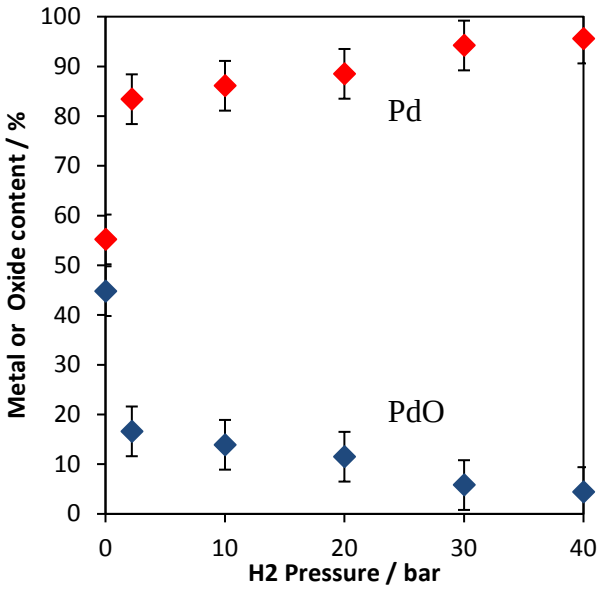

Figure 3.49 – Comparison of the metal/oxide composition percentage of the catalyst prior to the reaction, and at varying hydrogen pressures after at least 10 scans

With the oxidation state data acquired, focus shifted to the relative shifts of the XANES oscillations, in an attempt to discern if a similar effect to that of the solvent-only reaction could be observed, or if the presence of the reagent would affect it in any way. Once magnified and overlaid, including the fresh palladium powder scan (referred to as Catalyst 'washer'), it became immediately clear that the same trend of gradually decreasing excitation energy was not present for this reaction, as shown in **Figure 3.50**. Rather than the gradual shift, it was apparent that there was the initial shift upon the introduction of hydrogen to the reaction, followed by absolutely no change between 2 and 30 bar.

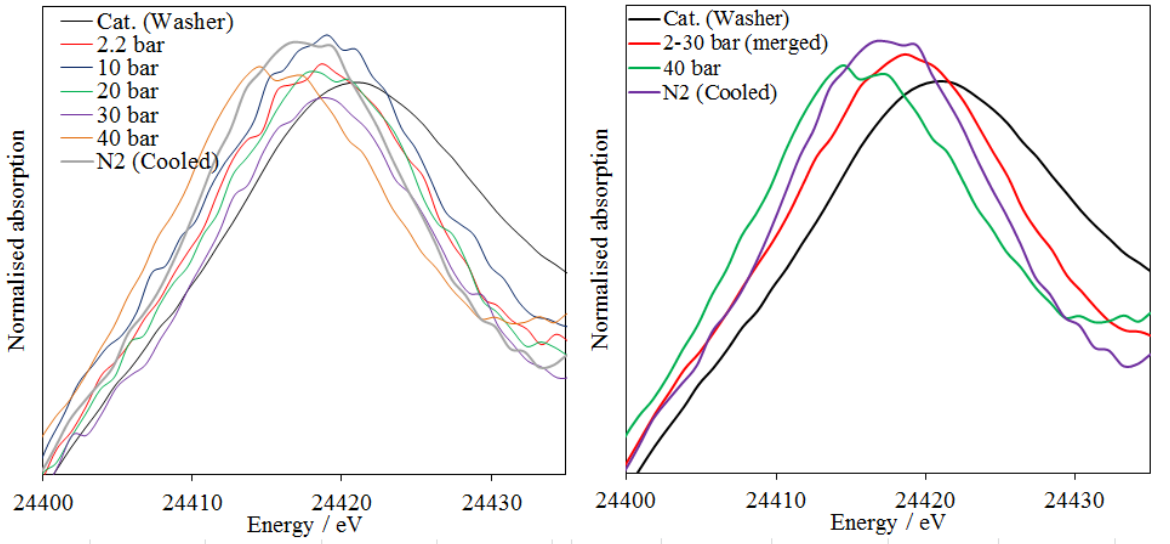

Figure 3.50 – Raw magnified XANES region (**left**) and the version with 2.2-30 bar condensed due to their identical patterns (**right**), highlighting the altered excitation energy

Once the scans from 40 bar H_2 were overlaid however, it was noted that it underwent a significant shift in energy compared to the previous pressures. Finally, upon cooling and purging under nitrogen, the data suggested that the change in excitation energy was actually reversed, showing a partial restoration to any effects within the palladium structure. The maxima of the merged scans were plotted and presented in **Figure 3.51**.

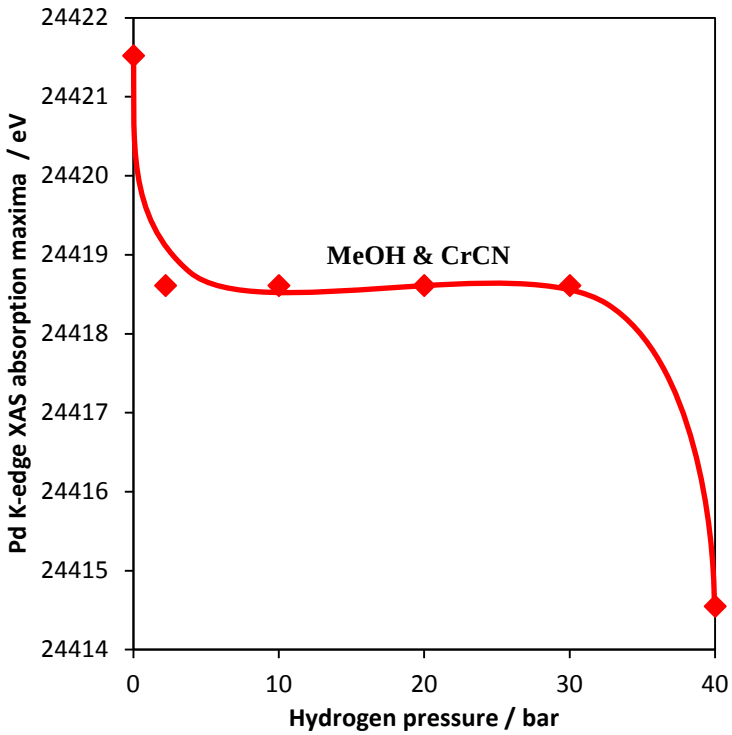

Figure 3.51 - Relative shift in the first absorption peak maxima as a function of pressure, showing a clear overall drop, with a distinct plateau between 2.2-30 bar H_2. (5 wt. % Pd/SBA-15, 120° C, 650 rpm, 319 mmol CrCN in MeOH)

This stalling plateau in the shift of excitation energy was perplexing. As determined prior to this, the decrease in energy is associated with the formation of Pd-H. For this dwell to occur, the assumption must be that the crotononitrile is preventing the formation of a palladium hydride species. That is, until a pressure of 40 bar H_2 is achieved. At this point the hydride retardation seems to revert, and we observe a full shift of -6.97 eV, almost identical to that observed in the solvent-only reaction.

In an effort to confirm this hypothesis of hydride retardation, the RDF interatomic scattering distance data from the XANES oscillations were evaluated. Upon plotting this data (**Figure 3.52**) and taking the peak maxima as a function of pressure (**Figure 3.53**) it quickly became clear that this effect was not an artefact of the excitation energy data alone.

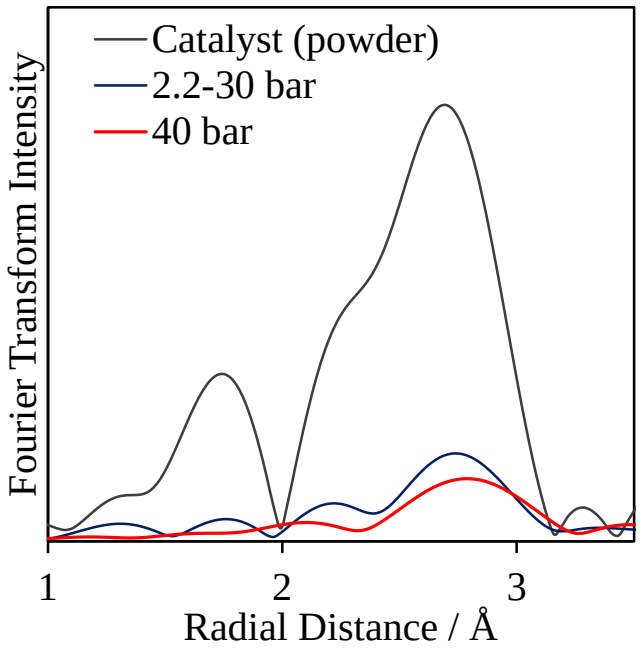

Figure 3.52 – Overlaid graph of the generated RDF plots for the merged scans run at varying hydrogen pressures. Indicates a subtle increase in interatomic distance

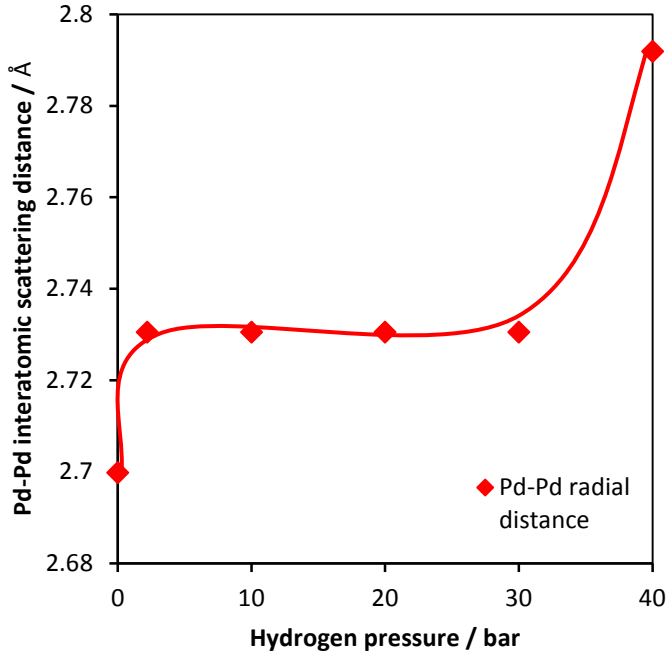

Figure 3.53 - Plotted data of the peak maxima magnitude for Pd-Pd interatomic scattering distance against hydrogen pressure, indicating a clear overall increase in distance as H_2 pressure increases (5 wt. % Pd/SBA-15, 120° C, 650 rpm, 319 mmol CrCN in MeOH).

It is clear from the plot that we can observe the exact same trend with the alteration for Pd-Pd interatomic distance, as we can for the core electron excitation energy. With an initial change upon introduction of hydrogen, followed by a dwelling plateau with no effect between 2 and 30 bar, and finally a significant shift at 40 bar H_2 to bring the total interatomic scattering distance change to 0.092 Å, the same as with the solvent-only system. It was then clear that the two experiments needed to be overlaid and compared, before a hypothesis could be discussed and argued for.

3.2.6.4 XAS - Conclusions

As it was clearly apparent that there were distinct differences between the two experiments, a comparison of the two in regards to excitation energy and interatomic scattering distance generated from the merged scans of each pressure were plotted (**Figure 3.54** & **Figure 3.55** respectively).

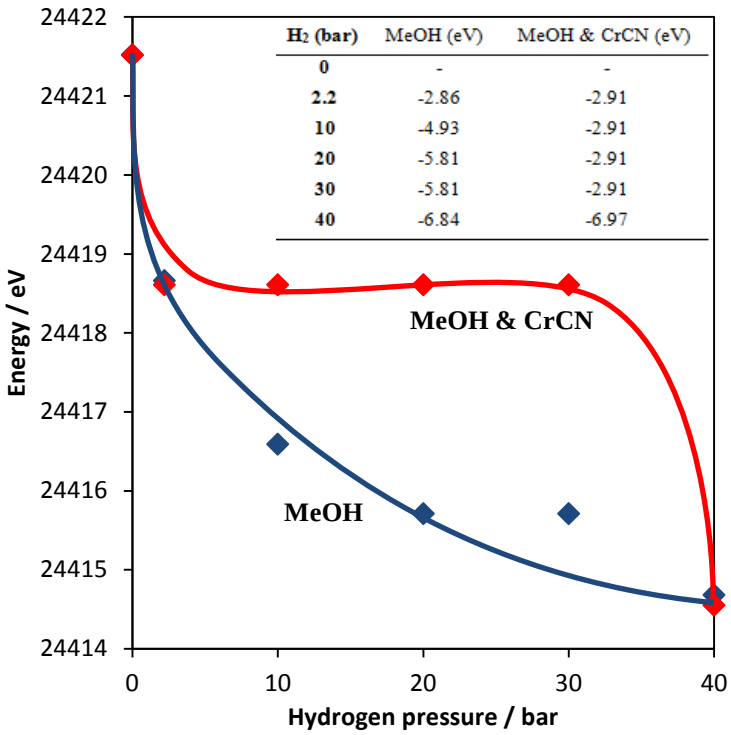

Figure 3.54 – Overlaid plot of both the solvent-only and reagent XAS reactions. (5 wt. % Pd/SBA-15, 120° C, 650 rpm, combination of MeOH only and 319 mmol CrCN in MeOH mixtures)

With **Figure 3.53** we can see a difference between the energy shifts that were initially apparent between the two. As shown here, the initial energy decrease is of a similar level for both experiments at 2 bar. However, at 2-30 bar there is a clear stagnation of change in the scans runs with crotononitrile present. Finally, at the 40 bar scans, we see that the two points re-join and exhibit a similar shift in the electron excitation energy again.

If we consider the literature and what we know of the processes responsible for this change, we can draw the conclusion that although the reagent-present reaction undergoes some small initial formation of hydride, the process is halted until sufficient pressure at 40 bar of H_2 is achieved. As such it can be inferred that crotononitrile itself is responsible for the forced inhibition of the hydride structure. However, once the pressure reaches 40 bar of hydrogen, we see that there is a rapid decent to the -6.9 eV range that we observe without the reagent. As such we can also deduce that whatever preventative measures the crotononitrile has upon Pd-H formation is reversed at appropriate pressure and/or concentration of hydrogen.

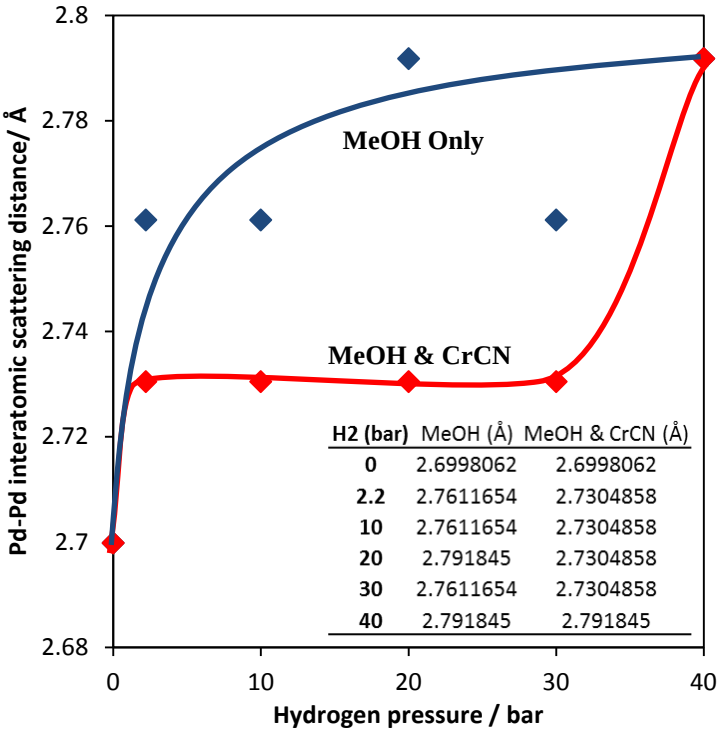

Figure 3.55 – Comparison plot of both XAS experiments for the Pd-Pd interatomic scattering distance shifts observed in both, again indicating a notable retardation in the presence of CrCN. (5 wt. % Pd/SBA-15, 120° C, 650 rpm, combination of MeOH only and 319 mmol CrCN in MeOH mixtures)

By comparing the results found with the energy shift to that of the Pd-Pd interatomic scattering distance as shown in **Figure 3.54** it was hoped that further evidence to support the theory of retardation could be found. What is obvious upon overlaying the data is that the same trend that we observe for the change in excitation energy can be observed here. Upon a small initial increase in Pd-Pd distance, the reagent-present reaction shows a marked dwell in activity up to 30 bar, where we again observe this convergence between the two experiments, to both match with an increase of 0.1 Å.

Again, with reference to previous discussions on the cause of this spatial increase, we can determine that the presence of the crotononitrile reagent is preventing the formation of a saturated Pd-H, a so-called beta hydride. However, once 40 bar H_2 is reached this effect ceases to have any preventative hold on the formation of the hydride material.

The reason for this hydride retardation is, in this author's opinion, due to the nature of the hydrogenation reaction. When only solvent is present, hydrogen may adsorb to the surface uninhibited, and eventually incorporate itself into the palladium crystal structure. However, with the introduction of crotononitrile, the reaction of alkene hydrogenation and to a lesser extent nitrile hydrogenation means that the adsorbed hydrogen is quickly consumed in the process. As a result, only a small percentage will form the Pd-H structure, accounting for the small shift we observe which would correlate to an alpha Pd-H. Up to 30 bar H_2, the reaction rate is so great that the hydrogen can never fully merge with the palladium atoms to form the hydride, instead being consumed in ever greater quantities by the reagent. However, upon reaching 40 bar H_2, it can be surmised that the sheer concentration of hydrogen then surpasses the rate at which the hydrogen atoms can be utilised. As such, a larger percentage of hydrogen atoms may dwell upon the surface long enough to incorporate into the bulk structure as a palladium-hydride. At this point, we observe the creation of a beta Pd-H. This is confirmed both by the full shift in excitation energy, as well as the full enhancement of the Pd-Pd interatomic distance.

In summary of the comparison of results between the solvent-only experiment and the crotononitrile present one, we can draw a persuasive hypothesis on the formation and role of palladium hydride in this reaction. If we recall the volcano-type plot of amine yield as a function of pressure, we can identify that 40 bar illustrates a significant degradation of yield. This 'catalyst poisoning' occurs only at 40 bar H_2 and onwards. If we then observe the trends shown in the XAS data, and the confirmation that significant quantities of

hydride (beta Pd-H) only occurs at 40 bar H_2, we can firmly claim that in the presence of a reacting agent, true formation of Pd-H only occurs at 40 bar.

Therefore, a solid claim can be made towards palladium-hydride acting as a catalytic poison, altering the electronic properties and/or physical properties of the Palladium metal nanoparticle active sites in such a way as to make nitrile hydrogenation highly unfavourable. This results in the trend of amine yield as a function of pressure that was observed in previous work. In essence, the hydrogen itself becomes a poison to the hydrogenation reaction.

It is important to note that the nature of working with X-ray Absorption Spectroscopy involves the evaluation of subtle changes. As such it is important to remain cautious with any findings unless there is sufficient evidence to corroborate. The work discussed in this chapter endeavours to do so, but further work is always beneficial when considering work in this field. As such it would be advisable to further this research to better elucidate the nature of this hydride formation.

3.3 Conclusions

To conclude the findings of this chapter on palladium catalyst-facilitated nitrile hydrogenation we can draw a number of succinct conclusions on the nature of the reaction.

When working at ambient pressure and temperature, it is possible to facilitate the hydrogenation of the C=C alkene bond. The rate of this reaction can easily be modified and increased through the manipulation of temperature, catalyst mass, metal loading, and perturbation (hydrogen access). However, the reaction within this stage is 100% selective towards the alkene hydrogenation and we observe neither the direct formation of any amine, nor any evidence of its presence at any point.

Upon increasing the pressure of the reaction, we see an expected increase in C=C hydrogenation yet still no evidence of amine formation until an increase in temperature is also facilitated. Upon a combination of temperatures exceeding 100° C secondary and tertiary amine formation was observed with increasing yields as temperature and pressure were increased, with an ideal yield observed at 120° C and 30 bar H_2. The lack of primary amine within chromatograph data supports the previously discussed volatility of this product when coupled with the imine intermediate.

However, introduction of pressures exceeding this value, from 40 bar and above, showed an almost instantaneous cessation of yield for any amine compound. After theorising on the cause, steps were taken to acquire the equipment and time needed to run *in-situ* pressurised X-ray absorption spectroscopy (XAS) in an attempt to elucidate if the issue was in response to a physical/electronic change brought upon by interaction of the material and palladium-hydride. A systematic study at the Diamond Light Source synchrotron highlighted key evidence for both the formation of hydride under solvent-only conditions, and the suspension of formation when in the presence of a reacting reagent such as crotononitrile. Upon exceeding 40 bar H_2, experimental results indicated total hydride formation, hypothesised as possible due to excess hydrogen accessibility. The corroborating data thus helped the generation of a hypothesis in which hydride formation within a reaction is in fact cripplingly detrimental towards nitrile hydrogenation due to modifications of the physical and/or electronic properties of the catalyst.

In this author's opinion, a plan of further action could easily be constructed in such a way to further enlighten the precise mechanics and interactions of the palladium-hydride phase within hydrogenation reactions. For example, with access to XAS again a systematic study of pressure in 5 bar increments focusing around the point of hydride formation could more accurately define the turning point. In addition, experimenting with gas mixtures could provide insight into whether the pressure is more important, or the abundance of hydrogen. For example, would we observe the same rate diminishing effect with 30 Bar hydrogen gas and 10 Bar nitrogen gas.

3.4 References

1. *World Development Report: Agriculture for Development*; The World Bank: 2008.
2. G. Lysenko, V. S., Willy H. Verheye, *Interactions: Food, Agriculture and Environment*. 2010; Vol. 2.
3. Caddick, S.; Judd, D. B.; Lewis, A. K. d. K.; Reich, M. T.; Williams, M. R. V., A generic approach for the catalytic reduction of nitriles. *Tetrahedron* **2003,** *59* (29), 5417-5423.
4. Haddenham, D.; Pasumansky, L.; DeSoto, J.; Eagon, S.; Singaram, B., Reductions of Aliphatic and Aromatic Nitriles to Primary Amines with Diisopropylaminoborane. *The Journal of Organic Chemistry* **2009,** *74* (5), 1964-1970.
5. Zhao, D.; Huo, Q.; Feng, J.; Chmelka, B. F.; Stucky, G. D., Nonionic Triblock and Star Diblock Copolymer and Oligomeric Surfactant Syntheses of Highly Ordered, Hydrothermally Stable, Mesoporous Silica Structures. *Journal of the American Chemical Society* **1998,** *120* (24), 6024-6036.
6. Bond Enthalpy (Bond Energy) http://www.kentchemistry.com/links/Kinetics/BondEnergy.htm (accessed June 2015).
7. Witte, P. T., A new supported rhodium catalyst for selective hydrogenation of nitriles to primary amines. *Collection of Czechoslovak Chemical Communications* **2007,** *72* (4), 468-474.

8. Ortiz-Hernandez, I.; Williams, C. T., In Situ Studies of Butyronitrile Adsorption and Hydrogenation on Pt/Al2O3 Using Attenuated Total Reflection Infrared Spectroscopy. *Langmuir* **2007,** *23* (6), 3172-3178.
9. Segobia, D. J.; Trasarti, A. F.; Apesteguía, C. R., Hydrogenation of nitriles to primary amines on metal-supported catalysts: Highly selective conversion of butyronitrile to n-butylamine. *Applied Catalysis A: General* **2012,** *445–446* (0), 69-75.
10. Hegedűs, L.; Máthé, T.; Kárpáti, T., Selective heterogeneous catalytic hydrogenation of nitriles to primary amines in liquid phase: Part II: Hydrogenation of benzyl cyanide over palladium. *Applied Catalysis A: General* **2008,** *349* (1–2), 40-45.
11. Storms, E. A student's guide to cold fusion, Chapter 5, II.2. http://www.lenr-canr.org/StudentsGuide.htm.
12. Bauer, M.; Schoch, R.; Shao, L.; Zhang, B.; Knop-Gericke, A.; Willinger, M.; Schlögl, R.; Teschner, D., Structure–Activity Studies on Highly Active Palladium Hydrogenation Catalysts by X-ray Absorption Spectroscopy. *The Journal of Physical Chemistry C* **2012,** *116* (42), 22375-22385.
13. Heterogeneous Catalytic Hydrogenation. *Platinum Metals Review* **2012,** *56* (4), 236.
14. Face Centred Cubic Structure. http://math.ucr.edu/home/baez/mathematical/face_centered_cubic.jpg (accessed 01/05/2016).
15. Clark, *Encyclopaedia of X-rays and Gamma Rays*. Reinhold: 1963.
16. Kawasaki, A.; Itoh, S.; Shima, K.; Yamazaki, T., Deformation of palladium plates by a small external stress during hydrogen absorption and desorption. *Materials Science and Engineering: A* **2012,** *551*, 231-235.
17. Diamond Synchrotron Components. http://www.diamond.ac.uk/Science/Machine/Components.html.
18. de Groot, F., High-Resolution X-ray Emission and X-ray Absorption Spectroscopy. *Chemical Reviews* **2001,** *101* (6), 1779-1808.

Chapter 4

Selective hydrogenation of allylic aldehydes using tuneable palladium-based catalysts

–

An investigation on the effect of nanoparticle characteristics and support architecture on cinnamaldehyde hydrogenation

4.1 Introduction

Previous work into the field of crotononitrile hydrogenation (**Chapter 3**) culminated in the discovery of a trend of high activity versus low selectivity upon palladium-based catalysts, able to be manipulated through changes in temperature, pressure, and catalyst structure. In an effort to further elucidate the nature of palladium nanoparticle catalysts, and bring to light further trends in regards to their role in selectivity and activity in hydrogenation reactions, this chapter focuses on selective hydrogenation of the simple aromatic aldehyde, cinnamaldehyde.

With both the amorphous silica (SiO_2), and mesoporous silica (SBA-15) catalyst series, this chapter will investigate the catalytic activity they demonstrate, involving comparisons to prior work performed within the group by Doctor Lee Durndell, using silica-supported platinum catalysts.[1] Beginning with conditions laid down in previous work, this chapter will detail the effects of modulated hydrogen accessibility, metal loading, temperature and pressure. Additionally, attention will be paid to the effects of the catalyst support upon the reaction, and also the importance of steric alignment for the reactant species. To further investigate this, work will be shown that delves into the effect of additional steric moieties within the reagent upon the activity and selectivity of the reaction.

4.2 Results and Discussion

4.2.1 Cinnamaldehyde hydrogenation

To begin, initial work was performed upon the cinnamaldehyde (CinnALD) hydrogenation *via* the same experimental parameters set out in **Chapter 3**, and also employed within prior work by the group. As this work was in essence a continuation of research on Platinum Group Metal (PGM) catalysts for aldehyde hydrogenation it was pertinent to begin testing under the same reaction conditions as set forth by the platinum work. The optimal conditions generated by the platinum work amounted to an ambient pressure reaction within a Radley reactor round-bottomed flask, run at 90° C. A magnetic stirrer flea maintained an 800 rpm perturbation whilst hydrogen gas was bubbled through *via* PTFE piping at 15 ml/min. Preliminary results with both series are shown in clusters for **Figure 4.1** and **4.2** (overleaf).

When considering the conversion of the starting material cinnamaldehyde for both catalyst series we can observe some clear trends in activity. Primarily, we can see that regardless of the catalyst loading, full conversion is observed by the two hour sampling point for the SBA-15 support. Although there is some variation in rate they all perform in much the same way. Comparatively, for the amorphous silica support we can see clear differences between each loading, with the highest loading taking two hours to fully convert, and the lowest taking seven.

In terms of reaction products we can see that for all catalysts we readily observe the formation of the saturated aldehyde, through C=C hydrogenation, and some small formation of the saturated alcohol through a combination of C=C and C=O conversion. In all cases, we see the steady conversion of CinnALD to the two carbon bond saturated products, mainly 3-phenyl propionaldehyde (PPA) and also 3-phenyl propan-1-ol (PP).

Previous work within this group and reported in literature with other metal nanoparticles such as platinum, have shown that this process will also form small amounts of cinnamyl alcohol (CinnOH) which can be compounded by altering the surface structure.[2,3,4] Notably for the palladium reactions, we observe a null synthesis for the desirable cinnamyl alcohol product. However, if we consider this from previous work in **Chapter 3**, and with reports within literature on the nature of palladium based aldehyde hydrogenation, this is a fairly predictable result.[5] It has been well determined that while palladium exhibits a high activity, its selectivity towards anything but carbon hydrogenation is lacking.

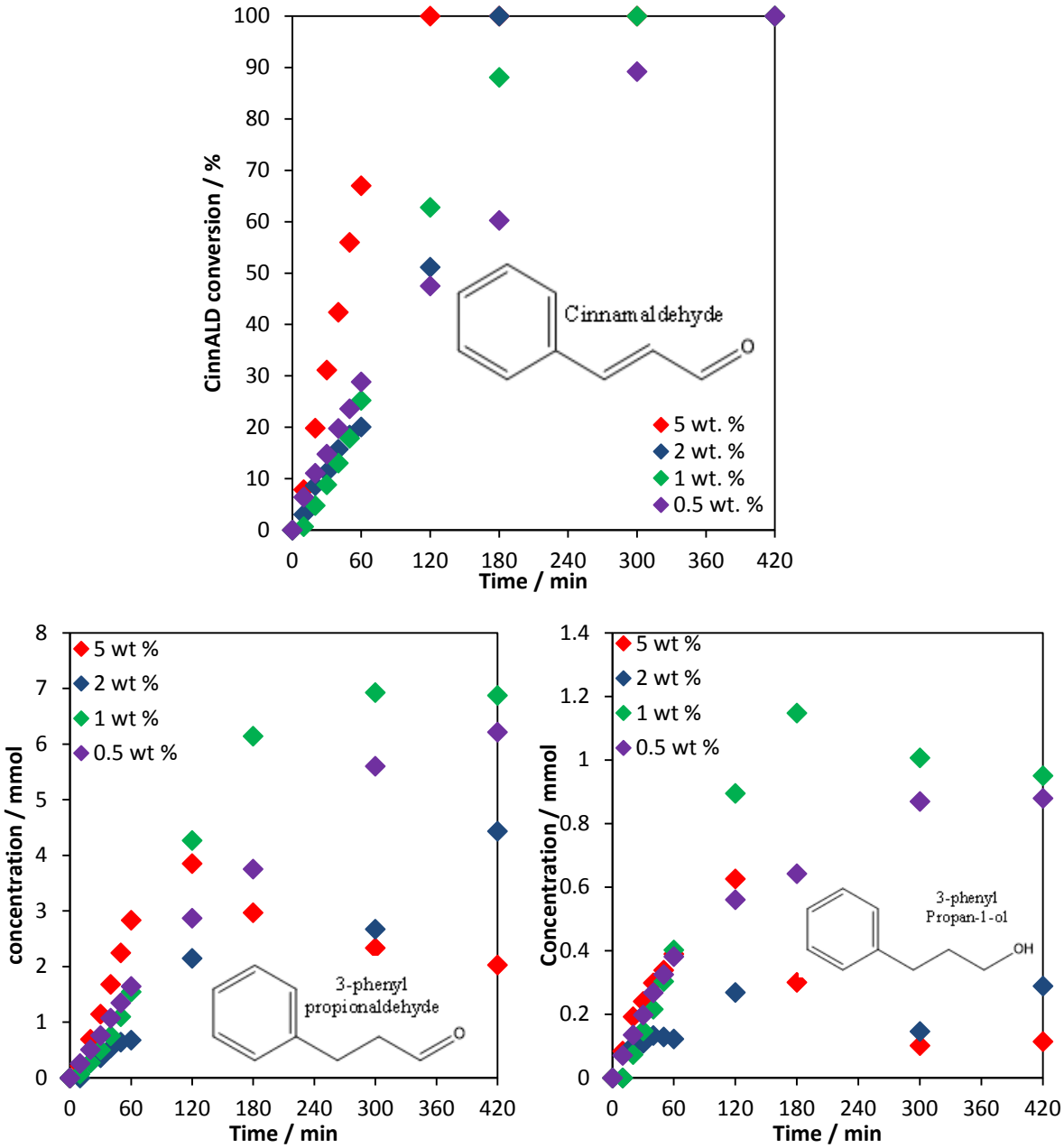

Figure 4.1 – Amorphous silica catalyst series, indicating conversion of CinnALD (**top**), and the formation of 3-phenylpropionaldehyde (**left**) and 3-phenyl propan-1-ol (**right**). (Conditions: anisole solvent, 90° C, 100 mg catalyst, 800 rpm, 15 ml/min H_2)

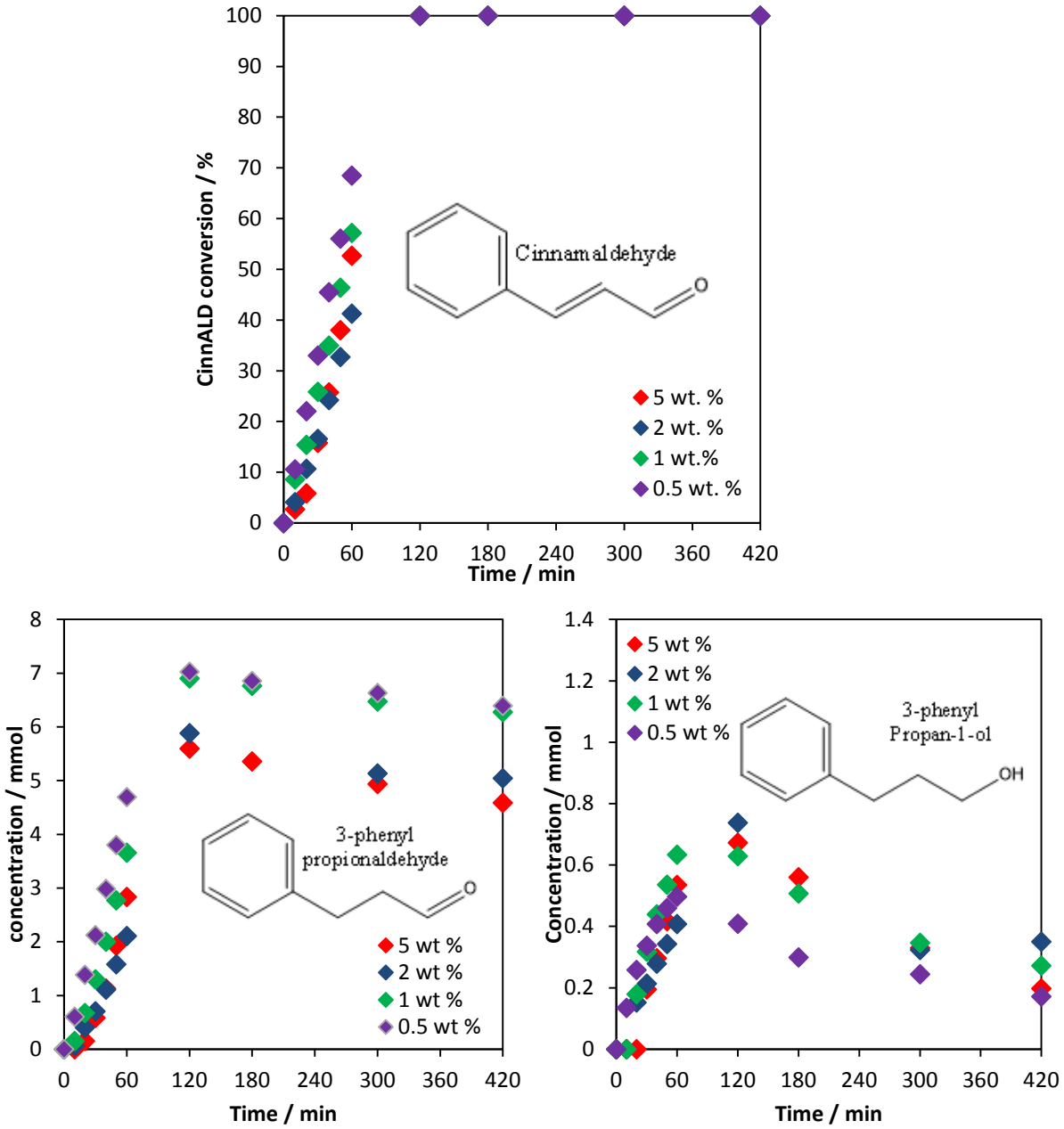

Figure 4.2 – SBA-15 supported catalysts, indicating conversion of CinnALD (**top**), and the formation of 3-phenylpropionaldehyde (**left**) and 3-phenyl propan-1-ol (**right**). (Conditions: anisole solvent, 90° C, 100 mg catalyst, 800 rpm, 15 ml/min H_2)

When considering these initial tests within an 'open' Radley reactor we also observe the slow consumption of the reaction products. As this reaction is running at 90° C and the boiling point of these products is close to this level, it is hypothesised that some of the product was evaporating from the reaction mixture and escaping the reaction entirely. A small peak was sometimes identified at later stages of the reaction that may be attributed to dimerisation of the reagent material that may also account for a small amount of the loss.

If the initial rates of these reactions are taken and normalised per gram of Pd present, and compared against all catalyst in the series, we can observe the trends outlines in **Figure 4.3**. As we can see, for both catalyst types the activity per gram of Pd rapidly increases as the overall loading of palladium decreases. The effect is more pronounced for the SBA-15. This is due to the fact that whilst more metal is indeed being added to the catalysts, it is not all contributing as active sites, as particles will grow and more will be lost within blocked or inaccessible pore structure. As such, the lowest loadings will display the best activity per g of metal, as they have the highest ratio of active sites to total metal. The effect is compounded for SBA-15 due to its larger surface area and metal distribution.

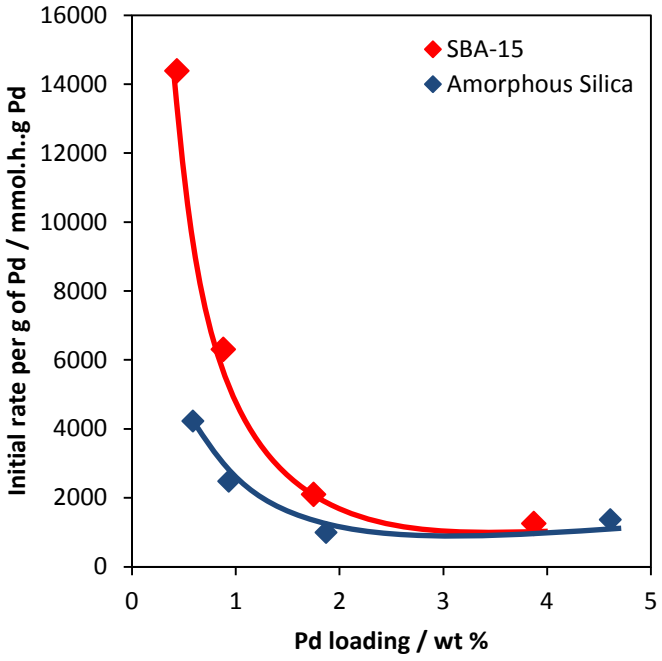

Figure 4.3 – Plot of normalised initial rate as a function of the metal loading for both SiO_2 and SBA-15 catalyst series, indicating an exponential trend of activity over loading. (Conditions: anisole solvent, 90° C, 100 mg catalyst, 800 rpm, 15 ml/min H_2)

In comparison to work done with platinum, the rates here are significantly higher in all cases, with internal group work showing a maximum of 800 $mmol.h^{-1}.gPt^{-1}$ on both supports.[1] This trend of heightened activity with palladium metal in comparison to other transition elements is in agreement with the literature.

In addition reactions were run, as with **Chapter 3**, with only the support materials, or with no material at all. All reactions indicated a total lack of conversion without the presence of palladium nanoparticles, confirming that this reaction cannot be driven purely thermodynamically, and must contain a catalyst in order to proceed.

Having run the initial reactions within round-bottomed flasks set within a Radley reactor, several issues were quickly identified. Most prominent were issues with hydrogen accessibility and bubbling. Relying on low pressure gas lines to force relatively low flow rates through a handful of flasks meant that there were often issues with maintaining a uniform flow of hydrogen. Additionally, as mentioned earlier, we would observe loss of product over time was observed due to what was suspected as external effects or loss through the open system. As a result it was quickly decided that reactions should proceed within the Parr autoclave used for the crotononitrile work, but performing under 1 bar of hydrogen. In this way the issues with bubbling and the open system could be accommodated for, whilst maintaining similar reaction parameters to those performed for the platinum work.

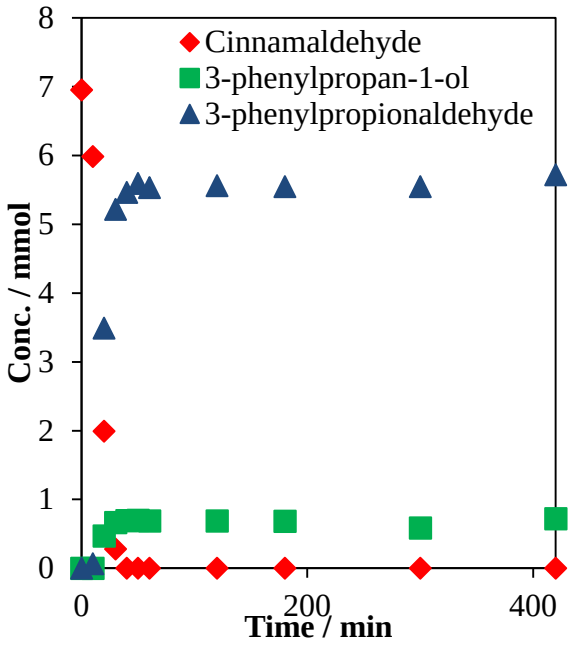

Figure 4.4 – Plot of reagent and product concentrations over a typical autoclave reaction (0.88 wt. % Pd/SBA-15, 100 mg, 90° C, 1 bar H_2, 800 rpm)

With **Figure 4.4**, we see one of the standard reactions repeated within the Parr autoclave. While the reaction rate is slightly improved due to the higher abundance of hydrogen, there is no appreciable difference in selectivity. Furthermore, the results are significantly more stable and agreeable, whilst showing no signs of product loss. As with **Chapter 3**, efforts were made to determine if the perturbation speed of the impeller exceeds that needed for the mass flow limitation. By running a series of experiments at steadily increasing stirrer speed, a point of initial rate plateau was worked towards (**Figure 4.5**).

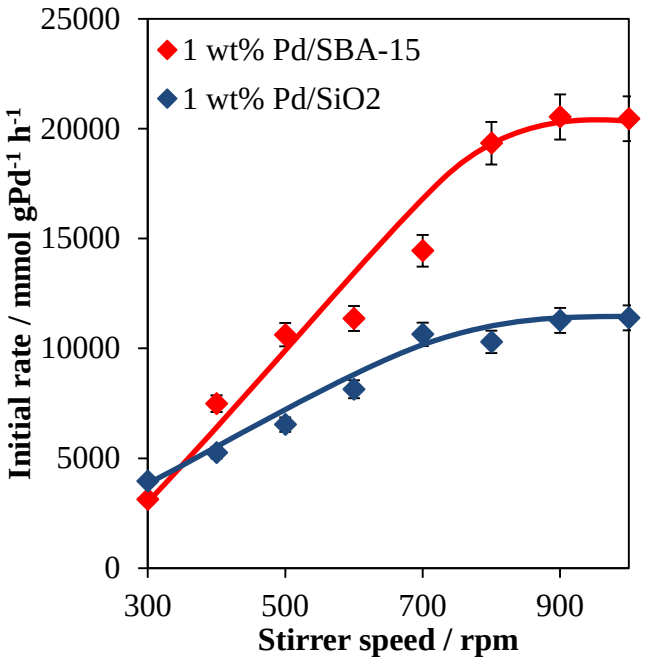

Figure 4.5 – Plot of normalised initial rate per gram of Pd for CinnALD hydrogenation as a function of stirrer speed using an overhead impeller and autoclave reactor (100 mg, 90° C, 1 bar H_2, 300-1000 rpm)

As shown above, we can see a clear trend of increasing initial rate up to a plateau at 800 rpm. As expected with previous work comparing the two supported catalysts, the SBA-15 supported palladium performed consistently better than that upon the fumed silica. As a result, this supports the experimental parameters initially set for this work, and those used within the platinum work.

The platinum work, run by Dr Durndell showed a plateau of approximately 700 rpm, with a peak metal-normalised initial rate of 200 $mmol.h^{-1}.gPt^{-1}$. Most notably here and in conjunction with prior work done in this chapter, is the significant increase in the initial rate of reagent consumption with palladium compared to platinum. In addition, whilst the platinum work showed very similar rates on both catalysts, the palladium work performed here showed a vastly greater rate with the SBA-15 supported catalyst. The fumed silica

catalyst achieved roughly 50 times the rate, and the SBA-15 showing a 100 times increase, which are vastly superior even accommodating for the doubling in atomic mass between the two elements. However the selectivity of the reaction must also be considered, when accounting for the efficacy of the catalyst. With this information in mind, subsequent reactions were continued at the 800 rpm perturbation speed, with assurance that optimal mixing is being achieved at this speed set.

4.2.1.1 Probing the reaction pathway

With a combination of prior work in this group with platinum catalysts, literature sources, and prior work within this chapter, it is clear that this reaction does not elicit a clean-cut selectivity towards one product.[6,5,7,8] With the potential for C=C hydrogenation and C=O hydrogenation to occur both exclusively, or sequentially, it was important to delve into the reaction pathway. To this end, tests were run not only with the standard reagent but also with each subsequent intermediate or product, to better grasp the relative rates and interactions taking place at each stage.

Reactions were run under standard autoclave conditions with cinnamaldehyde, the unsaturated 'desired' alcohol product cinnamyl alcohol, and the saturated aldehyde 3-phenyl propionaldehyde. By obtaining the initial rates for each step and normalising to palladium content, we would then generate a kinetic diagram for the reaction. By performing these reactions one step at a time we can also shed light on any unforeseen chemical interactions. For instance, it may be discovered that one compound requires the presence of another, for instance a precursor, to react at all. Comparisons were made for 1 wt. % Pd on both the amorphous silica and also SBA-15 catalysts (**Figure 4.6**).

As previously described within this chapter, under standard conditions, reactions containing cinnamaldehyde (CinnALD) proceed along two paths. The formation of the saturated aldehyde 3-phenyl propionaldehyde (3-PPA) occurs with a high rate for both catalysts, but almost double in the presence of the SBA-15 supported catalyst. Additionally, the formation of the saturated alcohol, 3-phenyl propan-1-ol (3-PP) occurs, at a much reduced rate, and with a slightly higher responsiveness with the SBA-15 catalyst.

Within these reactions we observe no formation of the unsaturated alcohol, cinnamyl alcohol (CinnOH). In order to understand if the cinnamyl alcohol could be formed from one of the intermediates under isolation and to see if 3-PPA reacts alone to form 3-PP, the additional reactions were performed.

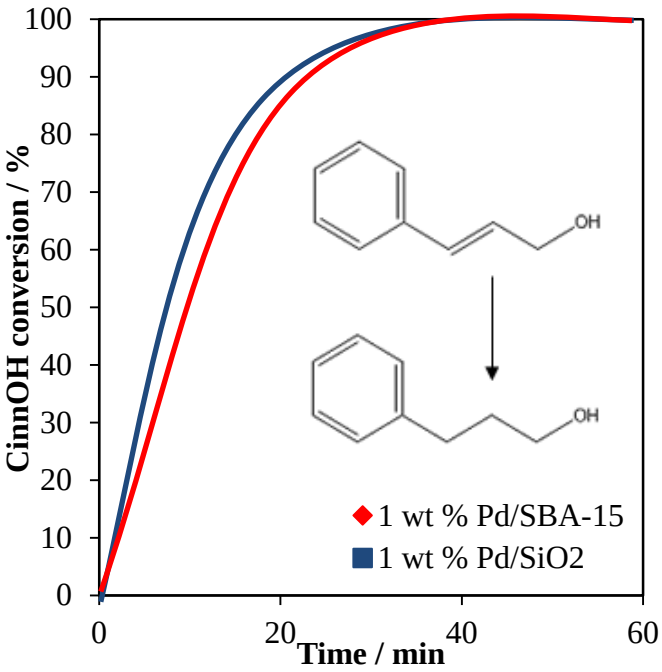

Figure 4.6 – Plotted data of cinnamyl alcohol conversion to 3-phenyl propan-1-ol with nominal 1 wt. % Pd on both supports (100 mg, 90° C, 1 bar H_2, 800 rpm)

Firstly, as shown above in **Figure 4.6**, we observed the expected result that cinnamyl alcohol will only perform a C=C hydrogenation to 3-PP. Notably, the initial rates are very high with conversion after 30 minutes, and closely agreeable for both catalysts, with 19118 mmol h^{-1} gPd^{-1} for SBA-15 and 19297 mmol h^{-1} gPd^{-1} for the amorphous silica support. In addition, no by-product chemicals such as ethyl benzene were observed, suggesting that we do not observe any over-hydrogenation leading to bond cleavage. When testing the saturated aldehyde 3-PPA in isolation, we obtained the most curious result. From both catalysts we observed a null reaction, with absolutely no conversion of the starting material into the saturated alcohol 3-PP, nor any by-products, for the duration of the test. With previous evidence with cinnamaldehyde showing the formation of this alcohol, albeit slowly, we must conclude that it is integral for the starting reagent to contain the C=C bond.

Work within the literature, and within this group, detail the effects of steric interaction for this particular process. Multiple sources corroborate to espouse the necessity of ideal reagent alignment for effective catalytic activity. Future sections of this chapter will address these, in large part due to the results observed here. The conclusion that can be drawn by this author is that the reagent will align upon the nanoparticle active site, using the C=C bond as an anchor. Under these conditions, the chemical may align in the most optimal position, and can undergo C=O hydrogenation.

With this data to hand, we can consider a kinetic diagram for the reaction of cinnamaldehyde with palladium nanoparticles upon both SBA-15 and amorphous silica. In this way we can clearly see difference in selectivity between C=C and C=O hydrogenation, and also the necessity of optimal steric alignment and atomic interaction (**Figure 4.7**).

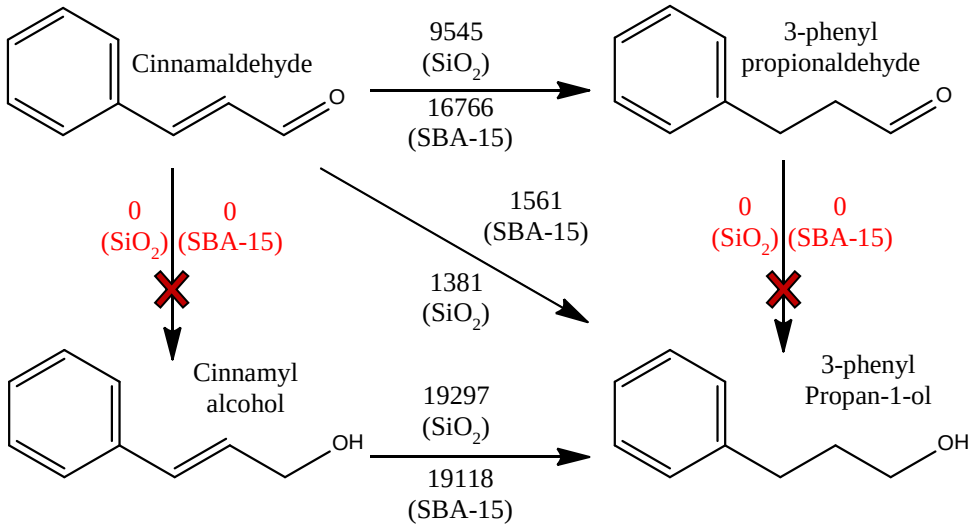

Figure 4.7 – Kinetic network for cinnamaldehyde (CinnALD) hydrogenation for nominal 1 wt. % Pd on both SiO_2 and SBA-15 catalysts. Values indicate normalised initial rate ($mmol.h^{-1}.g_{Pd}^{-1}$). (100 mg, 90° C, 1 bar H_2, 800 rpm)

If we compare the results of this palladium based work with that done in the group with platinum we can draw some stark comparisons on the reactivity and selectivity of these metals. By observing the kinetic diagram previously produced within the group we can highlight some of the key differences between the two studies (**Figure 4.8**).

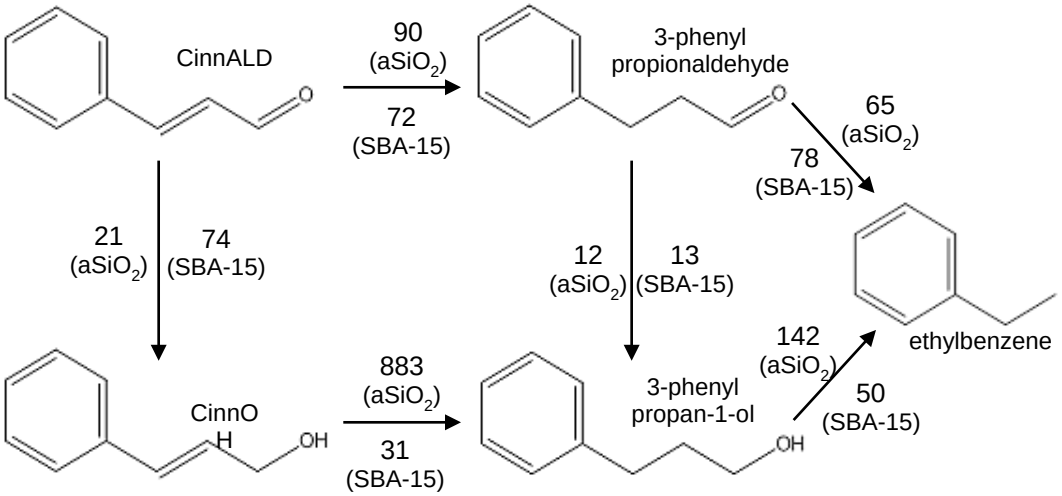

Figure 4.8 – Copy of the kinetic network for comparative platinum cinnamaldehyde (CinnALD) hydrogenation for nominal 1 wt. % Pt on both SiO_2 and SBA-15 catalysts. Values indicate normalised initial rate ($mmol.h^{-1}.g_{Pd}^{-1}$).[1]

Firstly we can note that the cinnamaldehyde reacts to form both the 3-PPA and the CinnOH. For the SB-15 the rate is very similar, but with the amorphous silica the formation of the saturated aldehyde is preferred. What we can clearly see from this comparison is that while the platinum is able to achieve the selective hydrogenation of the aldehyde, the overall activity of the reaction is magnitudes slower than for palladium. For the cinnamyl alcohol reaction, the rate is much improved for platinum on amorphous silica, yet we can see that the palladium catalyst can achieve more than 20 times this rate. Simultaneously, we can see that the SBA-15-supported catalyst is highly inactive for this step with platinum, hundreds of times slower than its palladium counterpart.

Whereas with the palladium tests we could observe no formation between 3-PPA and 3-PP, it was reported that a very small activity was detected with platinum catalysts. In addition, both 3-PPA and 3-PP underwent over-hydrogenation in their isolated platinum reactions, and proceeded to form the cleaved structure of ethylbenzene.

This overall trend of increased selectivity in return for significantly reduced activity agrees with work previously done in this chapter on the nature of cinnamaldehyde hydrogenation. The observation of ethylbenzene may also support this notion, due to the fact that if platinum contains active sites with a high enough energy to break the C=O bond, so too could it totally cleave the C-C bond. The notion that amorphous silica-supported platinum catalysts had overall superior activity to that upon SBA-15 is something addressed within previous work within the group, and considers the effect of polarity upon steric alignment. This is discussed in a later segment of this chapter.

4.2.1.2 Effect of H_2 pressure

Within both the atmospheric Radley reactors, and within the 1 bar H_2 pressurised autoclave system we can determine that, in much the same way as **Chapter 3**, palladium performs at an expedited rate but with a significant propensity towards the C=C bond over the C=O.

As with the previous chapter, and in line with work done within the group of a similar nature, a series of reactions were performed in an effort to understand the effect of increased hydrogen pressure on the aldehyde hydrogenation reaction. Foremost was observations of initial rate and substrate conversion, but specific focus was paid towards any potential changes in selectivity that we may observe under these conditions.

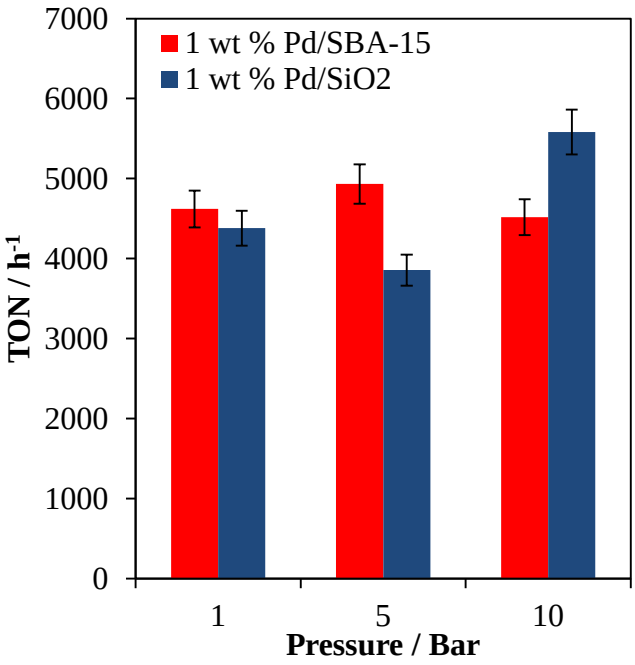

Figure 4.9 – Evaluation of Turnover Number of nominal 1 wt. % Pd upon both supports after seven hours, as a function of hydrogen pressure. Results indicate a curved effect, with 5 bar H_2 as the most optimal pressure for TOF (100 mg, 90° C, 1-10 bar H_2, 800 rpm).

In line with the work done with platinum, experiments were performed at 1, 5 and 10 bar hydrogen within the autoclave system (**Figure 4.9**). When observing the results shown in **Figure 4.9**, we can easily conclude that there is little difference in the Turn Over Frequency (TOF) of the reaction at these pressures. All three fall within a very close range for TOF value, with only the 10 bar reaction with amorphous silica showing any signs of deviation. This set of data may be explained in a few ways. The most obvious reason would be that the reaction proceeds too rapidly for significant differentiation of the reaction rate to be deduced. As a result the figures appear much the same. In this scenario if the reagent was significantly increased or the temperature decreased we may see some more spacing of the TOF number.

The second reason may be that the pressure for these experiments is simply too low for any reasonable effects to be identified. If we consider the results observed within **Chapter 3**, we see that the most significant changes in the activity/selectivity of the experiment occurred at higher pressures than those being worked at here. It is believed by this author that working at even higher pressures would yield more easily identifiable differences. However, it is also important to consider that the hydride effect as outlined before within **Chapter 3** may come into play with these reactions, especially if the overall process is more sensitive to physical/electronic structure manipulation.

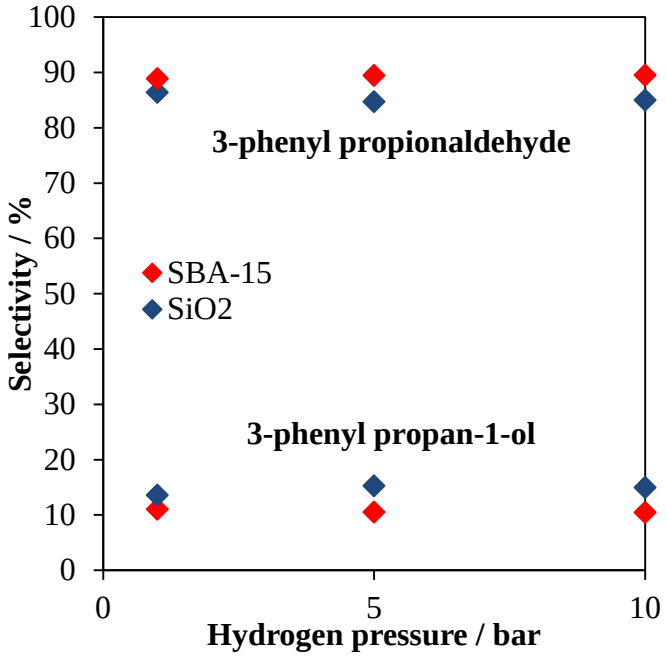

Figure 4.10 – Graph indicating the selectivity towards the saturated aldehyde and saturated alcohol for both catalysts as H_2 pressure varies (100 mg, 90° C, 1-10 bar H_2, 800 rpm).

As we can see in **Figure 4.10**, with the increase in pressure we see a completely negligible effect upon the selectivity of the reaction. Upon conversion of the starting material we see that the 3-phenyl propionaldehyde (3-PPA) is present in the largest amount an accounts for 85-89% of the products, with the remainder being formed of the 3-phenyl propan-1-ol product.

At none of the pressures is any of the unsaturated alcohol detected. This was to be expected, as increasing the energy and/or pressure of the reaction would only serve to increase the propensity towards hydrogenation reactions. With the C=C bond being much easier to convert than C=O, this would only lead to conditions even more favourable to the formation of the saturated products.

Interestingly however, we see no increase in the C=O hydrogenation even at 10 bar. By referring to the previous work in this chapter on the nature of the reaction, we can conclude that this is in agreement with the proposed theory on reagent alignment. In the previous section it was commented on that the reagent needed the C=C bond present for C=O hydrogenation. The evidence here supports the supposition that this activity is dependent on product alignment and active sites, and not on factors such as hydrogen pressure. It is believed that even at higher pressures we would still observe this trend.

4.2.2 Extended characterisation of Pd catalysts with DRIFTS

In an effort to better understand the mechanisms and factors responsible for the cinnamaldehyde hydrogenation, further characterisation techniques to those already run in **Chapter 3** were performed.

Previous work on the nature of cinnamaldehyde hydrogenation over supported platinum catalysts within the group looked into the nature of the silicon support for the nanoparticles. It was suggested that silanols, a moiety designated as Si-O-H, were present in varying quantities on the surface of the silica supports. These groups can be present either as isolated, geminal, or vicinal. Each has a different stretching frequency, as indicated in **Figure 4.11**, meaning that IR spectroscopy *via* Diffuse Reflectance Infrared Fourier Transform Spectroscopy (DRIFTS) becomes possible.

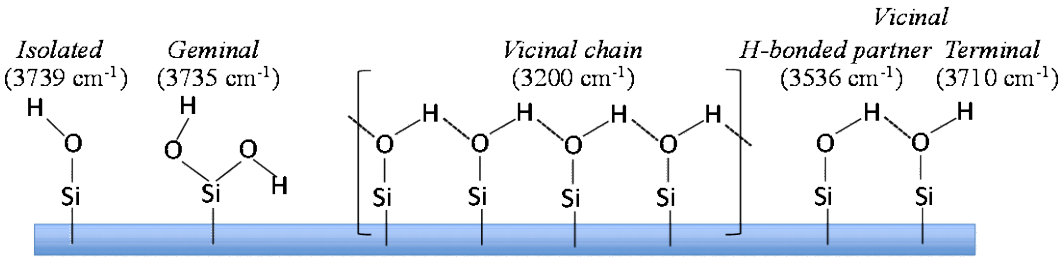

Figure 4.11 – Visual representation of the various silanol types and their corresponding IR stretching frequencies.[1]

Based on literature reports[9,10] and the findings within our own group[1] it was shown that these polar groups increased the overall polarity (and thus hydrophilicity) of the catalyst. In relation, it was shown that the higher the polarity of the catalyst, the greater the selectivity. This was used as part of a larger explanation for catalytic activity, suggesting that the polarity was a key part in the correct alignment of reagent upon the metal nanoparticles. The most polar catalysts were found to be the most selective as they could force the cinnamaldehyde to align in the optimal position for hydrogenation.

DRIFTS upon both the blank SBA-15 and amorphous silica support, and the representative nominal 1 wt. % Pd upon both supports was performed, with the resulting spectra displayed in **Figure 4.12**. For the supports we can see that there is evidence for Isolated silanols upon the amorphous silica, and a slight suggestion of Geminal/Vicinal forms. For the SBA-15 support we can see a much larger quantity of both, especially in respect to the Geminal/Vicinal group.

This effect is somewhat diminished upon introduction of the palladium metal to the supports. However this is to be expected, as the introduction of the metal to the surface will effectively block many of the sites that previously contained silanols. Additionally, the curing process, namely calcination and reduction, will likely have degraded the surface species.

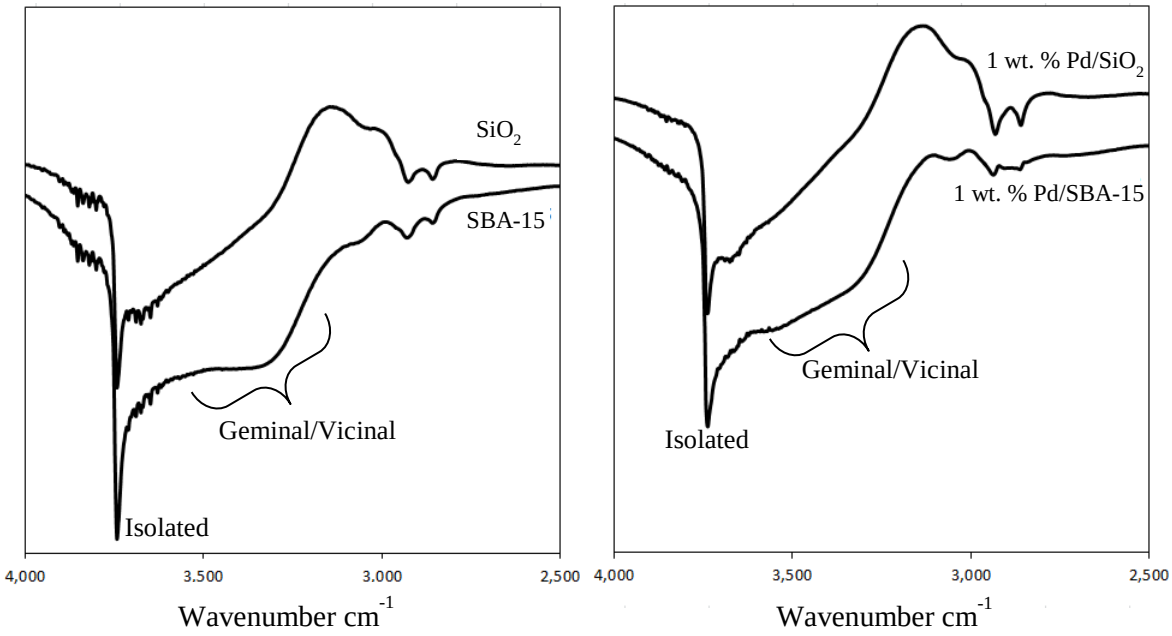

Figure 4.12 – *In vacuo* DRIFT spectra for blank catalyst supports (left) and impregnated 1 wt. % Pd supports (right).

If we were to consider the results with platinum, we would expect this to mean that SBA-15 supported catalysts would indicate a much greater selectivity towards the alcohol product. However, from the evidence put forth thus far, this can be shown to not be the case for palladium. Referring to the kinetic diagram (**Figure 4.12**), we can safely conclude that regardless of support the propensity towards alcohol formation is almost identical, and neither can successfully form the unsaturated cinnamyl alcohol under standard conditions.

It can thus be concluded that whilst platinum reactions are highly sensitive to the polarity of the support, the same cannot be said for palladium. This is, as mentioned before, likely due to the ease and strength at which palladium can facilitate the adsorption of reagents. The reason for this can be explained due to strength of adsorption. Known as the Sabatier principle, this concept outlines the interactions between a catalytic site and the substrate.

By plotting the reaction rate against the heat of adsorption, you end up with a 'volcano plot' curve upon which the transition elements fall. Palladium, as compared to platinum, falls further to the left on this plot. As a result, it is considered to have higher overall adsorption strength. In some cases this can be detrimental as you will then encounter issues with the product not readily desorbing after the reaction has taken place. However, based on the comparison of the two metals, and the relative reaction rates obtained, it can be safe to say that the palladium fits closer to the optimal region for adsorption/desorption capability. This would explain why we see a different between the two. The strength of adsorption with palladium overcomes the repulsive force of the silanols, which often prevent adsorption upon platinum.

As a potential hypothesis, this may also be used to explain why we see no sign of unsaturated aldehyde products. Because the adsorption strength is that much higher, the reagent remains on the surface too long and as a result the C=C hydrogenation will occur in every case. In comparison, with platinum we see this repulsive effect from the silanols, but if this can be overcome the surface adsorption is transient enough that the C=O hydrogenation may proceed whilst still avoiding the C=C hydrogenation. In addition, the effects of surface alignment and the speed/precision at which this occurs may play a role in the differences here. As such, further work was done to look at substrate alignment.

4.2.3 Alternative substrates – Substituted benzaldehydes

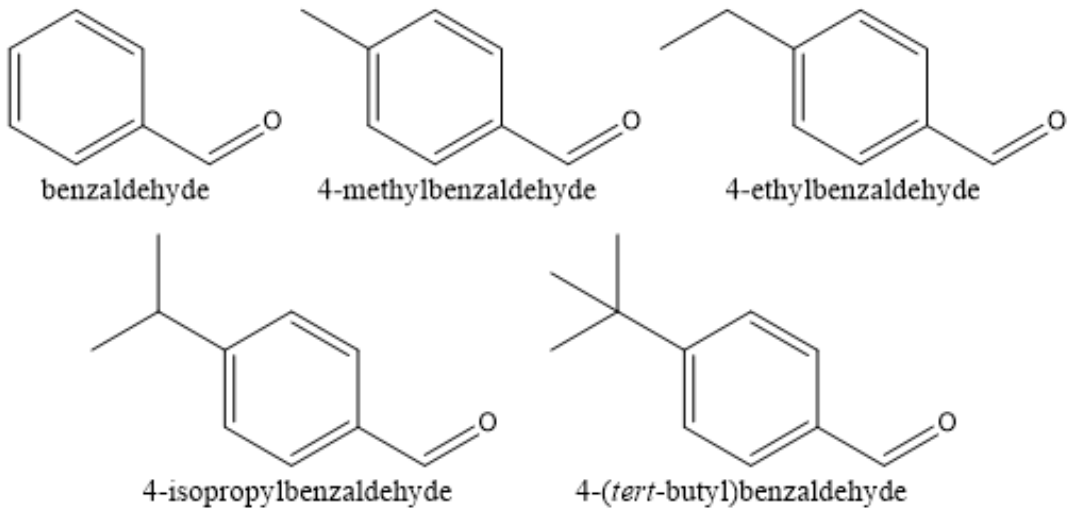

Figure 4.13 - Molecular structure of screened aromatic (benzylic) aldehydes, with steadily increasing hindrance through steric moiety in the *para* position to the aldehyde group

With previous work by the group and reported within the literature espousing the effect of molecular orientation upon the reaction rate, efforts were taken to discover how far these effects may carry. The prior utilised 1 wt. % Pd/SiO_2 and Pd/SBA-15 were therefore further tested with a selection of aromatic aldehydes, as shown in **Figure 4.13**. These new compounds were chosen due to the increasingly large or obstructing steric group bonded to the para position of the aldehyde. The experiments were laid out in the hopes to elucidate the effect of support polarity along with substrate steric effects upon the surface site alignment.

Initial theories on this experiment proposed that a systematic test with the 'standard' benzaldehyde, along with the *para* methyl, ethyl, *iso*-propyl and *tert*-butyl forms, would highlight an increasing trend of steric hindrance in correlation with the relative size and shape of the additional moiety. Specifically, by preventing the ideal alignment of the reagent, we would expect to see a decreasing trend in reaction rate in direct correlation to the size of the steric group. Screening occurred under the same standard reaction conditions for aldehyde hydrogenation as highlighted in previous sections of this chapter.

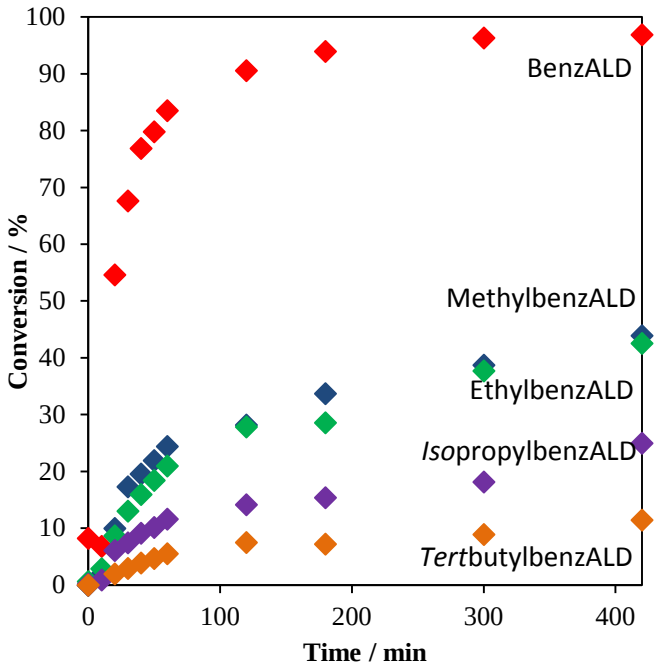

Figure 4.14 – Overlaid plots of the varying conversion rates of benzaldehyde and each of the functionalised forms, as a function of time. Results indicate a correlation between the size of the steric group and the reaction rate (100 mg, 90° C, 1 bar H_2, 800 rpm).

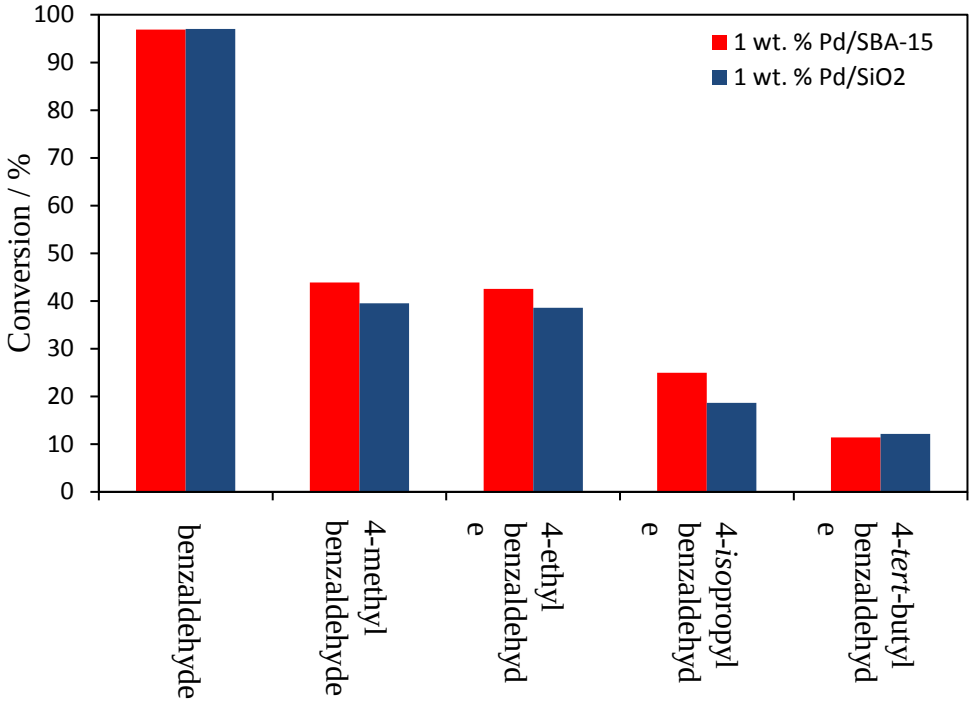

Figure 4.15 – Overall performance of 1 wt. % Pd/SBA-15 and Pd/SiO2 catalysts upon the hydrogenation of substituted benzaldehyde reagents after 7 hours. Data indicates a steady decrease in conversion as the steric hindrance of the *para* moiety increases. (100 mg, 90° C, 1 bar H_2, 800 rpm)

By observing the generated plots of conversion over time (**Figure 4.14**), and the graphic comparison of the overall conversion at the end of the reaction (**Figure 4.15**) a clear trend becomes apparent. Of initial interest is the comparison of both the standard silica (SiO_2) and mesoporous structure (SBA-15). In all cases, the discrepancy is at most 4%, as in the case of the *iso*propyl reagent.

This is significant when compared to previous work by this group with the PGM catalytic comparison with platinum.[1] In the case of that work, a consistent improvement of between 15-20 % in favour of Pt/SBA-15 can be ascertained. The hypothesis for this discrepancy in activity was proposed to be due to the more polar properties of SBA-15, having upon its surface a higher concentration of silanol species. It was determined that the greater presence of aromatic-silanol group repulsion resulted in faster desorption kinetics with this catalyst. Clearly, as indicated by this work with the palladium in place of platinum, this kinetic effect upon the nanoparticles is much less pronounced

Secondly, before the specifics of each reagent are discussed, it is important to remark upon the conversion of the substituted benzaldehyde compounds with the aid of the palladium-based catalysts. With previous work with platinum nanoparticle catalysts, conversion reached, at most, 16% with the ethyl benzaldehyde substrate upon 1 wt. %

Pt/SBA-15 and, at the least, 7% for the benzaldehyde reaction upon 1 wt. % Pt/SiO_2. In the case of the work documented above, the highest conversion is at 97% for benzaldehyde, and at its lowest (the only instance of lower activity compared to platinum) a conversion of 11.5% with *tert*-butyl benzaldehyde.

Beginning with the near-total conversion of benzaldehyde over the palladium catalyst, it is of interest to note the significant drop in activity to approximately 40% for both the methyl and ethyl-substituted benzaldehyde. Following from this we see a further decrease in conversion for the *iso*propyl benzaldehyde, before a subsequent final shift for *tert*-butyl benzaldehyde. As a result from the data evident from these experiments we can conclude that for palladium, as compared to prior platinum work, the steric effect upon the reaction is a far more pronounced factor than that of the desorption kinetics.

As shown in **Figure 4.16**,[11] the alignment of the reagent upon the supported metal nanoparticle is integral for the reaction to take place. Lacking any hindrance, the benzaldehyde can align itself in the most optimal position upon the palladium nanoparticles, and thus obtain a high kinetic rate.

However, once a *para*-substituted methyl group is incorporated into the structure, the reagent finds itself no longer able to align as effectively as before. As illustrated in the diagram, the presence of this group will cause a strain upon the reagent whilst attempting to align itself upon the metal.

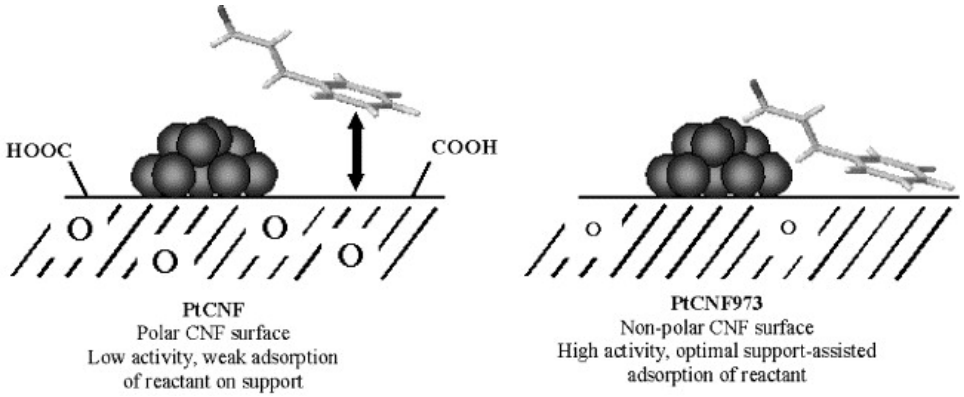

Figure 4.16 – Example schematic indicating the adsorption of cinnamaldehyde over a supported metal nanoparticle, highlighting both the steric importance of para-substituted groups upon the reaction, and the effect of support polarity (modified diagram[11]).

With the ethyl-substituted group the effect is much the same as with the methyl. It is suggested by this author that this is due to the nature of the steric group. As both the methyl and ethyl group only apply strain in one dimension, the effect upon the rate is much

the same. However, upon introducing the branched *iso*propyl benzaldehyde, the situation is markedly changed. Now, the steric effect is applied at new angles due to the *iso* configuration, creating a more difficult reactive condition for the reagent, when attempting to align upon the palladium catalyst. This effect is then further compounded by the presence of a fourth carbon in *tert*-butyl benzaldehyde, with the *tert* configuration exacerbating the already unfavourable steric hindrance as found in the *iso*propyl reagent.

In terms of selectivity for these reactions, for all the substituted benzaldehyde chemicals (methyl through to *tert*-butyl) the only detectable product was the corresponding alcohol. In the case of the benzaldehyde, there is a slow and steady formation of methylbenzene (toluene) through the act of over-hydrogenation, fully cleaving the C-OH bond.

This can be used to further reinforce this concept of correct steric alignment. With the benzaldehyde positioning itself upon the surface in such a favourable way, we can observe complete conversion of the starting material. However, this coordination can lead to the reagent remaining at the active site for too long, resulting in C-OH hydrogenation and the formation of the toluene unwanted by-product in some small amounts.

Due to the time limitations of this work, the author was unable to obtain further results to support this hypothesis on the nature of the steric groups, but is confident that if a reaction were to be run with the straight chain propylbenzaldehyde, as opposed to the branched *iso* form, we would observe a similar rate to that shown for the methyl and ethyl groups. Additionally, if more extensively branched groups were introduced, we would expect to see a further decrease in the overall rate of reaction, or a total cessation of the reaction altogether.

Finally, we can consider the similarity between both the amorphous silica and SBA-15 supported catalysts overall conversion. With a maximum of 6% discrepancy, it is in this author's opinion that the support does not play a significant role in reagent alignment upon palladium. The difference in reagent consumption could be attributed mostly to experimental and machine error, but also due to the retentive nature of the porous structure of SBA-15, leading to a perhaps artificially larger conversion of starting material.

Most notably, this finding is in stark comparison to the results of the platinum-based hydrogenation work. As mentioned before in the section on DRIFTS analysis, the presence of the silanol groups affects the activity and selectivity of these reactions when Pt is used. Here, however, there is very little in the way of discrepancy

between the two supports, despite evidence suggesting a much higher presence of geminal/vicinal silanol groups within the SBA-15 catalysts. The immediate conclusion to this is that the silanol groups contribute very little to the alignment of the reacting agents upon the surface of palladium. This is most easily explained by the strength of adsorption. As mentioned before, palladium adsorbs species much more readily and strongly compared to platinum as instanced by the Sabatier principle. This is a benefit in terms of activity, but is also responsible for the signature low-selectivity that we have addressed in all prior work herein. Whilst the previous hypothesis denoted that platinum had the benefit of more transient adsorption upon the surface, these results may complement it with evidence for the reverse. With palladium, the adsorption is so strong that the substrate may fixate upon the surface with no heed for optimal alignment. In this way we would observe that the correct alignment for C=O selective hydrogenation would very rarely be achieved, and would thus compound the effect already present from the effect of the weak platinum adsorption. Both factors work against palladium in this regard.

4.3 Conclusion

In summation of the work performed within this chapter on cinnamaldehyde hydrogenation we can draw several key conclusions. Foremost is that, in much the same manner as **Chapter 3** and the work on crotononitrile, palladium exhibits a strong activity coupled with a low selectivity towards the hydrogenation of species other than carbon double bonds. To this end, C=C hydrogenation occurs at a staggering rate, whilst C=O hydrogenation occurs much slower, with the formation of cinnamyl alcohol through selective hydrogenation never observed. With comparison to identical platinum-based work palladium exhibits significantly increased activity at the cost of selectivity.

In considering the effect of increased hydrogen pressure we can determine that very little effect can be found in the range of 1-10 bar. This has been explained due to the already great rate of reaction and a difficulty in differentiating at these speeds. Additionally, the lack of any change in selectivity was explained through the determination that active site and alignment were more important than hydrogen accessibility or energy.

Continuing on the theme of alignment, intriguingly, when creating a kinetic diagram for this reaction, it was discovered that the C=C bond plays a vital role in the hydrogenation of the C=O bond. By adsorbing in such a fashion as to align the reagent favourably, the C=O can also undergo hydrogenation. However, if this carbon double bond is absent, the reaction cannot be undertaken.

Following this thread, an analysis of the support properties of the catalysts determined that whilst SBA-15 contained significantly more polar silanol groups, these exerted no effect upon the selectivity of the reaction, in stark contrast to the sensitive nature of the analogous platinum work. Drawing on other lines of research, this can be explained through the strength/propensity of adsorption upon palladium, which also goes some way to explaining the lack of unsaturated alcohol formation under these conditions.

Finally, when further exploring the systems of this reaction a set of experiments with increasingly significant steric hindrances were run. These studies showed that while surface polarity does not affect alignment and activity, physically hindering moieties assuredly do. The greater the angular inhibition of the group the lower the overall activity, further justifying the hypothesis that alignment upon the metal is absolutely integral to this reaction and to the overall activity and selectivity within.

4.4 References

1. Durndell, L. J.; Parlett, C. M. A.; Hondow, N. S.; Isaacs, M. A.; Wilson, K.; Lee, A. F., Selectivity control in Pt-catalyzed cinnamaldehyde hydrogenation. *Scientific Reports* **2015,** *5*, 9425.
2. Durndell, L. J.; Wilson, K.; Lee, A. F., Platinum-catalysed cinnamaldehyde hydrogenation in continuous flow. *RSC Advances* **2015,** *5* (97), 80022-80026.
3. Tsang, S. C.; Cailuo, N.; Oduro, W.; Kong, A. T. S.; Clifton, L.; Yu, K. M. K.; Thiebaut, B.; Cookson, J.; Bishop, P., Engineering Preformed Cobalt-Doped Platinum Nanocatalysts For Ultraselective Hydrogenation. *ACS Nano* **2008,** *2* (12), 2547-2553.
4. Fechete, I.; Wang, Y.; Védrine, J. C., The past, present and future of heterogeneous catalysis. *Catalysis Today* **2012,** *189* (1), 2-27.
5. Delbecq, F.; Sautet, P., Competitive CC and CO Adsorption of α-β-Unsaturated Aldehydes on Pt and Pd Surfaces in Relation with the Selectivity of Hydrogenation Reactions: A Theoretical Approach. *Journal of Catalysis* **1995,** *152* (2), 217-236.
6. Espro, C.; Donato, A.; Galvagno, S.; Neri, G., On the formation of cinnamyl alcohol during the hydrogenation of cinnamaldehyde under mild conditions on supported palladium catalysts. *Reaction Kinetics, Mechanisms and Catalysis* **2016,** *118* (1), 223-233.
7. Satagopan, V.; Chandalia, S. B., Selectivity aspects in the multi-phase hydrogenation of α,β-unsaturated aldehydes over supported noble metal catalysts: Part I. *Journal of Chemical Technology & Biotechnology* **1994,** *59* (3), 257-263.
8. Zhang, Y.; Liao, S.; Xu, Y.; Yu, D., Catalytic selective hydrogenation of cinnamaldehyde to hydrocinnamaldehyde. *Applied Catalysis A: General* **2000,** *192* (2), 247-251.
9. Christy, A. A., New insights into the surface functionalities and adsorption evolution of water molecules on silica gel surface: A study by second derivative near infrared spectroscopy. *Vibrational Spectroscopy* **2010,** *54* (1), 42-49.
10. Isaienko, O.; Borguet, E., Hydrophobicity of Hydroxylated Amorphous Fused Silica Surfaces. *Langmuir* **2013,** *29* (25), 7885-7895.
11. Toebes, M. L.; Alexander Nijhuis, T.; Hájek, J.; Bitter, J. H.; Jos van Dillen, A.; Murzin, D. Y.; de Jong, K. P., Support effects in hydrogenation of cinnamaldehyde over carbon nanofiber-supported platinum catalysts: Kinetic modeling. *Chemical Engineering Science* **2005,** *60* (21), 5682-5695.

Chapter 5

Conclusions and Future Work

5.1 Conclusions

The basis of this work was to garner a clearer understanding of the processes involved within hydrogenation reactions utilising palladium nanoparticle catalysts. To begin, focus was made to better understand the mechanisms behind nitrile hydrogenations. Through this, it was hoped to create a better understanding of the steps involved in this reaction which is critical to the agrochemical industry. Along with systematic experimentation and the modification of reaction variables for the model reagent crotononitrile, work was undertaken to understand the atomic level interactions upon the catalytic surface. To this end much work and focus was paid to the use of x-ray absorption spectroscopy, utilising a synchrotron.

Following from this work, logical steps led us to the observation of aldehyde hydrogenation. Due to previous work within the group testing the processes inherent in cinnamaldehyde hydrogenation using platinum catalysts, this work was designed to complement the findings.[1] It was hoped that the findings of the previous chapter could also be applied to this process and help better elucidate the inner mechanisms at play. In addition, work was undertaken to better understand the role of surface alignment on activity and selectivity, through the effects of both polar repulsive surface agents, and sterically hindering moieties.

5.1.1 Crotononitrile selective hydrogenation

Two catalyst series were generated, one upon amorphous silica and the other upon the mesoporous silica SBA-15. For these, a set of catalysts with varying metal loadings were synthesised and fully characterised. Through a series of systematic experimentation, modifying the reaction variables such as temperature, pressure, catalyst support and mass, metal loading, and hydrogen accessibility, several conclusions were made.

Whilst the variation of factors under ambient pressure yielded appropriate changes to the rate of C=C hydrogenation, no evidence of the conversion of the nitrile bond was observed. Additionally, simply increasing the pressure under ambient temperature yielded no results in this regard. However, upon a combination of higher temperature and pressure, optimally 120° C and 30 bar H_2, observation of nitrile hydrogenation was observed.

In this regard, the detected agents were the secondary and tertiary amines (dibutylamine and tributylamine), confirming the proposed mechanism of reaction and the ‘cascade event’ that occurs utilising the imine (**Figure 5.1**).[2]

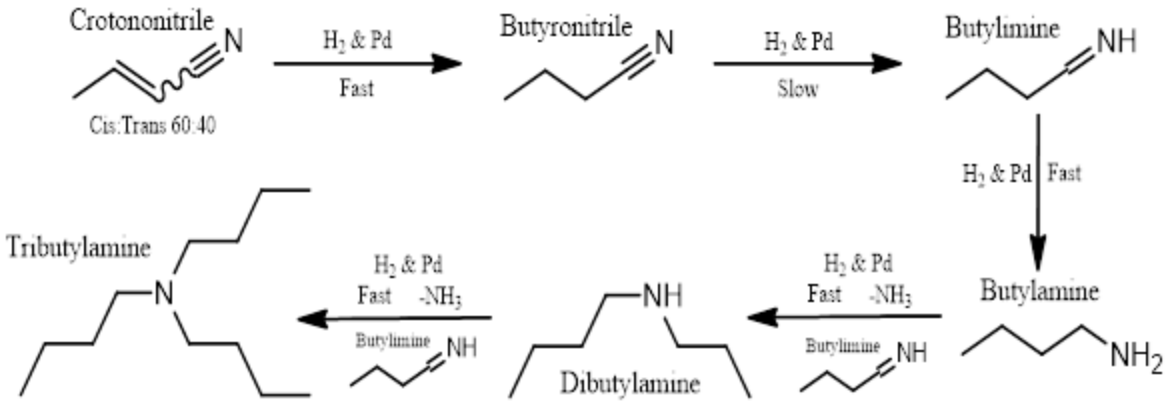

Figure 5.1 – Proposed and experimentally ratified reaction scheme for crotononitrile[2]

However, upon systematic experimentation over a number of hydrogen pressures, it was discovered that above 30 bar induced a rapid and significant drop in amine yield and thus nitrile hydrogenation activity (**Figure 5.2 – Left**). Determining that this must be due to a surface affecting event, extensive work was performed at the Diamond Light Source Synchrotron, to yield detailed *in-situ* X-ray Absorption Spectroscopy (XAS) data.[3] Here it was determined that a rarely documented palladium form, palladium-hydride (PdH) was formed whilst within solvent alone. With crotononitrile introduced, it was shown that the formation was retarded up to 40 bar, where the hydrogen accessibility exceeded the rate of consumption, allowing for suitable surface retention to form PdH (**Figure 5.2 – Right**).

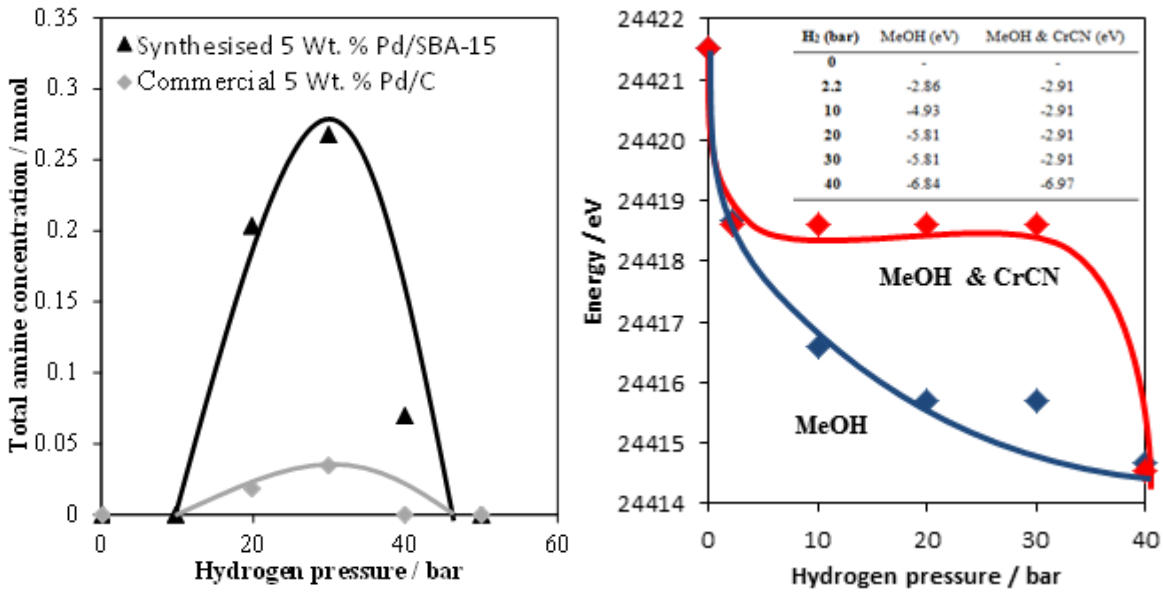

Figure 5.2 – Effect of pressure on amine yield (**Left**) and on hydride formation (**Right**)

The results of this ground-breaking work on *in-situ* XAS analysis of nitrile hydrogenation is the first of its kind to effectively observe the formation of palladium hydride as a function of reaction pressure. It also firmly supports the hypothesis that palladium hydride formation is detrimental to nitrile hydrogenation, affecting the surface properties, and/or electronic properties of the palladium metal active site.

5.1.2 Cinnamaldehyde selective hydrogenation

Through the use of the previously generated catalyst series upon both amorphous silica and SBA-15, a number of reaction variables were investigated in an attempt to better understand the roles of temperature, pressure, catalyst support and mass, metal loading and perturbation. Through these systematic experiments it was shown that whilst palladium exhibits a remarkable activity for C=C hydrogenation, especially in comparison to analogous platinum catalysts, the selectivity towards C=O hydrogenation is very low. When increasing the pressure within the range of 1-10 bar H_2 we see no significant change in activity or selectivity. This is explained though the sheer rate of activity making it impossible to differentiate effectively.

Most notably, regardless of reaction conditions the product cinnamyl alcohol was never formed successfully. In addition to this it was determined through experimentation for the kinetic diagram, that without the presence of the C=C bond, aldehyde hydrogenation will not occur as all (**Figure 5.3**). This was determined to be the result of reagent alignment, with the C=C bond pivotal for the correct orientation of the cinnamaldehyde to undergo aldehyde hydrogenation.

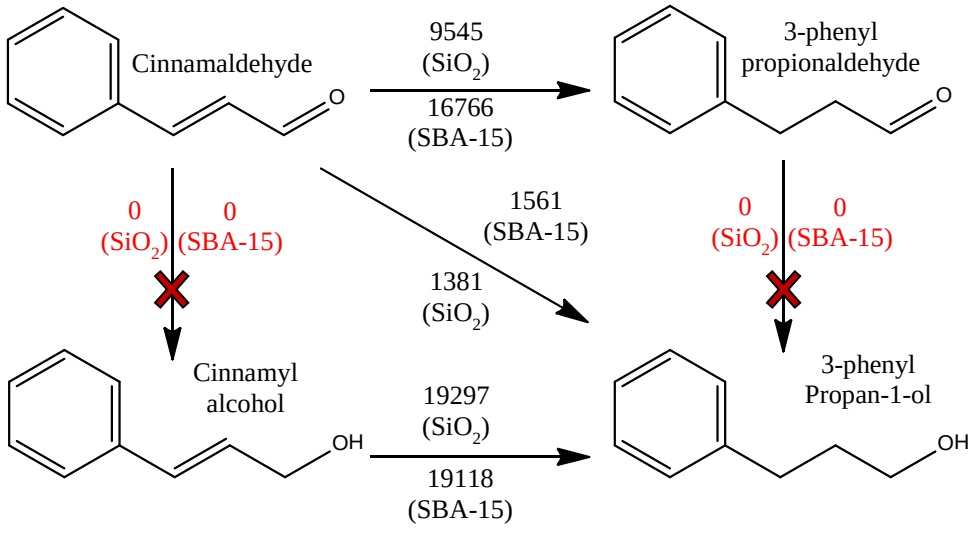

Figure 5.3 – Kinetic diagram for the process of cinnamaldehyde hydrogenation

With solid evidence of alignment-sensitive reactivity for the palladium, in much the same manner as platinum, additional research was undertaken into the factors which could affect this.[1] With literature evidence[4,5] espousing the effect of polar silanol groups upon silica supports causing repulsion and thus forcing the reagent into optimal alignment, it was determined that palladium is barely affected.

This is in direct comparison to platinum which is greatly affected by these repulsive agents with SBA-15, the most polar support, exhibiting significantly increased activity in comparison to amorphous silica.[1] Through examination of the properties of palladium nanoparticles it was concluded that the effect is diminished due to the stronger adsorption properties of the metal, leaving the reagent unaffected by the weakly repulsive force of the silanols. This also explains the low selectivity towards aldehyde hydrogenation, as the strength of adsorption causes the cinnamaldehyde to align sub-optimally.

Finally, in order to further elucidate the role of surface alignment, a series of experiments were run with aromatic aldehydes containing increasingly sterically bulky moieties in the *para* position. Here it was determined that the more sterically inhibiting the group, the lower the overall conversion, forcing the reagent into sub-optimal positioning or preventing it from adsorbing altogether (**Figure 5.4**).

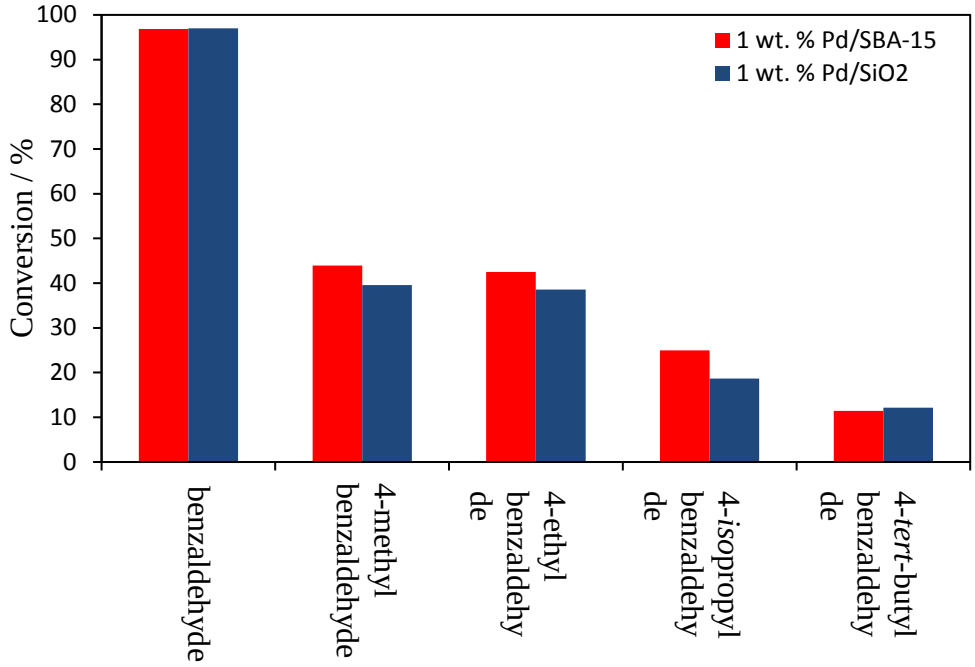

Figure 5.4 – Relative conversion of aromatic aldehydes in order of steric hindrance

The final conclusion from this chapter of work would be that whilst factors such as temperature, pressure, and hydrogen accessibility may affect the reaction rate, the greatest factor within this and also for selectivity is the role of surface alignment.

5.1.3 Future work

Through the work detailed within this thesis, there were several points which this author, time permitting, would wish to have investigated. As such, the following is a brief summation of work that may benefit or enhance the findings of this work.

In regards to the work on nitrile hydrogenation and the processes involved, this author believes that further investigation into the formation of palladium hydride, and its role on not only nitrile hydrogenation but also with a wide variety of reagents. As mentioned in the chapter, work of this nature involves the observation of subtle changes in eV and atomic distance. This is often open to some interpretation and any small errors or miscalculations during the work or processing of data may alter the results. Through both in-lab experimentation and subsequent visits to a synchrotron source facility, an even greater picture of the requirements for PdH formation and its effect upon the active sites would be generated. It would also reaffirm the findings and establish confidence in the results. This would undeniably contribute to the scientific community.

To work pertaining to aldehyde hydrogenation, this author believes that further investigations into the differences between the metal nanoparticles involved would be of great benefit. The significant differences in activity and selectivity between platinum and palladium, and the explanations regarding to adsorption strength and surface alignment are of great interest. Further work either with these two elements, or indeed a whole set of experimentation utilising a third would undoubtedly yield fascinating results.

Additionally, in regards to all hydrogenation processes, it is this authors belief that further research into tailored catalysts would be of great benefit both academically and commercially. Modifications to catalytic supports in terms of porosity, along with the formation of shape/size selective nanoparticles could generate innumerable novel findings.

5.2 References

1. Durndell, L. J.; Parlett, C. M. A.; Hondow, N. S.; Isaacs, M. A.; Wilson, K.; Lee, A. F., Selectivity control in Pt-catalyzed cinnamaldehyde hydrogenation. *Scientific Reports* **2015,** *5*, 9425.
2. Hegedűs, L.; Máthé, T.; Kárpáti, T., Selective heterogeneous catalytic hydrogenation of nitriles to primary amines in liquid phase: Part II: Hydrogenation of benzyl cyanide over palladium. *Applied Catalysis A: General* **2008,** *349* (1–2), 40-45.
3. de Groot, F., High-Resolution X-ray Emission and X-ray Absorption Spectroscopy. *Chemical Reviews* **2001,** *101* (6), 1779-1808.

4. Christy, A. A., New insights into the surface functionalities and adsorption evolution of water molecules on silica gel surface: A study by second derivative near infrared spectroscopy. *Vibrational Spectroscopy* **2010,** *54* (1), 42-49.
5. Isaienko, O.; Borguet, E., Hydrophobicity of Hydroxylated Amorphous Fused Silica Surfaces. *Langmuir* **2013,** *29* (25), 7885-7895.